REAL TIME OPTICAL CORRELATION

USING

WHITE LIGHT FOURIER TRANSFORMS

Final
Report of the technical work
15 September 1988

James B. Breckinridge
Erez Ribak
Claude Roddier
Francois Roddier
Christopher Habecker

Jet Propulsion Laboratory
California Institute of Technology
4800 Oak Grove Drive
Pasadena, California 91109

PREFACE

Optical image processing is the analysis by optical means of the information contained within an image. The most common optical image processor is a simple lens which takes an ensemble of wave-fronts which arrive at the lens from object space and transforms them into an image at an image plane some distance beyond the lens. Optical image processors of research interest today operate on that image in some manner to extract information of interest to the user.

The research work performed under this contract is an investigation of optical pre-detection processing of white light, passively illuminated scenes. This processing is performed in real-time on the incoming image signal. The image is not initially digitized, or detected or sensed in any of the typical ways, but rather it is processed in real-time, interferometrically by the optical processor and the output of the the analysis of the scene is recorded.

Such pre-detection processing is common among some areas of scientific instruments. The diffraction grating spectrograph is an example of an instrument that performs pre-detection processing on the signal: it enables a temporal frequency analysis for the spectral or color content of the light to be recorded. The interferometer system investigated here enables a spatial frequency analysis for the spatial content of the scene to be analyzed in real time.

Pursued in this work was analysis, hardware development and verification that an instrument to analyze the spatial frequency content of a white light scene using pre-detection processing is feasible. A preliminary evaluation was made of the suitability of this technology for field applications.

A laboratory breadboard white light rotational shear interferometer system was assembled from subsystems remaining from a discontinued NASA task

Data taken from this interferometer system was used to evaluate methods for phase closure for image reconstruction in the visible, for signal-to-noise ratio analysis theory including laboratory verification, for evaluation of engineering constraints for the construction of a portable unit, and for the design and implementation of several matched filter approaches for this type of interferometer.

Section 1 provides a brief analysis comparing the classical Vander Lugt filter approach with the white light rotational shear interferometer approach examined here. Section 2 describes the theory behind the interferometer, and section 3 describes the system itself. Sections 4, 5, and 6 describe computer analysis of the fringes, the signal to noise of the system and the method of phase closure achieved by it.

The research described in this report was carried out by the Jet Propulsion Laboratory, California Institute of Technology, under contract with the National Aeronautics and Space Administration, and was also sponsored by the United States Army Missile Command through an agreement with the National Aeronautics and Space Administration.

PARTICIPANTS

Participants in the Real-time optical correlation using Fourier Transforms project were:

James B. Breckinridge, Research director.

Erez Ribak, Scientist with assignment to operate the interferometer, to perform laboratory measurements of the fringes and reduce the data to determine the SNR properties of the brassboard.

Claude Roddier, Scientist with the assignment to develop software for the precision data reduction of the interferograms into fringes, and to provide an analysis of the fringe stability requirements.

Francois Roddier, Scientific consultant at no charge to the program. Provided support to the opto-mechanical alignment of the coherence interferometer (the rotational shear interferometer). Professor Roddier's salary was covered by the National Science Foundation at the Kitt Peak National Observatory.

John Stacy, Chief optical system engineer for the brassboard optical system.

Wai-Min Liu, Optical designer and responsible for the optical ray-trace design and engineering fabrication of the chromatic corrector.

Cesar Sepulveda, Optical engineer alignment and assembly of the brassboard optical system and the coherence interferometer assembly

Joel York, Former Caltech undergraduate student on a summer assignment under the Caltech SURF program to work in the optical interferometry laboratory.

Chris Habecker, Caltech undergraduate student on a summer assignment under the Caltech SURF program and as an Academic part-time student to work in the optical interferometry laboratory.

CONTENTS

LIST OF FIGURES

1. INTRODUCTION

In the following sections we provide a detailed discussion of the research activity pursued during this contract. These sub-tasks were accomplished under this contract:

1. Integration of the interferometer brassboard subsystems.
2. Development of mathematical methods to reduce fringe patterns.
3. Development of the signal-to-noise ratio (SNR) analysis.
4. The reduction of the SNR analysis to laboratory measurements to verify the theory.
5. Analysis of methods for phase closure to reconstruct images from fringes.

Results from this research appears in three peer-reviewed scientific publications [C Roddier and F Roddier 1987b, Ribak 1987b, Ribak *et al.* 1987] and are attached here. Four other interim reports were presented in scientific meetings [Ribak 1987a,c, C Roddier and F Roddier 1987a, Ribak 1988].

1.1 Optical Image Processors

This section provides a brief comparison between the Vander Lugt and the coherence interferometer approach to real-time optical information processing.

1.2 Vander Lugt Optical Correlators

The Vander Lugt optical correlator [Goodman 1968] requires that a white light scene be imaged onto an electro-optical image transducer such as a liquid crystal light valve. This electro-optical device changes the scene into one of variations in reflectivity across a thin film. These variations in reflectivity are much like one sees on the face of a liquid crystal digital wrist watch. Let us call these variations $g(x_1, y_1)$, where the subscript referes to plane P_1 in Figure 1.1. In the Vander Lugt optical correlator, the image on the liquid-crystal side is entirely illuminated with an expanded laser beam and the reflected signal is passed through a lens (L_1 with focal length f) in such a manner that the spatial frequency Fourier transform of the scene appears in the intensity distribution at the lens image plane (P_2). The amplitude distribution at this plane is $(1/\lambda f)G(x_2/\lambda f, y_2/\lambda f)$, where λ is the laser wave-length. Here, a matched filter containing the hologram reference signal is positioned. The matched filter is created by interfering a plane wave with the far-field pattern of a reference object and recording the resulting pattern on a hologram. For a number of reference objects a number of separate holograms must be created. Alternatively, several reference objects can be multiply encoded into the same hologram with different reference waves.

The Fourier transform of the scene is now multipied by the matched filter with a transfer function $t(x_2, y_2) = |r_0 e^{-2\pi i \alpha y_2} + (1/\lambda f)H(x_2/\lambda f, y_2/\lambda f)|^2$. $H(x_2/\lambda f, y_2/\lambda f)$ is the Fourier transform of some reference object $h(x, y)$, and $\alpha = \sin\theta/\lambda$, where θ is the angle between the recording beam and the reference object beam used to create the matched filter. The amplitude distribution just behind the mask is

$$u_2(x_2, y_2) = \frac{1}{\lambda f} G(x_2/\lambda f, y_2/\lambda f) t(x_2, y_2) \qquad 1.1$$

This result is inverse transformed by a lens (L_2; same focal length f) to a plane P_3 conjugate to the original scene input. The result is recorded on a two-dimensional detector, which squares

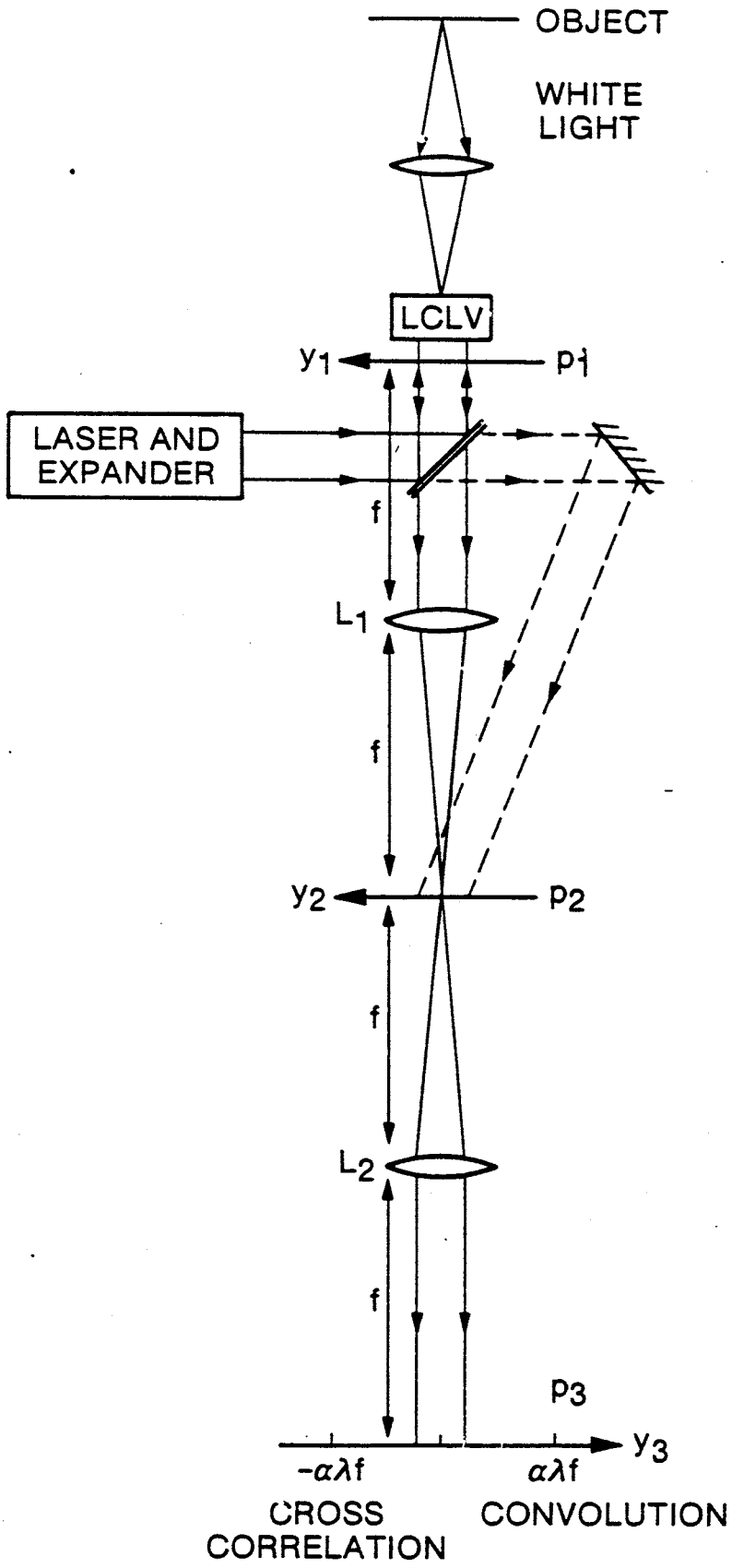

Figure 1.1. The Vander Lught Correlator. LCLV: liquid crystal light valve. L1, L2: lenses.

the amplitudes to yield a final intensity

$$
\begin{aligned}
u_3(x_3, y_3) = r_0^2 g(x_3, y_3) & \\
&+ \frac{1}{\lambda^2 f^2}[h(x_3, y_3) * h^*(-x_3, -y_3) * g(x_3, y_3)] \\
&+ \frac{r_0}{\lambda f}[h(x_3, y_3) * g(x_3, y_3) * \delta(x_3, y_3 + \alpha\lambda f)] \\
&+ \frac{r_0}{\lambda f}[h^*(-x_3, -y_3) * g(x_3, y_3) * \delta(x_3, y_3 - \alpha\lambda f)].
\end{aligned}
\qquad 1.2
$$

The third term on the right hand side represents the convolution of the reference object with the scene, and the fourth term the cross correlation of the two. These are centered at $(0, \alpha\lambda f)$ and $(0, -\alpha\lambda f)$, respectively. For reference width W_h and object width W_g there is full separation of all the components if $\alpha > (1/\lambda f)(3W_h/2 + W_g)$.

Several different object space scenes are passed into the correlator system. If one of the scenes contains an object whose spatial frequencies are the same as that in the reference hologram, a correlation signal is produced. The location within the image plane of this correlation appears at the output image plane and is recorded by a CCD.

This correlator was recently developed by JPL into a practical field unit [Bell 1986].

1.3 Rotational Shear Interferometry

The use of rotational shear interferometry eliminates the need for an electro-optical device which converts the white light beam into coherent laser light. The rotational shear interfereometer can produce the Fourier transform of a two-dimensional object in incoherent light. The light is divided by a beam-splitter into two beams and is recombined after they have been rotated with respect to each other. A point source on the axis will create a single white light fringe across the whole field. If the object is displaced from the axis (and its twin image is displaced in another direction) there will be a phase factor between the two rotated beams. This phase factor will appear as fringes across the field whose density is proportional to the object displacement. In the case of 180° shear, the fringes will be oriented perpendicular to the direction of displacement from the axis. If we add more and more points to the object, we incoherently add more and more fringes.

As in the Vander Lugt system, a matched filter containing the hologram reference signal is positioned in the Fourier plane. Different object scenes are passed into the system and those with the same spatial frequencies as the reference hologram produce a correlation signal. Since the signal is in white light, it is further processed by another coherence interferometer (alternatively, it can be re-directed into the first interferometer, provided some scheme is utilized to differentiate between the first and the second transforms.) The location of the correlation peak and its magnitude are recorded by a two-dimensional detector. The throughput of the optical processing is calculated in Appendix B.

1.4 Comparison of methods

Comparison of the measured performance of the Vander Lugt correlator and the predicted (based on laboratory measurements) performance of the coherence interferometer can be found in the following table.

	Vander Lugt Correlator	Coherence Interferometer
laser power	1 watt	0
liquid crystal light valve power	10 milliwatts	0
speed	50 milliseconds	< 10 nanoseconds
spatial resolution	512×512 (LCLV)	512×320 (CCD)
optical band-width	300Å@ 5000Å	2500Å@ 6000Å
size	10cm×10cm×10cm	currently 300cm×5cm×5cm down to 20cm×2cm×2cm
weight	1 kg	currently 20 kg down to 1 kg
detector power	same	same
dynamic range (simple object)	20	> 50
uniformity	SLM dependant (low)	detector dependant (high)
noise	coherent (clutter)	incoherent (Poisson, detector)
matched filtering	mechano-optical	electronic
technology status	high	low

1.5 Advantages of pre-detection processing

Predetection processing in optics is the manipulation of electro-magnetic wave-fronts to extract a signal of scientific, engineering or military interest. Either the entire wave-front or portions of the wave-front are either phase (time) delayed or spatially sheared to interfere with one another to observe a signal otherwise impossible to obtain. Detection of the radiation, that is, the conversion of the signal into electrons by taking the modulus squared of the superposition of the wave-fronts, is performed after the wave-fronts are manipulated.

The simplest example of wave-front manipulation is the formation of an image by a lens. Other examples are interferometers, Fourier transform spectrometers, and grating spectrographs.

2. ROTATIONAL SHEAR INTERFEROMETRY

Rotational shear interferometry allows the detection of spatial Fourier spectra in incoherent light. The manipulation of the signal can be accomplished by a beam splitter and two image folding roof prisms in a Michelson configuration [Mertz 1965], or by a Sagnac interferometer with a dove prism inside the common path, which has an opposite effect on the counter-propagating beams [Armitage and Lohmann 1965]. In either case the beams are rotated and then combined to create non-localized interference fringes. Both options are utilized in this project. The incoherent optical Fourier transform is obtained when each point of an incoherent object produces a distinct sinusoidal fringe pattern. The incoherent addition of all the fringe patterns produces the object Fourier transform. This is the case here when the interferometer gives two images of an incoherent object, one being rotated with respect to the other. Following the interferometer we have a color corrector, which compensates for the differential fringe frequency at different wave-lengths, and allows detection of multiple white light fringes. Next a double image of the object is formed, and a phase delay is introduced between the two beams, in order to allow modulation of the fringes. Finally the interferometer – with the fringes superimposed on it – is imaged onto a CCD sensitive detector.

Incoherent optical Fourier transforms have an advantage over coherent transforms in that they can be performed on natural white light scenes, as well as on simple input devices (CRTs, image intensifiers). They are also less sensitive to coherent noise and to system vibrations.

2.1 Analytic system description

We give here a short description of the principle behind the rotational shear interferometer, based on C. Roddier [1979]. Other descriptions can be found in Breckinridge [1976], George and Wang [1985], Glaser [1987], and Marathay [1987]. The idea was conceived by Mertz [1965] and further developed by Armitage and Lohmann [1965], Konjaev [1967], Stroke [1969], Cathey [1974], Courjon and Bulabois [1969].

Consider an object point, viewed through the entrance pupil in a direction $\mathbf{x}$ with complex amplitude $\Omega(\mathbf{x})$. The resultant complex amplitude at a point $\mathbf{r}$ in the entrance pupil, situated a distance z from the object, is given by

$$A(\mathbf{x},\mathbf{r}) = \Omega(\mathbf{x}) e^{i\pi r^2/\lambda z} e^{-2i\pi \mathbf{x}\cdot\mathbf{r}/\lambda} \tag{2.1}$$

where λ is the wave-length of the light. The interferometer adds up the complex amplitude of the incoming wave with its point symmetric duplicate, to yield in the exit pupil (Figure 2.1)

$$\begin{aligned} 2^{-1/2}[A(\mathbf{x},\mathbf{r}) + A(\mathbf{x},-\mathbf{r})] &= 2^{-1/2}\Omega(\mathbf{x}) e^{i\pi r^2/\lambda z}[e^{-2i\pi \mathbf{x}\cdot\mathbf{r}/\lambda} + e^{2i\pi \mathbf{x}\cdot\mathbf{r}/\lambda}] \\ &= 2^{1/2}\Omega(\mathbf{x}) e^{i\pi r^2/\lambda z} \cos(2\pi \mathbf{x}\cdot\mathbf{r}/\lambda) \end{aligned} \tag{2.2}$$

where we assume that the optical path difference is zero and that the pupil is infinite in size. The intensity $I(\mathbf{x},\mathbf{r})$ observed over the exit pupil is the square of the modulus of expression 2.2:

$$\begin{aligned} I(\mathbf{x},\mathbf{r}) &= 2O(\mathbf{x}) \cos^2(2\pi \mathbf{x}\cdot\mathbf{r}/\lambda) \\ &= O(\mathbf{x})[1 + \cos(4\pi \mathbf{x}\cdot\mathbf{r}/\lambda)] \end{aligned} \tag{2.3}$$

where $O(\mathbf{x}) = |\Omega(\mathbf{x})|^2$ is the brightness of the source in the direction of $\mathbf{x}$. Expression 2.3 represents the interference fringes of fringe spacing $\lambda/2|\mathbf{x}|$. The object $O(\mathbf{x})$ is incoherent, which means two

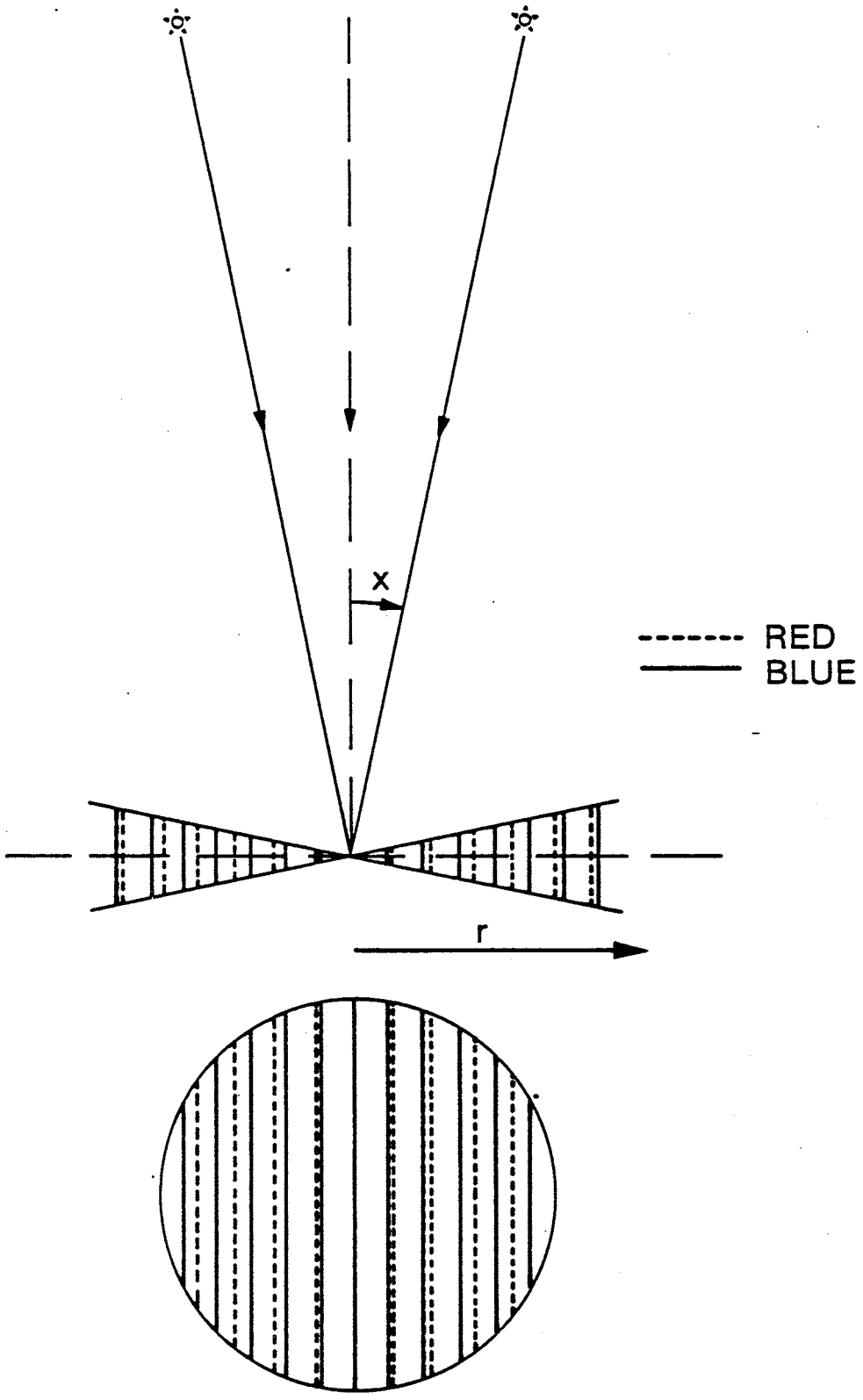

Figure 2.1. Interference fringes between two centro-symmetric twin images of a point source in poly-chromatic light.

different points on it cannot interfere. The fringes produced by each point of the object add up to a resultant intensity

$$\begin{aligned} i(\mathbf{r}) &= \int I(\mathbf{x},\mathbf{r})d\mathbf{x} \\ &= \int O(\mathbf{x})d\mathbf{x} + \int O(\mathbf{x})\cos(4\pi\mathbf{x}\cdot\mathbf{r}/\lambda)d\mathbf{x} \end{aligned} \qquad 2.4$$

If the Fourier transform of $O(\mathbf{x})$ is $o(\mathbf{u})$:

$$o(\mathbf{u}) = \int O(\mathbf{x})e^{-2i\pi\mathbf{x}\cdot\mathbf{u}}d\mathbf{x} \qquad 2.5$$

then expression 2.4 can be written as

$$i(\mathbf{r}) = o(0) + Re\{o(2\mathbf{r}/\lambda)\} \qquad 2.6$$

where $Re\{.\}$ represents the real part of a function. When calculating the two-dimensional Fourier transform of $i(\mathbf{r})$ one obtains

$$I(2\mathbf{x}/\lambda) = o(0)\delta(\mathbf{x}) + \frac{1}{2}[O(\mathbf{x}) + O(-\mathbf{x})] \qquad 2.7$$

where $\delta(\mathbf{x})$ represents a Dirac delta function at the origin. It is thus possible to retrieve the original brightness $O(\mathbf{x})$ in the object provided the two elements are sufficiently separated and do not overlap with the origin. Our interferometer allows us to combine two images of the object rotated at any angle β with respect to the optical axis of the system. Thus every point in the wavefront interferes with a point which is no longer necessarily symmetric about the optical axis, at a distance of $2|r|$. The distance between the interfering points is now $2|r\sin(\beta/2)|$. The particular case $\beta = 180^0$ corresponds to the calculation above. Where β is less than this value, we have to modify 2.6 to read

$$i(\mathbf{r}) = o(0) + Re\{o(2\mathbf{r}|\sin(\beta/2)|/\lambda)\} \qquad 2.8$$

Thus, a smaller shear angle β allows us to zoom on lower frequencies of the object. The irradiance distribution $i(\mathbf{r})$ in the hologram can now be written in a general way

$$i(\mathbf{r}) = o(0) + Re\{o(k\mathcal{R}\mathbf{r}/\lambda)\} \qquad 2.9$$

where $\mathcal{R} = 2|\sin(\beta/2)|$ is a rotation operator and k is a magnification factor between the pupil and the detector.

3. THE BRASSBOARD OPTICAL SYSTEM

The brassboard optical system components were procured by the National Aeronautics and Space Administration for a JPL project in optical image processing. The hardware was delivered after funding for the NASA program was cancelled. The United States Army paid for the final integration and test of the hardware and for the analysis, interpretation, and measurements made with the apparatus.

3.1 Optical system overview

The laboratory optical system consists of a light source and target assembly, interferometer, color corrector optical system (Chromatic Corrector), and digital CCD camera linked to a small computer system. It was designed and built to achieve the immediate goals and serve as apparatus for more advanced experiments. A drawing and a photograph of the apparatus is shown in Figures 3.1 and 3.2. Appendix A contains a copy of the optical prescription for this laboratory brassboard system. A description of each primary subsystem is now given.

3.2 Light source

The illumination and target system provided reasonably uniform illumination across the field of view (ten arc-minutes) for a variety of binary amplitude masks used for these experiments.

Initially, we used a commercial white light source with a fibre optic bundle and a microscope objective to illuminate a miniature pinhole mask for the object space irradiance distribution. This pinhole mask was re-imaged with a 1 meter focal length telescope. Unfortunately, the appropriate pinhole masks are difficult to make. After several experiments we discarded the microscope and the telescope, and used the mask far enough from the rest of the system so that the far-field approximation for Fraunhoffer diffraction was obeyed. This enabled the use of standard 35 millimeter slides for the objects. The illumination across the slides was not as uniform as one might have preferred, due to the nature of the fibres. Therefore we replaced the fibre bundle by a perspex rod light-guide, directly feeding from the light source. This allows full mixing of the light and a very high irradiance uniformity across the slides.

3.3 Targets

We produced a set of slides that allowed us to have different object inputs at various scale sizes and different degrees of complexity. Scene complexity is defined as the number of non-interacting (incoherent) point sources that are required to make up the scene. Most of the slides are simple cut-outs in aluminum foil. It should also be stressed that real three-dimensional objects were used as an input, merely by illuminating them and positioning them in the vicinity of the input plane of the system. White light holograms were recorded to give three-dimensional reconstruction of the scene details.

3.4 The rotational shear interferometer subassembly

The rotational shear interferometer subassembly consists of the glass (BK7, Schelerin grade) prisms and the precision opto-mechanical mounting and adjustment fixture used to adjust and align the interferometer.

Optical configuration. The rotational shear interferometer is a Michelson interferometer with roof prisms for reflectors at the two arm ends and the optical path lengths in each arm set equal. Details of the theory and construction of this interferometer assembly can be found in Roddier *et al.* [1978] and Breckinridge [1976].

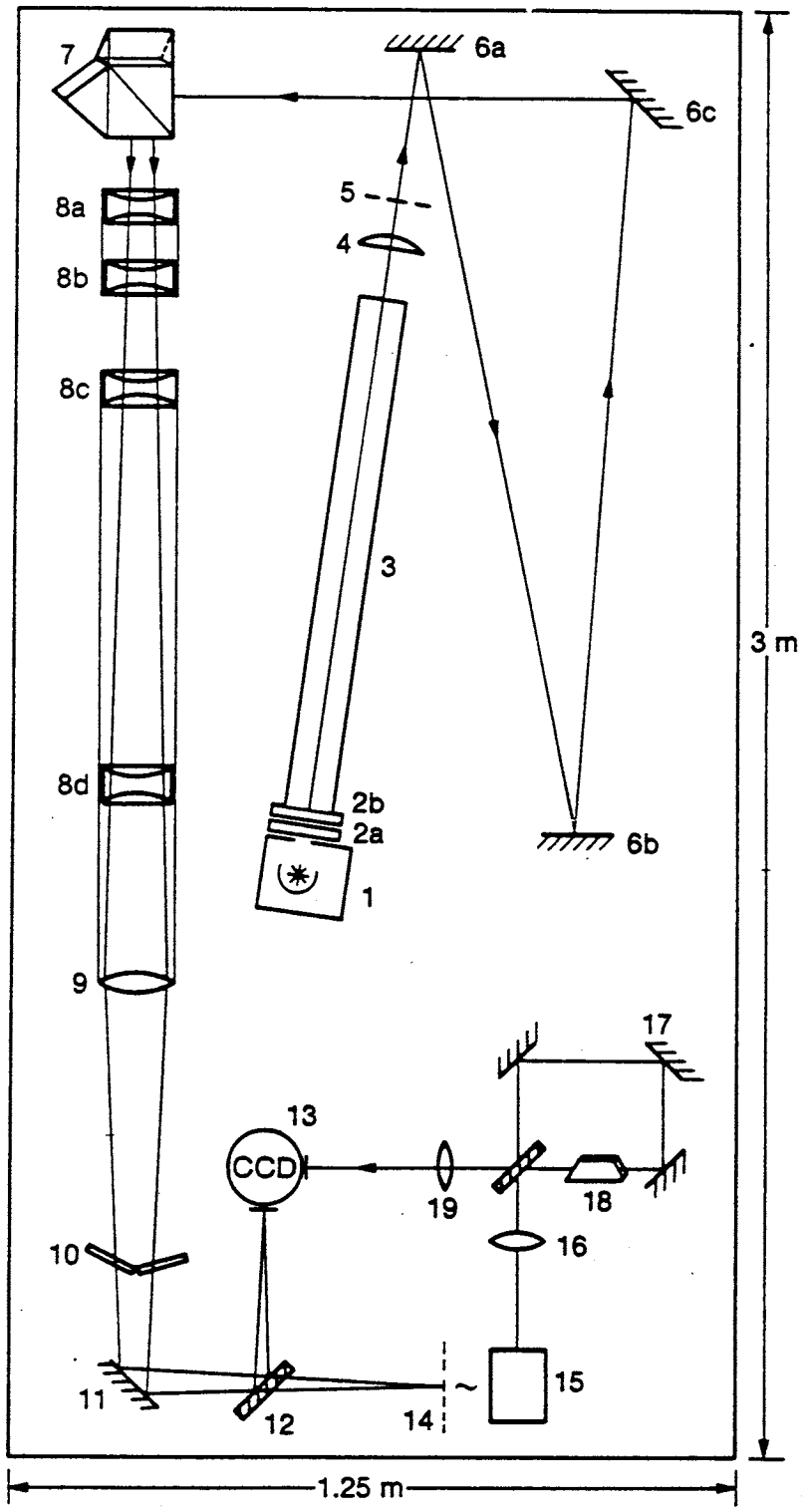

Figure 3.1. The optical system. 1) white light source. 2a,b) heat dissipators. 3) plexiglass (lucite) waveguide rod. 4) collimating lens. 5) 35 mm slide (image input plane). 6a-c) beam folding mirrors. 7) rotational shear interferometer (image far-field). 8a-d) color-correction system. 9) relay lens. 10) Jamin compensator. 11) folding mirror. 12) variable beam-splitter. 13) cooled detector. 14) image far-field (conjugate to 13 and 7). 15) coherent-to-incoherent converter. 16) collimating lens. 17) Sagnac rotational shear interferometer. 18) dove prism. 19) collecting lens.

Figure 3.3 shows a sketch of the optical configuration of the interferometer. White light compensation is achieved by mechanically shearing one prism cube across the face of the other and examining on axis, the channel spectra produced by interference fringes of the light coming from each arm of the interferometer. As alignment for the white light fringe becomes closer the channel spectra fringes are observed to "open up". Alignment for white light compensation is achieved when only one channel line spectrum is observed across the visible region of the spectrum.

To make the instrument most versatile it was decided to construct it with variable or tunable angular shear. This was done in a manner used by others [Roddier *et al.* 1978, Hofmann and Weigelt 1986, 1987, George and Wang 1984]. The roofs are constructed separately and a specially built opto-mechanical jig assembly enables rotation with interferometric precision. Being able to rotate these roofs, however introduces a polarization effect which effects the fringe contrast and contributes to a degradation in the signal to noise ratio achievable.

Polarization correction. A method first proposed by Armitage and Lohmann [1965] and first apllied by Roddier *et al.* [1978] was employed to maximize the fringe contrast. Cemented quarter wave plates were used at the interfaces of the roof assembly and the prism assembly to convert linearly polarized white light at any polarization angle to circular which is insensitive to rotation angle. Interference takes place in circularly polarized light and the circularly polarized interference signal is then converted back to linear at the original angle by the same quarter wave plate for measurement.

Fabrication of the glass prisms. Figure 3.4 shows a photograph of the prism assemblies. The prisms were made in the optical shop of the Astronomical Observatory of the Universite of Nice, France. They were the low bidder in an international competition. The functional requirements for the prism assembly included one-half arc second on the return beam from each roof and a general over-all alignment tolerance on the angles of 10 arc-seconds.

The prism assembly is designed to accomodate a clear aperture of 25 mm. The glass for the prisms is Schott BK7 Schelerin grade specially selected for use in an interferometer. The total optical path within the prisms exceeds 10 centimeters. Laboratory measurements show that a plane wave enteering the interferometer, exits the interferometer flat to within 0.1 wave.

Opto-mechanical fixture. White light fringes are obtained by sliding (micrometer screw precision) the two halves of the beam-splitter across each other with lubrication by an index-matching oil. The same technique applies for the rotation, where one roof prism is sliding around over the end of the beam-splitter on an oil film and over the flat end. Across the face of each roof prism assembly are two quarter-wave plates to minimize the deleterious effects of polarization reducing the fringe contact (see above). The optical quality is superior, and straight fringes are observed across the whole aperture. A special mount was designed and built to provide for alignment, fringe acquisition and field rotation.

The text in appendix A describes in detail the construction of the prisms and their jig assembly mount.

Another interferometer was later built to provide inverse transforms [Armitage and Lohmann 1965]. It is of the square Sagnac type, with a dove prism inside it to obtain image rotation. The two counter-propagating beams traverse the prism in opposite directions and are thus rotated in inverse orientations.

3.5 The Chromatic Corrector

A major effort in optical system ray-trace design enabled the design and construction of a chromatic corrector with properties for broad band correction for the interferometer focal plane. It should be noted here that some applications require only low spatial coherence, but not wide band light, and can be processed without color correction. Between these we can count processing images

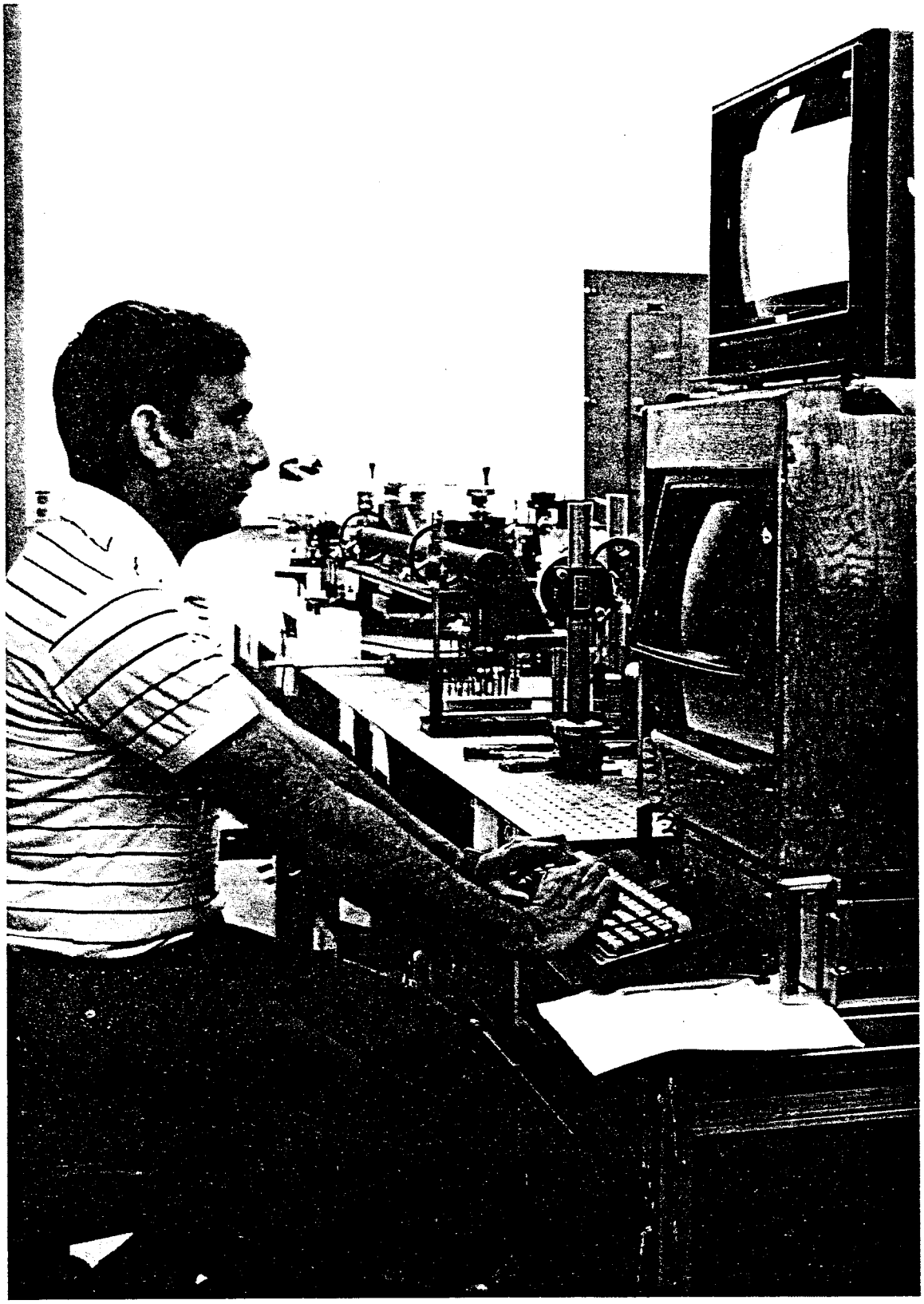

Figure 3.2. Overview of the optical system, as seen from the bottom-left corner in figure 3.1. In front is the camera computer and display.

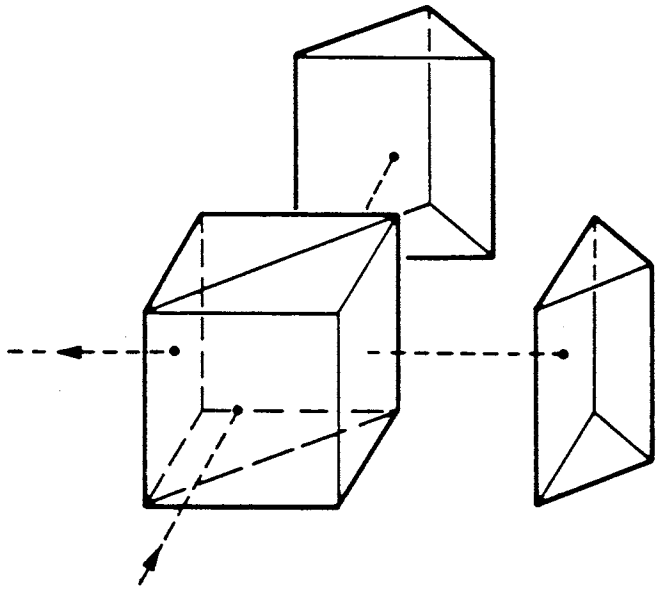

Figure 3.3. The prism assembly. The beam-splitter and two (rotatable) roof prisms. The polarization corrector plates are combined with the roof prisms.

that come off a cathode-ray tube and are usually limited to the narrow band of the phosphor, and multi-mode fiber optic systems.

To achromatize the interferometer fringes, we require a linear variation of magnification with wave-length. It is therefore a very special lateral chromatic aberration that we introduce, one that is linear with increasing radius. This is seen by writing the equation for Young's fringes at two wave-lengths λ_c (a control wave-length) and λ (any other wave-length) to give:

$$x_c = \frac{s}{d_c}\lambda_c; \qquad x = \frac{s}{d}\lambda \tag{3.1}$$

and subtracting the two to give:

$$x_c - x = s(\frac{\lambda_c}{d_c} - \frac{\lambda}{d}) = 0 \tag{3.2}$$

where we have set the difference to be zero to obtain achromatic fringes. solving for $d(\lambda)$ we obtain:

$$d(\lambda) = \lambda\frac{d_c}{\lambda_c} \tag{3.3}$$

This is the magnification variation at the doubled image plane, required to superpose all of the colored fringes at the detector plane and thus produce an achromatic fringe performance. Figure 3.5 shows a plot of wave-length from 0.4 to 1.0 micrometers as a function of $d(\lambda)/d_c$, where d_c is the separation of two points at the doubled image plane 10 in Figure 3.1. This is the variation in chromatism required from a "chromatic" corrector for the interferometer.

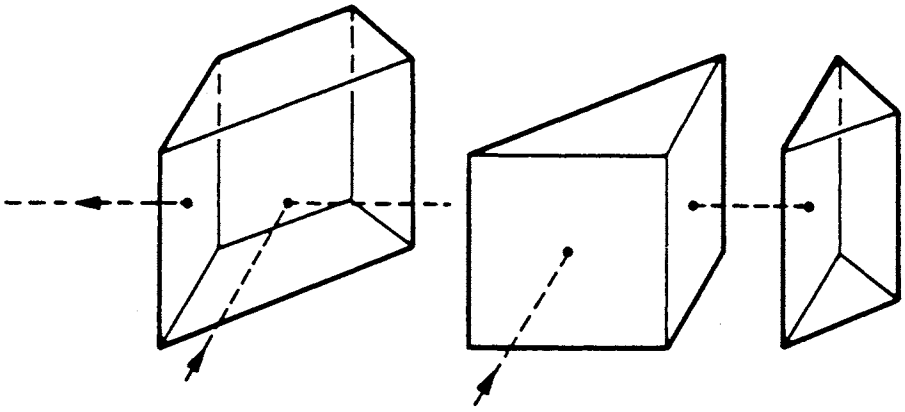

Figure 3.4. Overview of the prism assembly showing the sliding surfaces. An oil layer between the two halves of the beam-splitter allows path-length equalization. Another such layer permits rotation of one roof prism about its axis. The polarization corrector plates are combined with the roof prisms.

Qualitatively, a single polychromatic point in object space will be mapped into two polychromatic points at the "doubled" image plane shown at plane 10 in Figure 3.1. At the detector plane (an image of the pupil plane) fringe patterns will appear. Radiation from the blue portion of the spectrum from the polychromatic point will produce more closely spaced fringes than that from the red. The chromatic corrector must change the spacing of the fringes so that the fringes over the entire detected spectrum overlap. For a given pupil size before and after the corrector there will be seen a separation of the red and blue portions of the spectrum. The blue portion will cover a larger area than the red one.

Wang and George [1985] described in detail one design for a chromatic corrector. Roddier *et al.* [1978] described another approach to the design. Here we approached the problem from the exact computer-aided design point of view. We modeled in the VAX 11/785 computer the detailed optical system shown in Figure 3.1. The system was modeled from the light source through to the detector, including actual values for all of the optical thicknessess and the clear apertures on the mirrors.

After the system was set up in the CODE V computer program, the radii of curvatures and lens separations were changed using the linear damped least squares routines available within the program to optimize for maximum chromatic correction across the detector plane. Table 1 gives the optical prescription for the 22 element chromatic corrector. Table 2 shows a comparison between the theoretically calculated dispersion curve and a measured dispersion for the as-built system.

The chromatic corrector was designed and specified using the JPL VAX 11/785 computer with

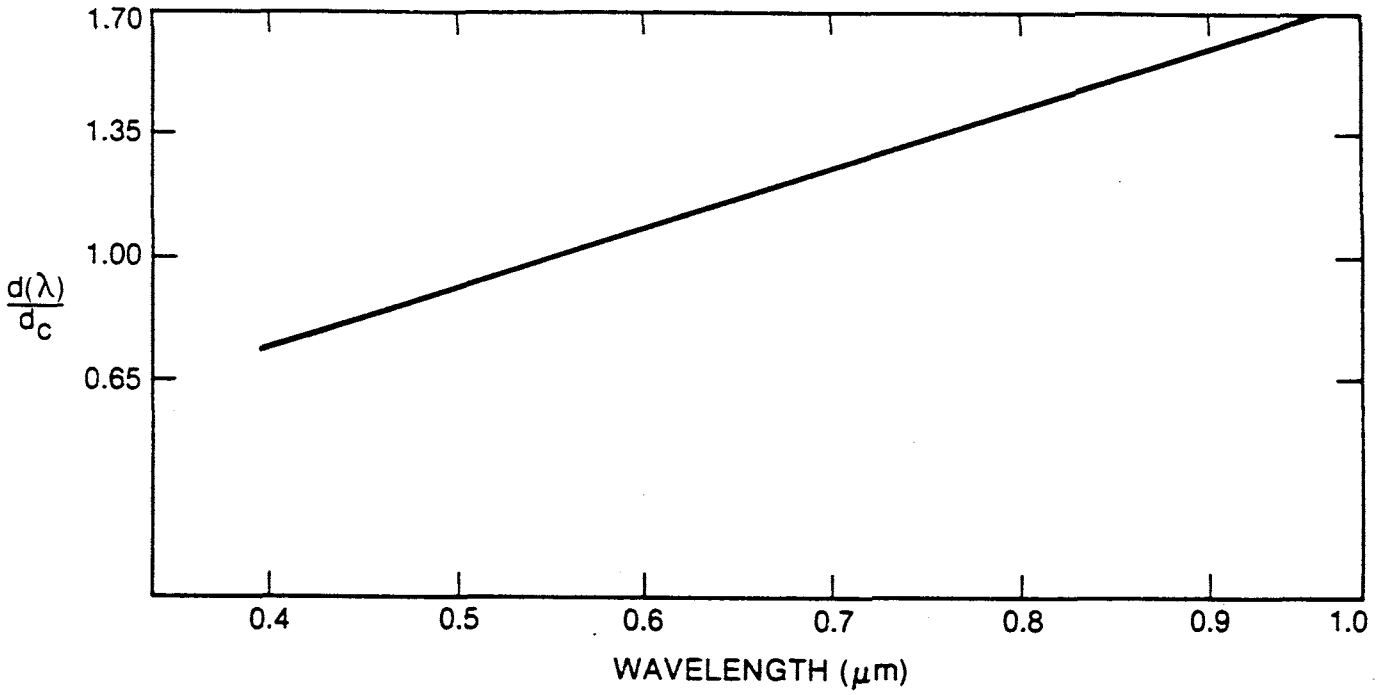

Figure 3.5. Wave-length dependence of the color corrector magnification.

a leased version of the computer aided design ray trace program CODE V. The optical elements were fabricated by Perkin-Elmer Corporation (Garden Grove, California) optical company. The tube and mounting assembly were built in the instrument machine shop at the Jet Propulsion Laboratory.

One advantage of using wide band light is that there is a reduction in noise level, as compared to narrow band systems. This reduction is due to the increased integrated intensity, and the elimination of coherent noise (such as from dust specks on the optical elements) which appears as clutter. The corrector was fabricated, aligned and its performance verified. Its linearity is better than 4% over the visible region, and better than 1% over the central 200 nm in that region.

In our experiment the color correction is achieved by a system of four afocal triplet lenses, combined with a relay lens, all placed after the interferometer. The relay lens re-images the twin images, which are chromatically dispersed, and the beams expand on freely to interfere on the detector. The chromatic dispersion is such that the angular distance between the twin images, as viewed from the detector, is proportional to the wave-length. Since fringe spacing is proportional to both the wave-length and the inverse of this angular distance, it becomes wave-length independent. Indeed by putting in Equation 2.9 a magnification factor $k = m\lambda$ proportional to the wave-length λ we have a wave-length independent illumination

$$i(\mathbf{r}) = o(0) + Re\{O(m\mathcal{R}\mathbf{r})\} \qquad 3.4$$

After the chromatic corrector every image point is smeared into a spectrum expanding radially from the optical axis. When interfering on the detector the two beams produced by twin points combine together to create white light fringes. We have counted a few hundred such fringes with the CCD detector. A test using system illumination at a series of discrete wave-lengths between 500 and 700 nanometers showed less than four percent error for the desired equally spaced fringes.

3.6 Phase switching

We refer again to figure 3.1, which shows a schematic of the entire interferometer optical system. A special apparatus was placed at the doubled image plane (shown as plane 10). This apparatus enabled phase shifting or modulation of the fringes at plane 13 to improve their detectability.

Fringe modulation is desirable to maximize the signal to noise ratio of the system. A total spatial separation of the two rotationally sheared images which appears at plane 13 in Figure 3.1 is necessary if one wants to reconstruct each image from its Fourier component. Otherwise the two reconstructed images overlap and in the regions of overlap, the images co-mingle and are confused. This means that there is also a spatial separation of the images before detection. The separated images means that a time-varying phase mask can be placed over one of the images but not the other to enable a path-length modulation different in each path. To increase the signal-to-noise ratio the phase modulation can occur at a high frequency and the CCD array configured for phase-locked synchronous loop detection.

A drawback of incoherent holography is the D.C. bias produced by the term $O(0)$ in Equation 3.4. Another bias term composed of light scattered in the system and dark current of the CCD should be added to this term. In order to remove these bias terms two holograms were taken per image, with the fringe phase flipped 180 degrees between them, thus flipping the sign of the last term in Equation 3.4 [Kozma and Massey 1969, Ribak and Leibowitz 1985, Ribak *et al.* 1985, Rhodes and Sawchuck 1981]. Taking the difference between the two (digitized) holograms gives

$$\Delta(\mathbf{r}) = Re\{o(m\mathcal{R}\mathbf{r})\} \qquad 3.5$$

i. e. a hologram with the bias terms removed.

We constructed a Jamin compensator as shown in Figure 3.6. It consists of two same pieces of glass, tilted at some small angle. Each beam of the interferometer passes through either glass, and rotation of the two glasses together introduces a differential effect on the path lengths. The observational procedure for the data recorded in this experiment was to take two pictures for each object, one with the fringes at zero phase and the other with the fringes at quadrature. The fringe patterns are then subtracted digitally to yield only the fringe signal. Figures 3.7a-b show photographs of the fringes. Figure 3.7c shows an example of a hologram obtained with this procedure (another such hologram can be seen in Figure 5.1). It has three advantages:

1) It removes all the bias components, including their irrelevant spatial structure.
2) The noise (contributed mainly by fluctuations in the bias terms) is multiplied by $\sqrt{2}$. But, since the signal is doubled, the SNR increases by a factor $\sqrt{2}$.
3) It improves the dynamic range. Although for the CCD read-out we still use the same dynamic range, the digital Fourier transform that follows gains from the more limited range of input levels.

3.7 The CCD array detector

A very sensitive digital charge coupled device (CCD) camera with 16-bit per pixel dynamic range is used to detect fringes in the Fourier plane. The Photometrics camera system* consists of a 320×512 CCD RCA detector mounted in a liquid-nitrogen cooled dewar, and an analogue-to-digital converter. A Heurikon computer with a Unix V system utilizing with one megabyte of random-access memory is used for near real-time digital data processing. Images are stored on a 65 megabyte disk, a nine-track tape or floppy disk. The data processing software provided by the manufacturer includes image addition, subtraction, multiplication and division, panning and

* Photometrics Ltd., 2010 N. Forbes Blvd, Suite 103, Tucson, Arizona 85745.

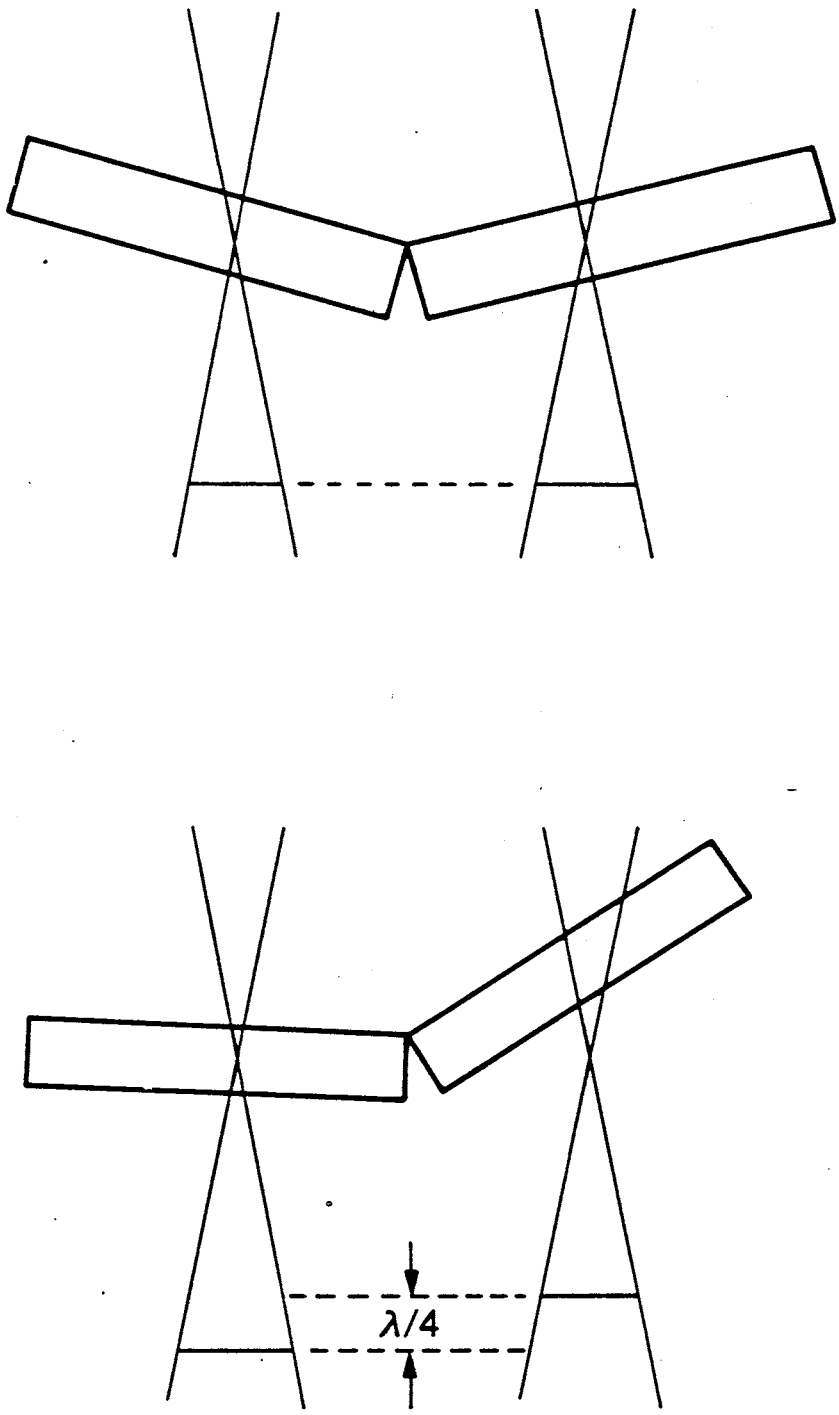

Figure 3.6. The Jamin compensator.

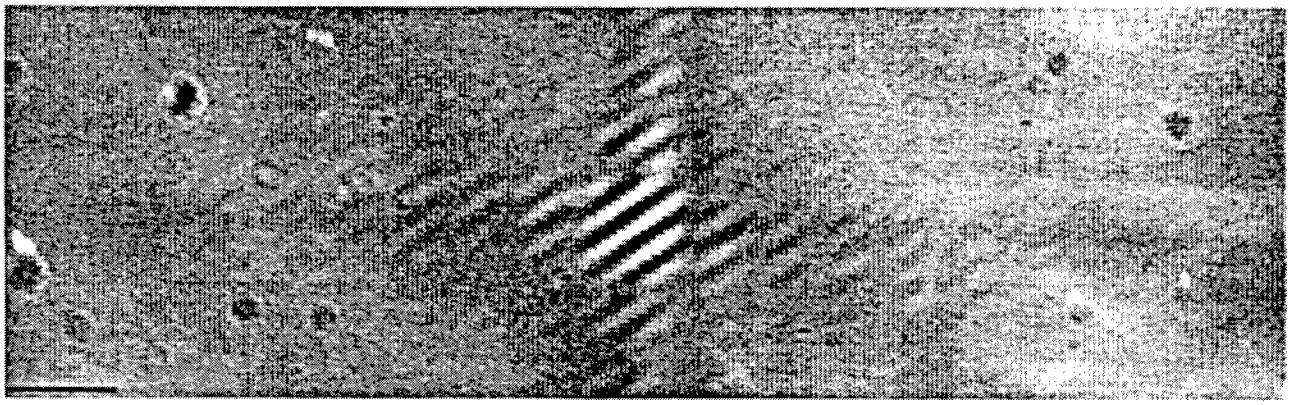

(a)

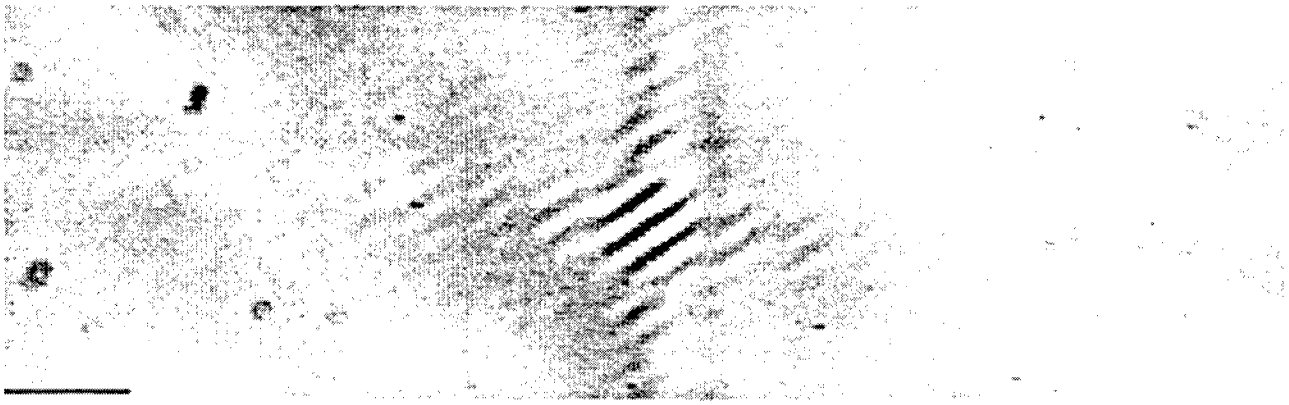

(b)

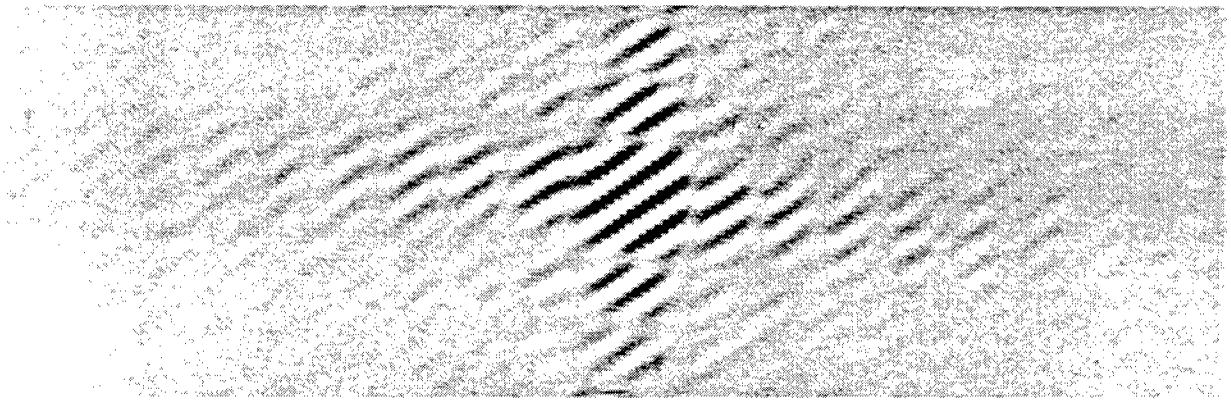

(c)

Figure 3.7. a) white light fringes due to a square object. b) fringes from the same object, with a $\pi/2$ phase shift. c) difference between the two holograms.

zooming, statistics, cross-section, histograms, etc. The system includes a scan converter and a graphics separate display.

For additional processing, images can be loaded (by use of the tape) into any mainframe computer. In our case, we utilized interchangeably two VAX 11/785 computers, one in the Optical Sciences and Applications Section, in the Jet Propulsion Laboratory in Pasadena, and one in the National Optical Astronomical Observatories computer center in Tucson. Software developed at NOAO under sponsorship of the National Science Foundation was modified under sponsorship of the U.S. Army for special application to the needs of this program.

Additional details of the CCD camera are given in appendix C.

3.8 Link to second interferometer

One of the applications of the rotational shear interferometer is its inclusion as a part of an optical correlator. Such a correlator has two cascaded interferometers, the first producing one transform, the second an inverse one. In order to correlate a scene with some object, the transform of that object is multiplied by the transform of the scene as represented by a matched filter [Marathay 1987]. After inverse transforming, a thresholding function can be applied to detect the location of a correlation peak. We describe here the first step of an experiment towards this end.

The first thing to realize is that the inverse transform also has to be produced in white light. By this we mean that no lateral coherence is allowed in the input image of either interferometer. The calculation in §2.1 assumes that every point in the object emits light that is statistically independent of that emitted by other points. Otherwise the doubled far-field pattern of the object, will be redoubled by a second equal system. It will have in *its* far-field pattern the quadrupled image of the object: a double-image from the first interferometer doubled again in the second one. This method was analyzed before [Wang and George 1985], and requires perfect alignment of all four images. However, it does not make use of the incoherent transform capabilities of the second rotational shear interferometer.

How do we make coherent light incoherent? Since we only require loss of lateral coherence, this seems an easy enough task: use a scatter plate (preferrably a moving one, for averaging puposes) to render the light spatially incoherent. The scatter plate is positioned in the transform plane of the first interferometer as an input for the second interferometer. Unfortunately, the scattering has to be strong (over 4π) or else the light will remain coherent. This means a large loss of light, since one starts with a rather collimated beam from the first interferometer and such a beam is also required for the second interferometer. We next tried an organized ("coherent") bundle of fibres, were there is a full and correct geometric mapping between the input (namely the transform plane of the first interferometer) and the output (which is the input to the second interferometer. If single mode fibres are used, we assume different path lengths in them, longer than the coherence length of the light. If the bundle is made of multi-mode fibres, the assumption is that the many scatterings inside each fibre, as well as the indepence of scattering centers between fibres, will leave the light collimated but incoherent. Unfortunately, we found that the coherence persisted for all the bundles we tried, single mode as well as multi-mode ones, which means that our assumptions were not fulfilled.

Looking at equations 2.3 – 2.6 we notice that the transform is achieved by observing the *intensity* of the interfering waves. This means that if we want to use two rotational shear interferometers in cascade, we have to detect the light from the first one, and re-transmit it to the second one. We found out that an image intensifier was too wasteful as it scattered the light over 2π. The collimated beam traversing the second interferometer was too faint and long integration times were required. The image intensifier was also cumbersome to work with, because of its sensitivity to

background lights.

Another solution we tried was a video link – detecting the fringes with a commercial CCD video camera and broadcasting them to the second interferometer by means of a television screen. Unfortunately, such a screen has the same disadvantage, namely that it scatters the light over a large angle, and very little is captured by the interferometer. A less pleasing, but brighter input was found to be a commercial liquid-crystal television screen, illuminted by a strong collimated white light beam. A fibre bundle feeds the light from a light source onto the screen, which multiplies it by the input scene as brought in by the video line. Inverse transformed objects (along with their twin image) can be seen in Figure 3.8. The limitations of the video link are low detection sensitivity, a small space-bandwidth product, reduced dynamic range, low contrast (for the liquid-crystal tlelevision), or low light levels (for the standard screen).

3.9 Second interferometer

A second rotational shear interferometer was built in the lab for producing simultaneous inverse transforms. It is of the Sagnac type interferometer (Figure 3.9), with a beam-splitter and three mirrors (in a rectangular configuration), and the two beams are counter-propagating over the same path. A dove prism is inserted in the interferometer, and the two beams are rotated about their common axis at twice the rotation angle of the prism. Since their directions are opposite, their rotation is also in opposite sense. Thus, for a rotation of 45°, each beam is rotated by 90°, with a total difference of 180°. After devising and building the interferometer, we found out that the idea has been proposed previously [Armitage and Lohmann 1965]. This interferometer is very easy to align and maintain, and was mounted as a unit on a small, separate optical table. Unfortunately, the mirrors we used are not adequate for this interferometer, and polarize the light differently. The polarizations differ by about 40° and the intensity ratio can be up to 3:1. The dove prism does not change the polarization in any significant manner, as predicted theoretically and verified in the lab.

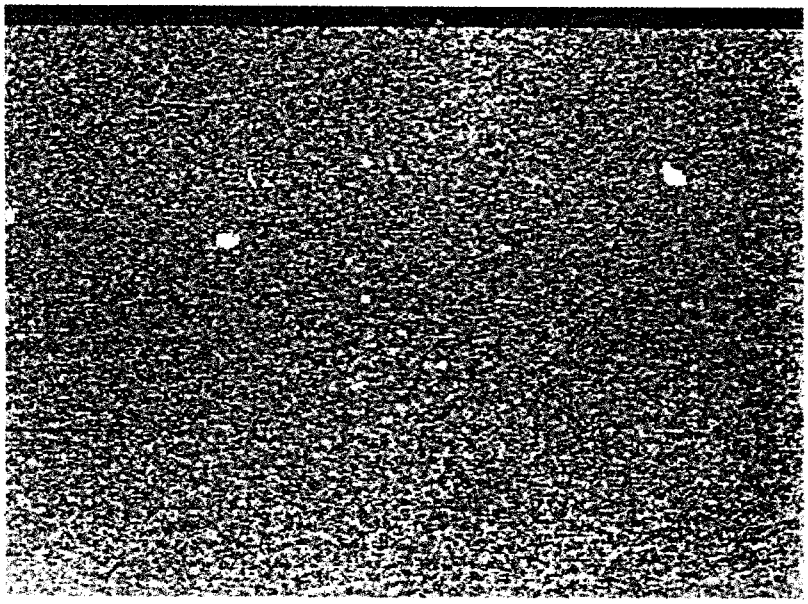

(a)

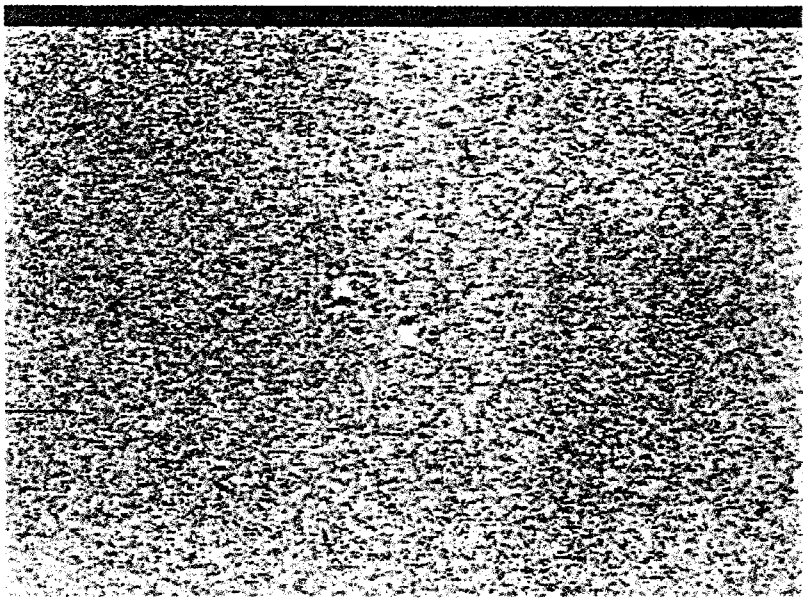

(b)

Figure 3.8. Optical reconstruction of (a) Circle and (b) Square. The white-light hologram was displayed by means of a liquid crystal television and optically re-transformed.

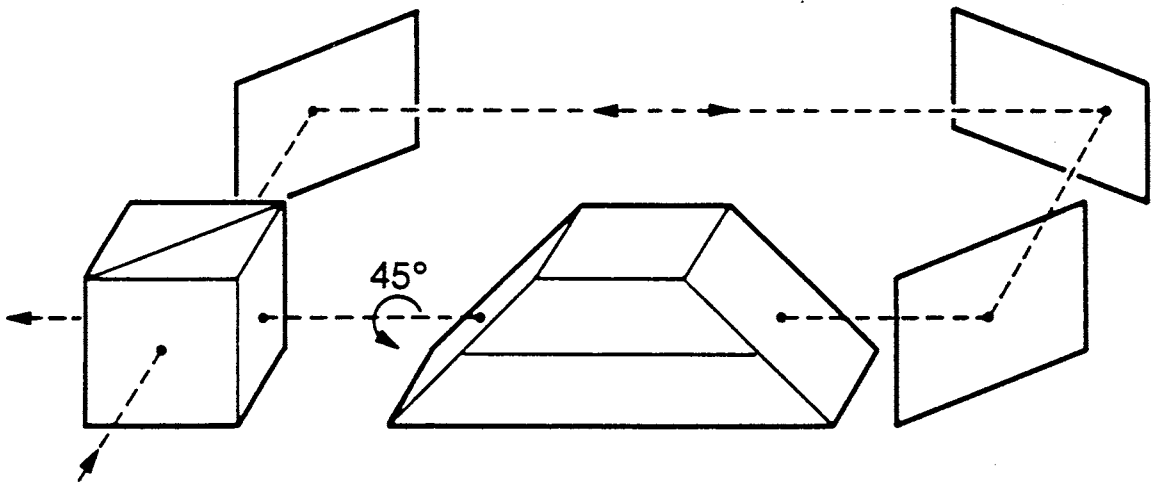

Figure 3.9. The rotational shear Sagnac interferometer. A rotation of $\pi/4$ of the dove prism about its axis rotates each beam by $\pi/2$ in an opposite direction, to have a total shear of π.

4. COMPUTER ANALYSIS OF FRINGES

Fourier-transform techniques were applied to map the complex fringe visibility in several types of interferograms. A Gershberg-type iterative technique is used to eliminate edge effects. Results are presented in this section for two specific cases: seeing measurements and interferometric tests. A third application is given in §5 regarding signal-to-noise limitations.

Mapping the amplitude and/or phase of fringes displayed on an interferogram is important for the reconstruction of an image from a fringe pattern. Figure 4.1 shows three examples of interferograms we have analyzed. The application and the way they have been obtained is discussed below. Interferogram (c) requires mapping of the fringe phase, interferogram (b) requires mapping of the fringe amplitude, and interferogram (a) requires both.

We have worked mainly on interferograms of type (a) which are clearly the most challenging. The interferogram in Figure 4.1a was recorded in 1980, in a plane conjugate to the entrance pupil of the 3.6 m CFH telescope in Hawaii, using a portable rotation-shearing interferometer of design similiar to that used within the laboraotry brassboard. The telescope was illuminated with light from the star alpha Ori (Betelgeuse). The distortion of the fringes due to atmospheric turbulence was frozen in a 1/60th of a second exposure through a 4-stage image intensifier. Photon shot-noise is the main source of noise apart from atmospheric perturbations. Mapping the amplitude and the phase of the fringes on the interferogram and averaging the result over many such interferograms, yields an estimate of the complex coherence function of the unperturbed wave-front, the Fourier transform of which gives a reconstructed image of the star.

Fourier transform techniques were used to reduce such interferograms. The two-dimensional algorithms used are described by C. Roddier [1979] and the results on the first laboratory tests are presented by F. Roddier and C. roddier [1978], C. Roddier and F. roddier [1979], and F. Roddier [1979]. Astronomical results are presented by C. Roddier and F. roddier [1983] and F. Roddier and C. roddier [1985]. In 1982, Takeda *et al.* [1985] suggested applying a similar method for the reduction of interferometric tests but using only one-dimensional Fourier transforms. Macy [1983] made tests showing the accuracy of the method. Nugent [1985] discussed the effect of sampling and detector non-linearities. Recently Bone *et al.* [1986] developed a two-dimensional algorithm and suggested a technique for reducing phase errors produced by the boundaries.

We present here our latest approach to the problem. Our algorithms were developed to estimate both the amplitude and the phase of the fringes (yielding the modulus and the phase of the holographically recorded object Fourier transform). We have recently applied our algorithms to simpler cases, namely the reduction of interferometric seeing measurements, i.e. the estimation of the fringe amplitude only from interferograms such as the one displayed in Figure 4.1b and the reduction of interferometric tests, i.e. estimation of the fringe phase only from interferograms such as the one displayed on Figure 4.1c. It is the reduction of the interferogram for reconstruction of images in the laboratory brassboard that is of interest for the SNR. The NSF supported the analysis and reduction of the astronomical images. We present here results obtained for these two applications only.

4.1 Theory

The irradiance distribution in a general interferogram can be described as

$$I(\mathbf{r}) = D(\mathbf{r})A(\mathbf{r})\{1 + V(\mathbf{r})\cos[2\pi\mathbf{f}_0 \cdot \mathbf{r} - \phi(\mathbf{r})]\} \qquad 4.1$$

$D(\mathbf{r})$ describes the domain D over which the interferogram extends:

$$D(\mathbf{r}) = \begin{cases} 1, & \text{inside the pupil;} \\ 0, & \text{otherwise.} \end{cases} \qquad 4.2$$

(a)

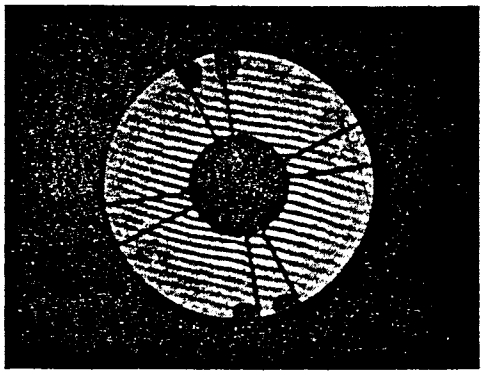

(b)

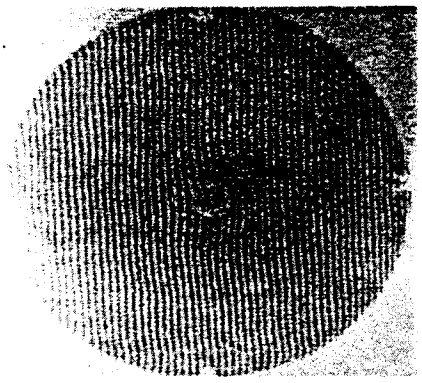

(c)

Figure 4.1. Examples of interferograms. (a) stellar interferogram, (b) interferometric seeing measurement, (c) interferometric test.

$A(\mathbf{r})$ will be referred to as the continuum. We assume that it can be determined independently inside the domain D. Methods to determine the continuum will be discussed in §4.3. $\mathbf{f_0}$ is a reference spatial frequency usually taken as the average or undisturbed fringe frequency. $V(\mathbf{r})$ and $\phi(\mathbf{r})$ are to be determined from the interferogram. $V(\mathbf{r})$ is the local fringe visibility and $\phi(\mathbf{r})$ is the local fringe phase with respect to the reference frequency $\mathbf{f_0}$. Equation 4.1 can be written

$$\begin{aligned} I(\mathbf{r}) &= D(\mathbf{r})A(\mathbf{r})[1 + Re\{C(\mathbf{r})e^{2i\pi\mathbf{f_0}\cdot\mathbf{r}}\}] \\ &= D(\mathbf{r})A(\mathbf{r})[1 + \frac{1}{2}C(\mathbf{r})e^{2i\pi\mathbf{f_0}\cdot\mathbf{r}} + \frac{1}{2}C(\mathbf{r})e^{-2i\pi\mathbf{f_0}\cdot\mathbf{r}}] \end{aligned} \qquad 4.3$$

where $C(\mathbf{r})$, often called the complex fringe visibility, is defined as

$$C(\mathbf{r}) = V(\mathbf{r})e^{-i\phi(\mathbf{r})}. \tag{4.4}$$

The problem is to determine $C(\mathbf{r})$ from $I(\mathbf{r})$. The Fourier transform of $I(\mathbf{r})$ is

$$i(\mathbf{f}) = d(\mathbf{f}) * a(\mathbf{f}) * [\delta(\mathbf{f}) + \frac{1}{2}c(\mathbf{f} - \mathbf{f_0}) + \frac{1}{2}c^*(-\mathbf{f} - \mathbf{f_0})], \tag{4.5}$$

where the asterisk ($*$) denotes a convolution product, the asterisk superscript (*) denotes a complex conjugate, and $\delta(\mathbf{f})$ represents a Dirac impulse distribution.

Let us consider first the ideal case of an infinite interferogram with a uniform continuum ($A(\mathbf{r}) = D(\mathbf{r}) = -1$ for all $\mathbf{r}$). In this case the Fourier transform of the interferogram reduces to the last convolution factor in Equation 4.5, i.e. to the three following terms: a Dirac impulse $\delta(\mathbf{f})$ at the origin and two terms shifted from the origin and centered at frequency $+\mathbf{f_0}$ and $-\mathbf{f_0}$, the Fourier transform of the complex fringe visibility and its transposed complex conjugate. This clearly shows that the complex fringe visibility can be unambiguously determined only as long as $C(\mathbf{r})$ is a band-limited function, with a frequency cutoff $\mathbf{f_c}$, and $|\mathbf{f_0}|$ is taken larger than $\mathbf{f_c}$. This condition holds whatever the method is used to determine the fringe amplitude and/or phase. Here we will assume that it is satisfied in all that follows.

The complex fringe visibility can be obtained by setting to zero all the points in the closed half part of the frequency plane opposite $\mathbf{f_0}$, shifting the result by an amount $-\mathbf{f_0}$ back to the origin and taking an inverse Fourier transform. This is nothing else than a generalization in two dimensions of a standard technique in wave processing. The interferogram can be considered as an amplitude and/or phase modulated two-dimensional sinusoid. The process of recovering the fringe amplitude and/or phase is a demodulation process. Setting to zero half of the frequency plane yields the Fourier transform of the associated analytic signal and shifting the result by an amount $-\mathbf{f_0}$ eliminates the carrier frequency.

Difficulties arise from the fact that any interferogram has a finite extent and generally, the continuum is not uniform. Since $D(\mathbf{r})$ has a bounded support its Fourier transform $d(\mathbf{f})$ is analytic and therefore extends to infinity. After convolution with $d(\mathbf{f})$ and $a(\mathbf{f})$ in Equation 4.5, the three terms described above now overlap producing errors in the determination of the complex fringe visibility. The extended wings may also produce significant aliasing errors associated with the use of discrete Fourier transforms. In §4.2 we discuss how to correct for continuum nonuniformities and in §4.3, we propose new ways to deal with the finite extent of the interferogram.

4.2 Estimation of the continuum

We found that fluctuations of the continuum $A(\mathbf{r})$ due to imperfections in the optics often seriously affect the data. An independent measure of the continuum is therefore necessary if one seeks an accurate estimate of the fringe visibility. Some interferometric systems provide two outputs with fringes in opposite phase, in which case the continuum is easily obtained by simple addition of the two output frames. Dividing $I(\mathbf{r})$ by $A(\mathbf{r})$ eliminates the effect of the continuum nonuniformities and considerably improves the final result. We have devised and implemented three different techniques to estimate the continuum.

Use of a frame without fringes. For our seeing measurements, fringes were obtained with broad band light. In this case, it is easy to introduce an optical path difference in the two arms of the interferometer to make fringes disappear. The resulting illumination may slightly differ from that of the continuum in the interferogram. We found that the best results were obtained by taking the Fourier transform of the interferogram, removing from it two spectral windows

centered at frequencies $+\mathbf{f}_0$ and $-\mathbf{f}_0$ where most of the fringe signal is located, and replacing them with the corresponding values obtained from the Fourier transform of the frame without fringes (appropriately weighted). Our estimate of the continuum is obtained by taking the inverse Fourier transform of the result. Figure 4.2 shows an example such a correction. Figure 4.2a shows a scan across one line of the raw data (interferogram). Figure 4.2b shows the fluctuations of the continuum estimated as described above. Figure 4.2c shows the result of the division $I(\mathbf{r})/A(\mathbf{r})$. The improvement is clearly apparent.

Use of a frame with different fringe orientation. With narrow band laser light, the above procedure is no longer applicable. However another frame can be taken with fringes oriented at 90° from the previous one. In this case, we take the Fourier transform of the first interferogram, remove as above two windows centered at frequencies $+\mathbf{f}_0$ and $-\mathbf{f}_0$, and replace them with the corresponding values obtained from the Fourier transform of the second interferogram which are essentially free from fringe signal. Figure 4.1c shows an interferogram of a 1.8m telescope mirror under test at NOAO. The interferogram was taken with a scatter plate interferometer [Burch 1953, Scott 1969]. The fringe amplitude is clearly non-uniform. A second interferogram (not shown) was taken with fringes oriented at 90°. The continuum was estimated as described above. Figure 4.3a shows the result of the division $I(\mathbf{r})/A(\mathbf{r})$.

Use of symmetries. When no other frame is available, one can still make use of the symmetry properties of the interferogram. If the shape of the interferogram is invariant under a 90° rotation, one can still remove, as described above, two spectral windows where the fringe signal is concentrated, and replace them by the corresponding values taken on the same Fourier transform after a 90° rotation. We applied this technique in some cases to incoherent holograms.

4.3 The boundary problem

As shown in the beginning of §4, the boundaries of the interferogram are an important source of errors if they are not properly taken into account. This was also noted by Bone *et al.* [1986]. The discontinuities of $D(\mathbf{r})$ at the edge of the interferogram produce large ripples in which dominate the Fourier transform of the interferogram. A way to deal with this problem is to extrapolate the interferogram beyond its limits. Indeed if the Fourier transform $c(\mathbf{f})$ of the complex fringe visibility $C(\mathbf{r})$ has a bounded support as assumed above, $C(\mathbf{r})$ is analytic and can therefore be uniquely extrapolated beyond the interferogram limits by analytic continuation. In 1974, Gerchberg [1974] proposed a simple iterative algorithm for analytic continuation. We have applied Gershberg's method to extrapolate the interferograms.

The algorithm works as schematically described in Figure 4.4. After division by the continuum, we first subtract unity inside the interferogram. According to Equation 4.1, we get

$$\begin{aligned} J(\mathbf{r}) &= \frac{I(\mathbf{r})}{A(\mathbf{r})} - D(\mathbf{r}) \\ &= D(\mathbf{r})V(\mathbf{r})\cos[2\pi\mathbf{f}_0 \cdot \mathbf{r} - \phi(\mathbf{r})], \end{aligned} \tag{4.6}$$

the Fourier transform of which is

$$j(\mathbf{f}) = d(\mathbf{f}) * [\frac{1}{2}c(\mathbf{f} - \mathbf{f}_0) + \frac{1}{2}c^*(-\mathbf{f} - \mathbf{f}_0)]. \tag{4.7}$$

If the interferogram was infinite, $j(\mathbf{f})$ would be entirely concentrated inside two circles centered at $+\mathbf{f}_0$ and $-\mathbf{f}_0$ and with radius $\mathbf{fc}$ [the frequency cutoff of $c(\mathbf{f})$]. The algorithm consists of setting to zero all the values outside these two circles. The inverse Fourier transform of the result produces an interferogram with extrapolated fringes. The values inside the interferogram are replaced by

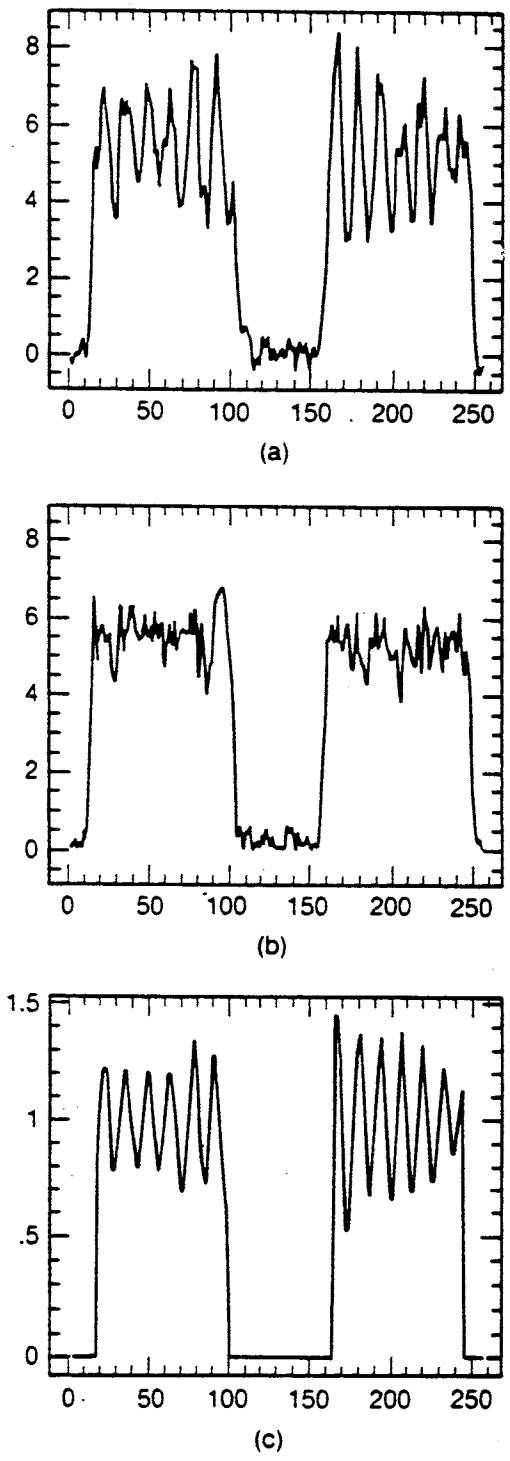

Figure 4.2. Seeing measurements: correction for the fluctuations of the continuum. (a) raw data, (b) estimated continuum, (c) corrected data.

the original values. The extrapolated values are kept as they are. The new interferogram is Fourier

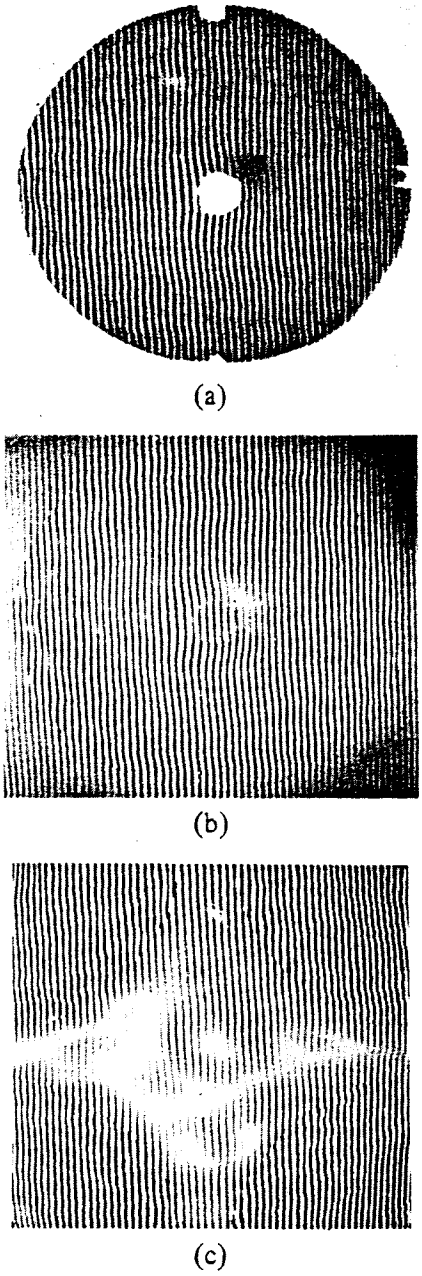

(a)

(b)

(c)

Figure 4.3. Processing of the interferometric test. (a) after sampling and correction for the continuum, (b) after extrapolation of the fringes, (c) same as (b), but shifted by half a period.

transformed and the procedure is repeated until most of the energy becomes concentrated inside the two circles. This usually takes only a few iterations. The fringe pattern inside the interferogram remains unchanged. It is only extrapolated outside the interferogram limits which prevent the two terms in the Fourier transform from overlapping. Figure 4.3b shows an extrapolation of the fringes displayed in Figure 4.3a. The two fringe patterns are identical inside the interferogram boundaries.

A discrete Fourier transform must be thought of as the Fourier transform of a periodic function, i.e. in two dimensions, of a plane tiled with interferograms all adjacent and identical. The algorithm described above not only extrapolates the fringes but also nicely interpolates them from one period to another thus avoiding any discontinuity in the periodic tiling. Figure 4.3c is identical to Figure

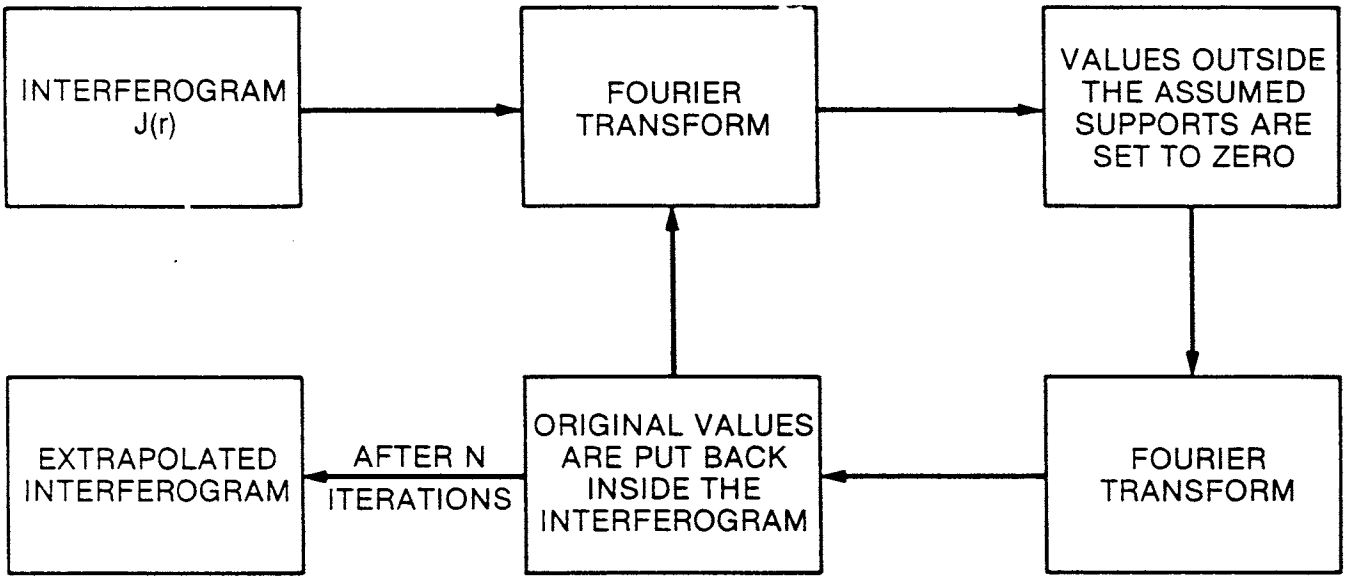

Figure 4.4. Gerchberg's extrapolation algorithm.

4.3b but for a shift of one half period in both directions. It clearly demonstrates the continuity of the interpolation. Methods previously proposed to extrapolate the fringes do not have this property Bone *et al.* [1986]. Because the periodic tiling is continuous, the energy is highly localised in the Fourier transform plane and aliasing errors due to finite sampling are avoided.

4.4 Phase unwrapping

The phase of the complex fringe visibility, also called the wrapped phase is defined on a circle, modulo 2π. For some applications, such as image reconstruction through turbulence [McGlammery 1971, Itoh 1982, Itoh and Ohtsuka 1983, Mertz 1984, 1985], or wave-front reconstruction [Takeda *et al.* 1982, Macy 1983, Fried 1977, Hudgin 1977, Hunt 1979] it is necessary to compute an unwrapped phase, defined on the real axis. Mathematically, the unwrapped phase is defined as the integral of the derivative of the wrapped phase. In practice, due to finite sampling, an unwrapped phase is obtained by summing phase differences. As discussed by Itoh [1983], in one dimension this is possible only if the true phase jumps are smaller than π, i.e., if the true phase differences range between $-\pi$ and $+\pi$.

Takeda *et al.* [1982] and Macy [1983] compute phase differences from the phase of the complex fringe visibility. It is equivalent but more elegant to compute the sine and the cosine of the phase differences from the real and imaginary part of the complex visibility yielding automatically phase differences ranging between $-\pi$ and $+\pi$, which can be directly summed without bothering about phase jumps. As shown by Itoh and Ohtsuka [1983], turbulence effects are best removed by averaging sine and cosine of phase differences computed as above.

Unfortunately, when the fringe contrast is low or the interferogram is noisy, as in the example of Figure 4.1a, phase jumps larger than π often occurs and none of the methods described above works. Tribolet [1979] proposed to unwrap the phase with an adaptive sampling interval. In two dimensions one may use many different integration paths and use the constraint that each path should yield the same result. Least square algorithms have been proposed to integrate two-dimensional wave-front slopes [Fried 1977, Hudgin 1977, Hunt 1979]. Unfortunately they do not

take properly into account the statistics of the errors on phase differences, namely the fact that a small error on the complex fringe visibility may produce nearly a 2π error on the phase difference producing dislocations in the reconstructed wave-front surface. We have written a two-dimensional phase unwrapping algorithm which seeks to find and correct these dislocations [REF 1]. Recently Ghiglia *et al.* [1986] proposed a two-dimensional phase unwrapping algorithm based on cellular automata which may also isolate dislocations.

4.5 Results on seeing measurements

Figure 4.1b shows an example of seeing measurements made with a rotational-shear interferometer. The interferometer and this application are described in C. Roddier [1976] and C. Roddier *et al.* [1977]. Fringes are photographically recorded in a plane conjugate to the entrance pupil of a 50-cm astronomical telescope illuminated with a bright star. The film is photometrically calibrated. The interferometer produces two images of the telescope pupil rotationally sheared about their center. Clearly, the fringe visibility decreases as the baseline for interference increases from the center to the edge, showing the loss of coherence produced by atmospheric turbulence on exposures of the order of a few tens of seconds. The shear angle can be adjusted to match the coherence length with the interferogram size. The optical band-width was limited by an interference filter to $\approx$ 100Å.

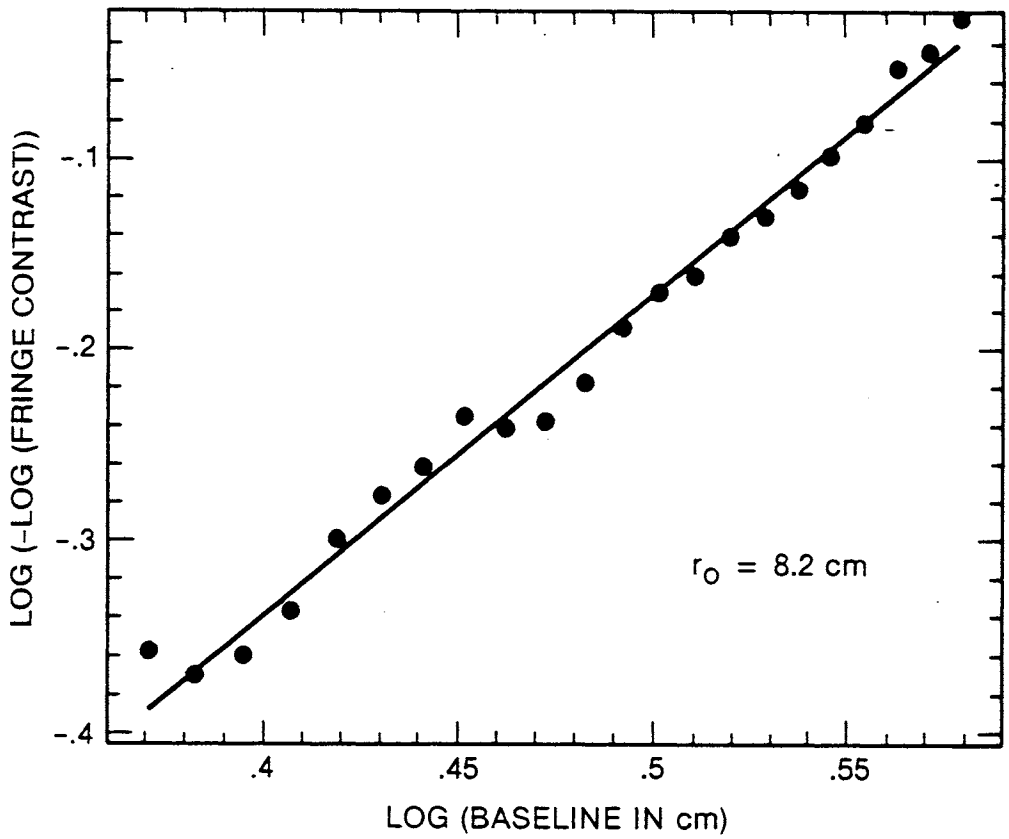

Figure 4.5. Seeing measurements: plot of the log-log visibility *vs* log base line. (dots) and 5/3 slope best fit (full line).

The algorithms described above were used to map the fringe visibility on such interferograms.

Theory predicts that the fringe visibility should decrease with the baseline $\mathbf{r}$ as [Roddier 1981]

$$V(\mathbf{r}) = e^{-3.44(|\mathbf{r}|/r_0)^{5/3}}, \qquad 4.8$$

where r_0 is a parameter called Fried's parameter which is a measure of the seeing quality of the atmosphere. Figure 4.5 is a plot of the observed log of the log visibility as a function of the log baseline together with a 5/3 slope best fit showing how well the 5/3 law in Equation 4.8 is verified. We estimate that the method yields a determination of r_0 with a few percent accuracy.

4.6 Results on interferometric tests

The same methods were applied to scatter plate interferograms used to control the figure of large mirrors under test at NOAO. Figure 4.1c shows such an interferogram obtained on a 1.8-m mirror with a honeycomb structure. The reference wave was highly tilted in order to enable us to recover small details on the wave-front surface. Figure 4.3a-c show intermediate steps of the process as described above. Because fringes have a large amplitude at the edge of the interferogram, the use of Gerchberg's extrapolation was found to be especially important.

Figure 4.6a shows a map of the wave-front slope along the horizontal direction reconstructed from the interferogram in Figure 4.1c. Such a display simulates the result of a knife-edge test. For comparison, Figure 4.6b shows the result of a real knife-edge test made on the same mirror a few months before. Clearly the two results are in excellent agreement. Small differences can be attributed to the effects of atmospheric turbulence in the laboratory which does not average out in a single short exposure interferogram. These effects can be removed by averaging the results of several interferograms.

Figure 4.7 shows a plot of one line of the reconstructed wave-front taken near the center of the 256 computed lines. The phase was unwrapped without difficulty using the simple one-dimensional algorithm described in §4.4. Because of the high amplitude of the fringes and the high signal-to-noise ratio of the data, it was not necessary to use more robust two-dimensional algorithms. However it is worth mentioning that, when the same data were processed without Gerchberg's extrapolation, the simple one-dimensional algorithm did not work, showing evidence for phase errors. The peak-to-valley amplitude displayed on Figure 4.7 is of the order of half a wave. The small ripples related to the honeycomb structure have an amplitude of typically one-tenth of a wave, corresponding to 0.03-5μm bumps on the mirror surface. The horizontal resolution on the mirror is 3 cm. We have therefore been able to reconstruct the wave-front with interferometric accuracy, while achieving a spatial resolution comparable to that of a knife-edge test.

(a)

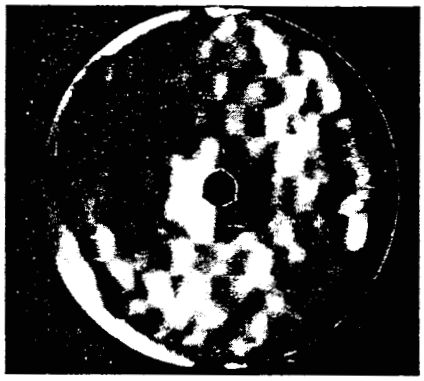

(b)

Figure 4.6. Wave-front slopes derived from 4.1c and knife-edge test on the same mirror.

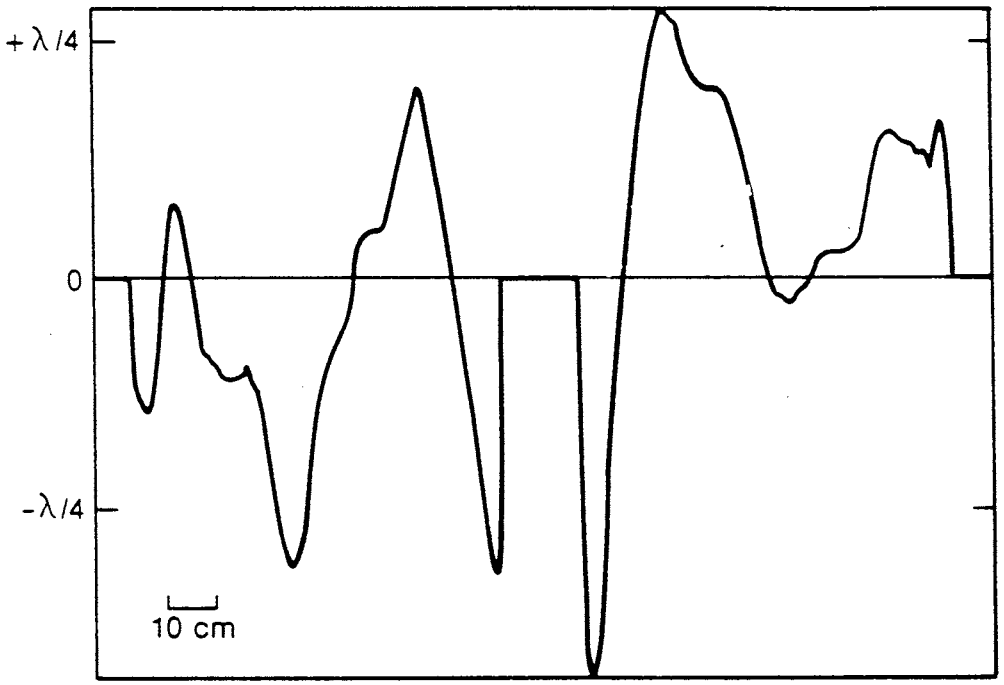

Figure 4.7. Horizontal cut of the reconstructed wave-front in Figure 4.6 (near the center).

5. SIGNAL TO NOISE RATIO

The signal-to-noise ratio of the reconstruction from white light Fourier transform was calculated theoretically. It was found to depend on the signal-to-noise ratio of the original transform, the object complexity and the number of pixels in the detector. We are able to verify this relationship experimentally. We found slight excursions from the predicted values only at the least complicated objects, namely ones that contained less than four resolvable elements in them.

A simple derivation is given for the signal-to-noise ratio (SNR) in images reconstructed from incoherent holograms. Dependence is shown to be on the hologram SNR, object complexity and the number of pixels in the detector. Reconstruction of involved objects becomes possible with high dynamic range detectors such as CCDs. We have produced such white light holograms, by means of a rotational shear interferometer, combined with a chromatic corrector. A digital inverse transform recreated the object.

Incoherent optical Fourier transforms have an advantage over coherent transforms in that they can be performed on natural white light scenes, as well as on simple input devices (CRTs, image intensifiers). They are also less sensitive to coherent noise and to system vibrations. In this section we investigate the noise characteristics of such transforms.

An incoherent optical Fourier transform is obtained when each point of an incoherent object produces a distinct sinusoidal fringe pattern. The incoherent addition of all the fringe patterns produces the object Fourier transform. This is the case when an interferometer gives two images of an incoherent object, one being rotated with respect to the other. Let $o(\mathbf{x})$ be the irradiance distribution in the incoherent object. Without loss of generality we shall assume that the object is at infinity so that $\mathbf{x}$ is a pair of angular coordinates expressed in radians. The irradiance distribution $I(\mathbf{r})$ in the hologram can be written in a general way

$$I(\mathbf{r}) = O(0) + Re\{O(k\mathcal{R}\mathbf{r}/\lambda)\} \qquad 5.1$$

where $o(.)$ is the Fourier transform of $O(.)$, k is a magnification factor, $\mathcal{R}$ a rotation operator and λ the wave-length (notice that we have switched capital notation from the rest of this report, i.e. that functios in the hologram plane are now in capitals.) The Fourier transform $i(.)$ of the irradiance distribution in the hologram gives

$$(k/\lambda)^2 i(k\mathcal{R}^{-1}\mathbf{x}/\lambda) = O(0)\delta(\mathbf{x}) + \frac{1}{2}[o(\mathbf{x}) + o(-\mathbf{x})] \qquad 5.2$$

where $\mathcal{R}^{-1}$ is the inverse rotation and $\delta(\mathbf{x})$ is a Dirac distribution. Equation 5.2 shows that the object can be recovered from the hologram as long as it does not overlap with its mirror image with respect to the interferometer axis. Another limitation is that the transform has to be either narrow band or chromatically corrected in order to utilize the polychromatic nature of real-life objects (and increase the signal-to-noise ratio of the transform). Many efforts have been conducted [C. Roddier *et al.* 1980, George and Wang 1984, Wang and George 1985, Leith and Angell 1985] towards a solution to this limitation. For involved objects, the DC component (which may also include scattered light) creates a demand for a high dynamic range detector.

Incoherent holography might be called as well "Fourier transform imaging" since it is formally similar to Fourier transform spectroscopy [Connes 1970], time being here replaced with a two-dimensional space variable. Theoretical analyses of Fourier transform spectroscopy directly apply to Fourier transform imaging.

5.1 Theory

The signal-to-noise ratio (SNR) for the reconstructed image has been discussed by Lowenthal *et al.* [1970]. Here we adapt a derivation due to Mertz [1965] for the SNR in Fourier transform

spectroscopy. The noise n_o in the reconstructed image is a scaled version of the Fourier transform of the noise N_I in the hologram. According to Equation 5.2, Parseval theorem gives

$$\int |N_I(\mathbf{u})|^2 d\mathbf{u} = (\lambda/k)^2 \int |n_o(\mathbf{x})|^2 d\mathbf{x} \qquad 5.3$$

which can be written

$$\overline{N}_I^2 A = (\lambda/k)^2 \overline{n}_o^2 a' \qquad 5.4$$

where A is the hologram area and a' is the mean area over which noise extends in the plane of the reconstructed image. $\overline{N}_I$ and $\overline{n}_o$ are the average r.m.s. noises in the hologram and in the reconstructed image respectively. We assume here that the reconstructed image is obtained from Equation 5.2, although taking the real part of it would reduce the noise by a factor $\sqrt{2}$.

Let a be the area over which the reconstructed image extends. The average signal in the image is

$$\overline{o} = \frac{1}{a} \int o(\mathbf{x}) d\mathbf{x} = \frac{O(0)}{a} = \frac{\overline{I}}{a} \qquad 5.5$$

where $\overline{I}$ is the average illumination in the hologram (Equation 5.1). We estimate the SNR for the reconstructed image as

$$\Theta_{rec} = \frac{\overline{o}}{\overline{n}_o} \qquad 5.6$$

Putting 5.4 and 5.5 into 5.6 yields

$$\Theta_{rec} = \frac{\sqrt{a'}}{a\sqrt{A}} \frac{\lambda}{k} \frac{\overline{I}}{\overline{N}_I} \qquad 5.7$$

Since the smallest resolved area in the image plane is $(\lambda/k)^2 A^{-1}$, one can introduce in Equation 5.7 the number $M = (k/\lambda)^2 aA$ of resolved pixels in the image, yielding

$$\Theta_{rec} = \frac{\sqrt{a'}}{\sqrt{A}} \frac{1}{\sqrt{M}} \frac{\overline{I}}{\overline{N}_I} = \frac{\sqrt{a'}}{\sqrt{a}} \frac{1}{\sqrt{M}} \Theta_{hol} \qquad 5.8$$

where Θ_{hol} is the SNR for the hologram. Equation 5.8 is formally equivalent to that derived by Lowenthal *et al.* [1970]. Assuming detector pixels with statistically independent noise, the noise to image area ratio a'/a in the reconstruction is also the ratio of the number P of independent pixels in the detector to the number of independent samples in the hologram. In order to reduce the noise, we wish the noise area a' to be as large as possible (Equation 5.4) compared to the image area. The factor $\sqrt{a/a'}$ shows that the SNR in the reconstructed image can be improved at will by averaging each sample of the hologram over a larger number of detector pixels. Equation 5.8 now gives

$$\Theta_{rec} = \frac{\sqrt{P/M}}{\sqrt{M}} \Theta_{hol} = \frac{\sqrt{P}}{M} \Theta_{hol} \qquad 5.9$$

5.2 Discussion

Equation 5.9 holds for any kind of noise (as long as different pixels have statistically independent noise). It shows that the SNR in the reconstructed image decreases when the image complexity increases [Kozma and Massey 1969]. For a given detector (given P) and a given object total flux (given Θ_{hol}), it is proportional to the inverse of the number M of bright pixels resolved in the object, defined as (Equation 5.5)

$$M = aA = \frac{A}{\overline{o}} \int o(x) dx \qquad 5.10$$

If the object total flux increases as M, keeping constant the object brightness, one can match the detector size to the object size ($P \approx M$), keeping constant Θ_{hol}. In this case the SNR will decrease with image complexity M only as $1/\sqrt{M}$.

When photon noise is the main source of noise, one has

$$\Theta_{hol} = \sqrt{N/P} \qquad 5.11$$

where N is the total number of photons detected. Putting Equation 5.11 into Equation 5.9 gives

$$\Theta_{rec} = \frac{\sqrt{N}}{M} \qquad 5.12$$

which is independent of the number of pixels in the detector.

In all cases, the maximum achievable SNR in the reconstructed image depends upon the number of detector pixels P and upon the maximum achievable SNR in the detector which is determined by its saturation level:

$$(\Theta_{rec})_{max} = \frac{\sqrt{P}}{M}(\Theta_{hol})_{max} \qquad 5.13$$

Current CCD chips can store up to 160,000 photoelectrons before saturating which gives

$$(\Theta_{hol})_{max} = 400.$$

Hence a commercially available 2,048×2,048 pixel CCD can holographically record a 100×100 pixel image with a SNR

$$(\Theta_{rec})_{max} = \frac{2048 \times 400}{10,000} = 82 \qquad 5.14$$

5.3 Experiment

We employed the rotational shear interferometer in order to verify the dependence of the SNR on image complexity, measured by the parameter M. Incoherent holograms were recorded with the CCD camera using the 512×320 pixel detector. However only 256×256 pixels were used for the image reconstruction. The holograms were recorded with broad band white light by using the color corrector, and the DC bias was efficiently removed by the phase flipping method.

We needed an object with a varying and definable degree of complexity. For this purpose, we drilled a large number of round, identical holes in a metal plate at random locations. We masked them all with a black tape, and then unmasked a growing number of holes from the center outward for each hologram. Since the fully exposed mask was very large, the illumination of the holes was slightly different between the center and the outer side. The object had therefore more than the initially expected two levels of illumination. We estimate the number a'/a of detector pixels per independent area in the hologram to be about ten for the maximum number of holes (sixty).

The holograms were digitized with a dynamic range of up to 4000 levels. The gain was approximately forty photons/level. The read-out noise was low (up to 0.025 of the full range) and was therefore negligible compared to photon noise. In order to utilize the full dynamic range, different exposure times were used for different number of holes. The hologram difference shown in Figure 5.1 was obtained with 40 holes. Hologram differences were Fourier transformed digitally to reconstruct the original object and its twin image. Figure 5.2 shows the image reconstructed from the hologram of Figure 5.1. The noise level in the reconstructed image was measured outside the object extent, and was found to be uniform all over the reconstruction area as expected.

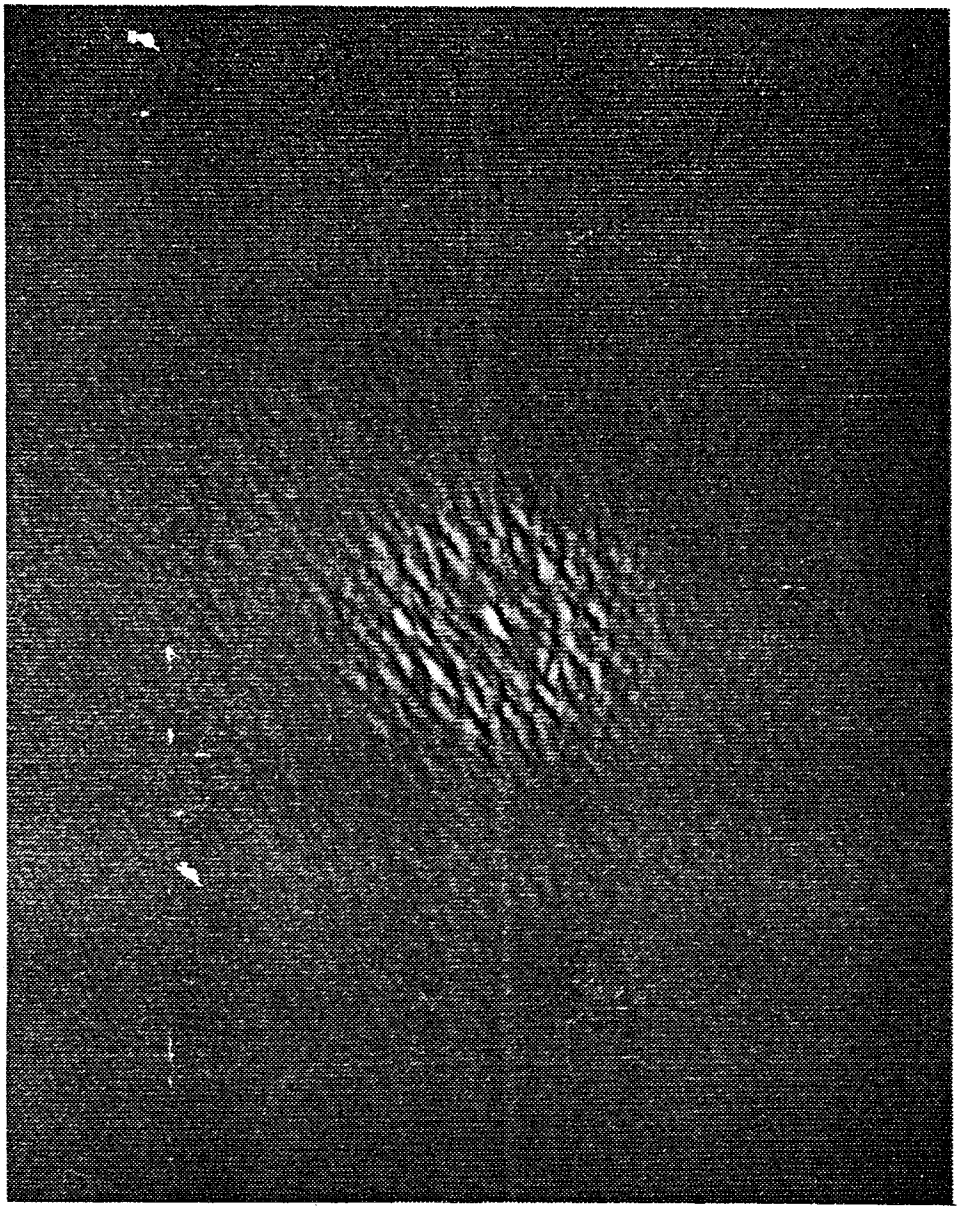

Figure 5.1. Incoherent hologram recorded with broad band white light. The D.C. bias has been removed (background grey level is zero, dark is negative, bright is positive). The object consisted of 40 bright dots.

Since the object had more than two levels of illumination, we defined the object area as the area over which, in each reconstructed point, the signal was above some fraction of its maximum value. The results given below were found widely independent of the fraction chosen. This area expressed in number of pixels was taken as our measure of the object complexity M. The SNR in the reconstructed image was obtained by taking the ratio of the signal (averaged over the above defined area) to the r.m.s. noise (measured outside the reconstructed object as indicated by Equation 5.5).

Assuming pure shot noise, the noise in the hologram was taken as the square root of the average illumination expressed in detected photons per pixels, and the signal was taken as the maximum amplitude of the fringes also expressed in photon units. The SNR in the reconstructed image was

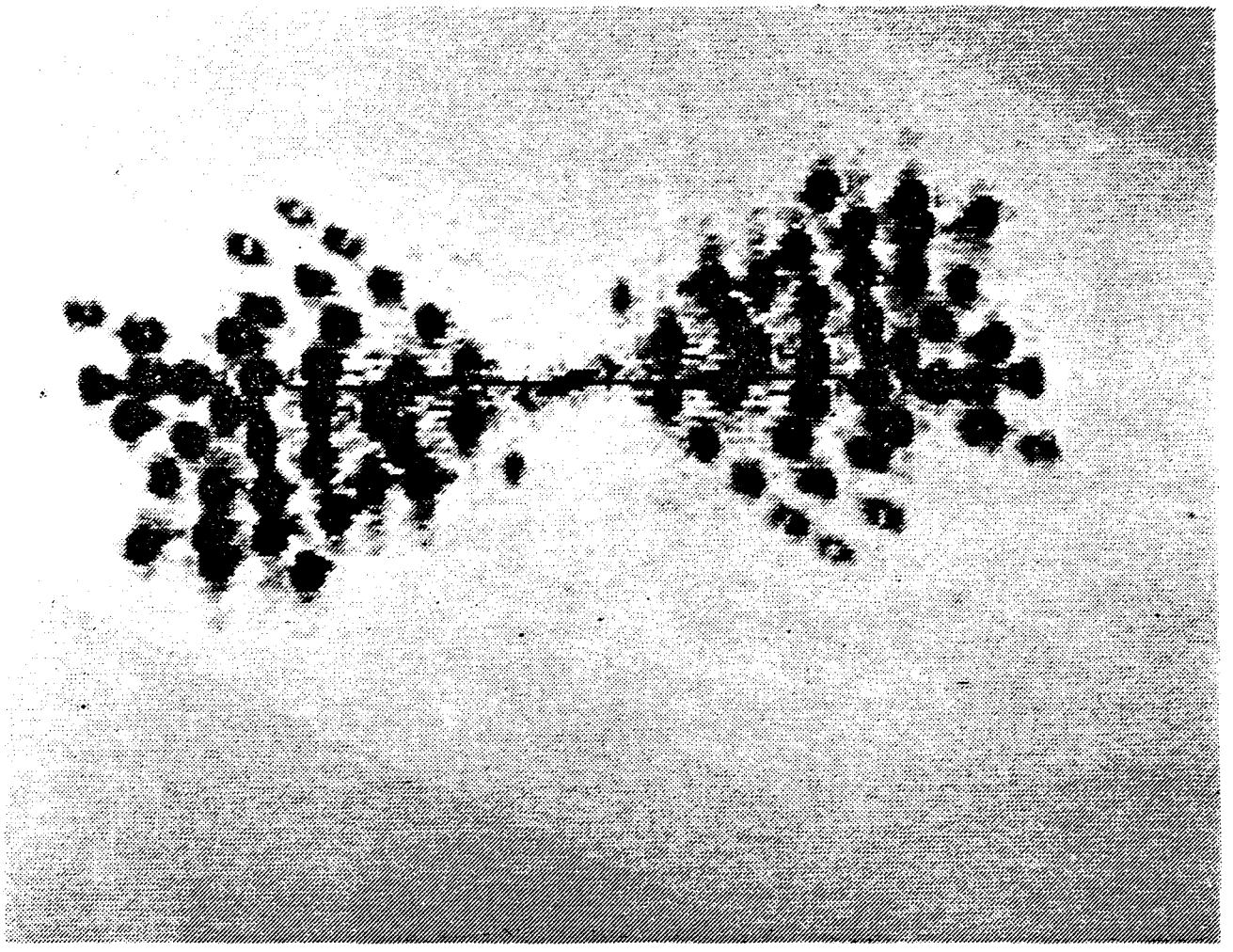

Figure 5.2. Reconstructed image obtained by computing the two-dimensional Fourier transform of the hologram displayed on Figure 5.1. The picture is a negative with reduced dynamic range to better show the noise distribution.

then divided by the SNR in the hologram and plotted as a function of M in a log-log scale as shown on Figure 5.3. It is clear that for a large object complexity the $1/M$ dependence predicted by Equation 5.9 is well observed. However the factor of proportionality is found to be about 40, well below the factor $\sqrt{P} = 256$ predicted by Equation 5.9, i.e. the SNR in the reconstructed image is about 6.4 times lower than the expected value assuming photon noise as the only source of noise in the hologram. The discrepancy is even larger when the image complexity is small.

We believe that these discrepancies can be explained by the imperfections of the optics such as aberrations, dust and misalignment of the chromatic corrector. Such errors are highly correlated over different detector pixels and are not included in our modelization. We indeed observed that

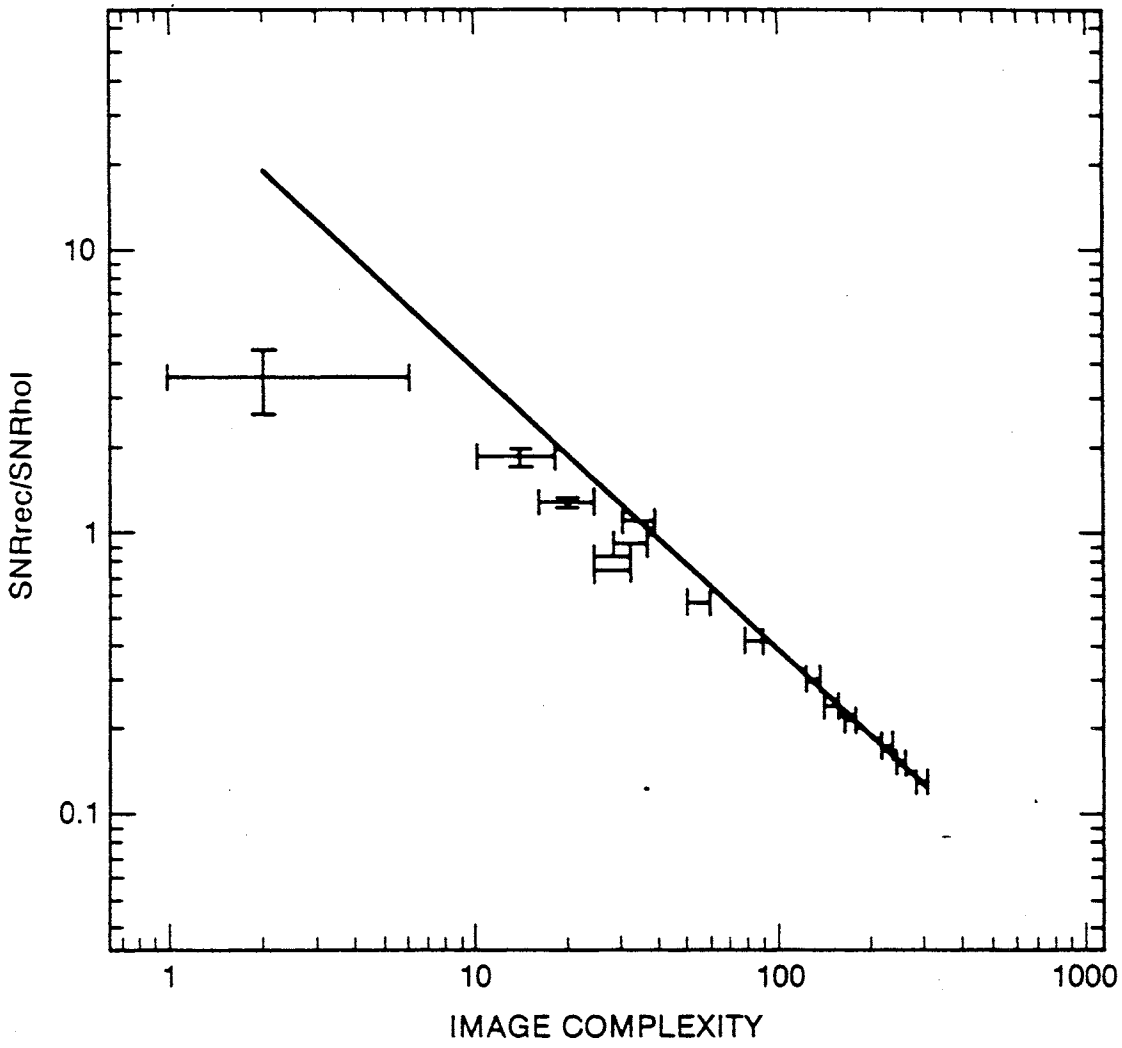

Figure 5.3. Ratio of the SNR in the reconstructed image to the SNR in the hologram as a function of the number of bright pixels in the image taken as a measure of its complexity. A minus one slope is shown for comparison with theory.

the point-spread function of the full system is a sharp spike flanked by low lying, wide side-lobes. These side-lobes divert power from what we have considered as the reconstructed image (central peaks) and therefore produce a lower SNR. When the object consists of closely packed dots the loss of signal power is less severe as observed. The situation is a close analog to that of image reconstruction in radio-astronomy where the point spread function is called the dirty beam. Deconvolution techniques such as CLEAN [Högbom 1974] can be used to produce images with an improved SNR.

6. PHASE CLOSURE IMAGE RECONSTRUCTION

In most cases, rotational shear interferometers are used at 180° shear. In this case, any perturbation of the wave-front will show symmetrically on the two opposite sides of the interferogram. Thus it will not be distinguishable from true object transform phase. This degeneracy can be removed by using other shear angles. If the shear angle is slightly different from 180°, then mere averaging over the perturbations will yield the true value of the object transform [Ribak 1987a, 1988]. If the shear angle is a simple fraction of 360° (say 120° or 72°), it can be shown that the sum of the phases over the interference points is the sum of the object phases, as the atmosphere and telescope phases cancel out (the method of phase closure). The information can then be used to reconstruct aberrated images, either by means of a single interferogram [Ribak 1987b] or the combination of two simultaneous ones [F Roddier and C Roddier 1986, 1987].

Phase closure is a radio astronomical technique that enables recovering Fourier transform phases that would otherwise be corrupted by atmospheric and instrumental errors [Pearson and Readhead 1984]. It has been suggested in the past that radio methods, such as aperture synthesis and phase closure, can be applicable to the visible region too [Rhodes and Goodman 1973, Rogstad 1968], and direct phase closure has indeed been demonstrated [Baldwin *et al.* 1985].

We rewrite Equation 2.9 as

$$\begin{aligned} i(\mathbf{r}) &= o(0) + Re\{o(2\mathbf{r}|\sin\beta/2|/\lambda)\} \\ &= o(0) + Re\{o(k\mathcal{R}\mathbf{r}/\lambda)\} \\ &= o(0) + |\Gamma(\mathbf{u})|\cos[\psi(\mathbf{u}) + \phi(\mathbf{u})] \end{aligned} \qquad 6.1$$

where $\mathbf{u} = \mathcal{R}\mathbf{r} = 2\mathbf{r}|\sin\beta/2|/\lambda$, $\Gamma(\mathbf{u})$ is the mutual coherence function and $\psi(\mathbf{u}) = arg\{\Gamma(\mathbf{u})\}$. $\phi(\mathbf{u})$ is the optical path difference (expressed in wave-length units) between the object and detector, and is due to different phase fluctuations at the two ends of the base line $\mathbf{u}$. These can be attributed to atmospheric turbulence and instrumental errors. In phase closure one chooses three vectors $\mathbf{u_1}$, $\mathbf{u_2}$, $\mathbf{u_3}$ such that $\mathbf{u_1} + \mathbf{u_2} + \mathbf{u_3} = 0$. In this case the phases must obey $\phi(\mathbf{u_1}) + \phi(\mathbf{u_2}) + \phi(\mathbf{u_3}) = 0$. When adding the total phases of the three measurements along the three vectors, one is left with the sum of the phases of the coherence function $\psi(\mathbf{u_1}) + \psi(\mathbf{u_2}) + \psi(\mathbf{u_3})$. The same theory applies to any closed loop of vectors, not just three.

If we choose a rotation angle $\beta = 120°$, we automatically create an infinite number of closure loops. Every centered equilateral triangle will constitute such a set of vectors. At each vertex of such a triangle, we have an interference of two points 120° apart on the telescope aperture (Figure 6.1a). The same applies for a rotation angle of 72°, where we now have phase closure in all possible centered pentagons (Figure 6.1b), or, for 144° shear, all possible five-pointed stars (Figure 6.1c). Since for rotation angles $\beta < 180°$ we lose the highest frequencies (between $2r|\sin\beta/2|/\lambda$ and $2r/\lambda$), we cannot have all the phases, but methods do exist that allow reconstruction of images from partial phase information [Bates and McDonnel 1986].

It is relatively easy to extract the auto-correlation of an object by either rotational shear interferometry or speckle interferometry. The former is more efficient, especially for brighter objects; it also utilises a significantly wider band-width. Now it seems that obtaining phase relations, and thus full imaging, is even more efficient when done in the pupil plane. For most rotation angles (with the notable exception of π or $\pi/2$) the true visibility phase can be decoupled from the atmospheric phase, allowing extraction of the closure phase (for $\rho = 2\pi/3, 4\pi/5, \ldots$) [Ribak 1987b] or phase relations similar to Knox-Thompson (for $\rho \approx \pi$) [Ribak 1987a, 1988]. For an exit pupil encompassing N pixels, the number of phase relations is $N\rho/\pi$, providing enough information for image reconstruction. Similar schemes have been suggested, involving more that one

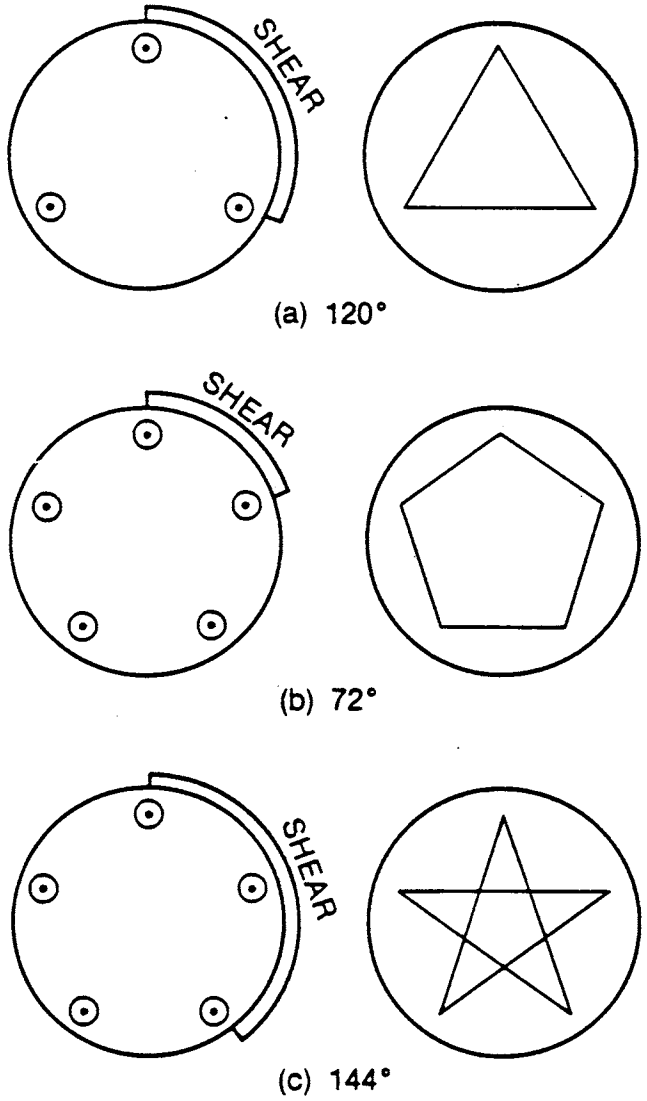

Figure 6.1. (a) Two interfering apertures at 120° shear and one set of base lines in the telescope aperture that constitutes a closure loop. (b) As in (a) with 72° rotation and pentagon. (c) As in (a) with 144° rotation and five-pointed star.

interferometer. These provide closure relations between two simultaneous interferograms obtained on the same detector [Hofmann and Weigelt 1986, 1987] or on two separate detectors [Roddier and Roddier 1986, 1987].

6.1 Closure relations.

The simplest closure case is for a 120° rotational shear. The electric field in the telescope aperture (Figure 6.2, top) is split into two, one half is rotated by 120° (Figure 6.2, middle), and the two are combined to interfere (Figure 6.2, bottom) on a detector. Every point in the resulting interference pattern corresponds now to a vector (base line) in the original aperture; thus the correlation $E_A E_B^*$ is associated with the vector **AB**, etc. Moreover, symmetrically opposite points

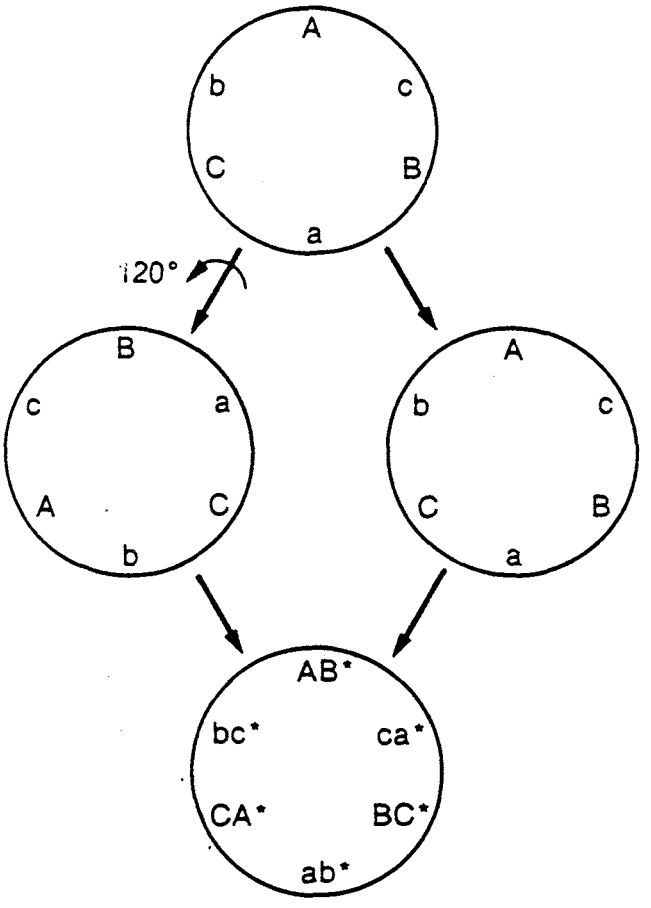

Figure 6.2. Aperture image, 120° rotational shear. Top: telescope aperture; center: split beams; bottom: recombined beams.

provide information about the same base line, with the vectors pointing the opposite way. Thus, the opposite vector $\mathbf{ab} = -\mathbf{AB}$ will yield $E_a E_b^*$. However, the phases of these points are not opposite in sign, as they are affected in a different manner by the atmosphere. In general, we get $|E_A E_B^*| = |E_a E_b^*|$. This is true for any rotation angle, but for 120° rotation we can utilise the fact that two other vectors, **BC** and **CA** (or **bc** and **ca**) create an equilateral triangle and provide phase closure. Assuming $\langle E_A \rangle = \langle E_B \rangle = \langle E_a \rangle = \cdots = \sqrt{I}$, where I is the average illumination in the hologram, we can write

$$E_A E_B^* = I\Gamma_{AB} e^{i(\phi_A - \phi_B)} \qquad 6.2$$

where Γ_{AB} is the (complex) mutual coherence function for the vector **AB**, and ϕ_A and ϕ_B are the atmosphere-induced phases at points A and B. Similarly

$$E_a E_b^* = I\Gamma_{ab} e^{i(\phi_a - \phi_b)}. \qquad 6.3$$

Multiplying the three correlations around the closure triangle (there is *no* need to conjugate one of them), we get

$$(E_A E_B^*)(E_B E_C^*)(E_C E_A^*) = I^3 \Gamma_{AB}\Gamma_{BC}\Gamma_{CA} \qquad 6.4$$

$$(E_a E_b^*)(E_b E_c^*)(E_c E_a^*) = I^3 \Gamma_{ab}\Gamma_{bc}\Gamma_{ca} = -I^3 \Gamma_{AB}\Gamma_{BC}\Gamma_{CA} \qquad 6.5$$

and all the atmospheric phases are left out of the loop. This is true for *all* equilateral triangles in the aperture. The same can be done for 72° and 144° rotations, with five multiplications at a time,

but the noise involved seems to be prohibitive (except, possibly, for the lowest spatial frequencies, where the object is unresolved and the signal is high).

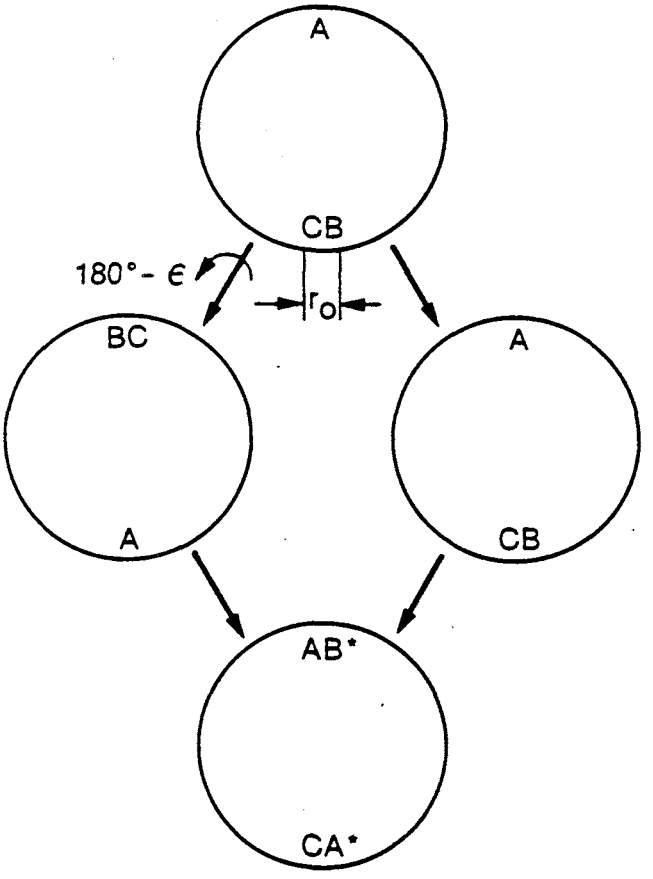

Figure 6.3. Aperture image, $180° - \epsilon$ rotational shear. Top: telescope aperture; center: split beams; bottom: recombined beams.

6.2 Phase relations.

A special case where one removes the ambiguity between the object phase and the atmospheric phase is for rotation of $180° - \epsilon$ (Figure 6.3). If the difference between two adjacent vectors **AB** and **AC** is short enough so that $\mathbf{BC} < r_o$ (Figure 6.3, top) then on combination we get

$$E_A E_B^* = I\Gamma_{AB} e^{i(\phi_A - \phi_B)} \tag{6.6}$$

$$E_C E_A^* = I\Gamma_{CA} e^{i(\phi_C - \phi_A)} \tag{6.7}$$

which we multiply to get [Ribak 1987a]

$$(E_A E_B^*)(E_C E_A^*) = I^2 \Gamma_{AB}\Gamma_{CA} e^{i(\phi_C - \phi_B)}. \tag{6.8}$$

We now average over many realisations of the atmosphere. If indeed the points B and C are close enough, the phase fluctuations between them will be small and average out [Roddier 1981]

$$\langle e^{i(\phi_C - \phi_B)} \rangle = 0 \tag{6.9}$$

in a manner very similar to that of Knox and Thompson [1974], although here the phase difference is known only for the tangential direction. The advantage of this approach is that only one multiplication is involved, compared with two in most phase closure schemes, with the attendant signal-to-noise level that one has in first- (as opposed to second-) order correlation.

6.3 Process simulation.

In order to estimate the difficulties involved with the phase closure technique, as applied in the image plane, simulations were carried out. Here is a description of the process step by step, starting with the creation of a set of interferograms.

1. Create a model star and Fourier transform it.
2. Take the square root of the atmospheric transfer function and Fourier transform it.
3. Create a frame of complex random numbers (every two frames).
4. Convolve with the above atmospheric function:
   4a. Fourier transform the random number frame.
   4b. Multiply by the atmospheric correlating function (from step 2).
   4c. Inverse Fourier transform the result.
5. Split into real and imaginary parts to get *independent* representations of the wave-front phase.
6. Subtract phase 120° away (on equilateral centred triangle) to get wave-front phase difference.
7. Add differences to mutual coherence function (obtained in step 1).
8. Take real part. This is the AC part of the interferogram.
9. Add DC component to the interferogram.
10. Multiply by the telescope aperture function.
11. Add Poisson noise at each pixel according to the intensity.
12. Next frame even: go to step 6; odd: go to step 3.

The simulations were run on a 128 × 128 array, where the telescope diameter was about 65 pixels. The following parameters were assumed: integration time 10 msec, wave-length 500 nm, band-width 50 nm, telescope diameter 1 m, no central obscuration, r_o of 10 cm, rotation angle 120°, and stellar magnitude of 4 (30.7 photons/pixel) or 8 (0.77 photons/pixel). Two objects were cosidered: a point source and an extended object that was characterised by 18 parameters (Figure 6.4).

6.4 Data reduction.

Once the interferograms are obtained, either experimentally or by simulation, we wish to extract their phases in order to get phase closure. This is done, more or less, in the reverse order. Some of the following steps are after C Roddier and F Roddier [1987a,b], but are all automated.

1. Estimate the number of photons *inside* the interferogram.
2. Subtract this average number to remove the DC bias.
3. Divide by this same intensity to normalise the interferogram.
4. Multiply by the telescope aperture function to remove leftovers outside the measurement area.
5. Estimate the main frequency of interferogram (can be applied to the ensemble):
   5a. Apodise interferogram to remove high frequencies.
   5b. Fourier Transform and square to get power spectrum.
   5c. Locate the highest side lobe and find its size.
6. Turn real interferogram into complex:

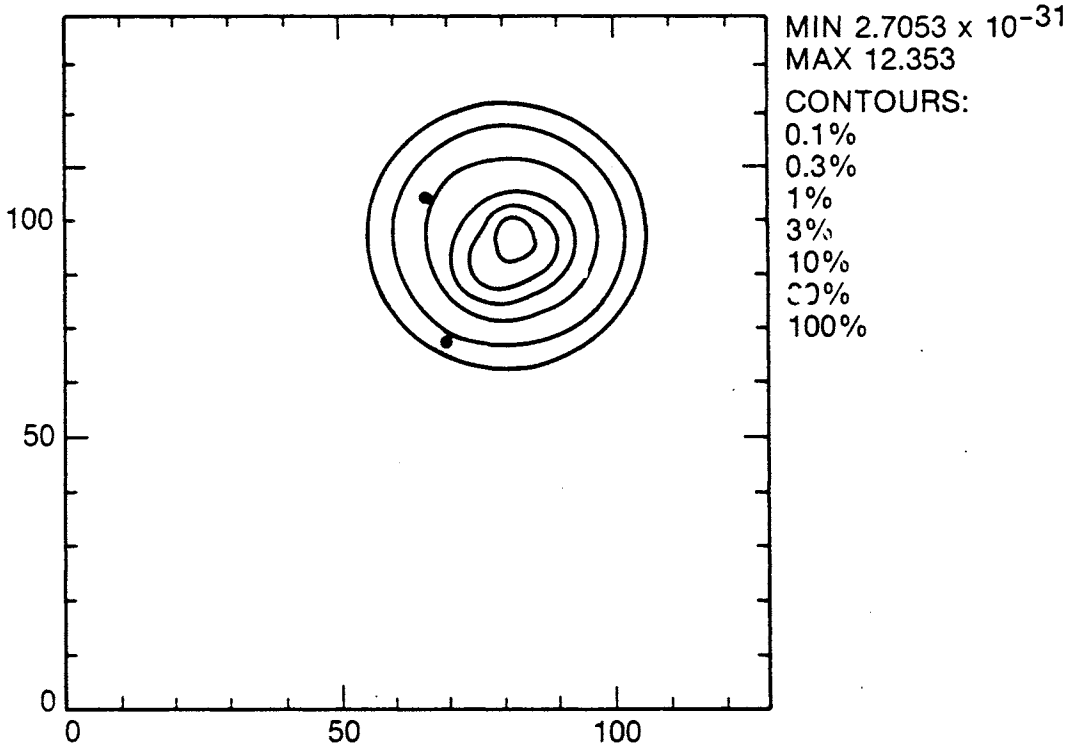

Figure 6.4. An extended object for simulations, composed of a combination of Gaussians and point sources. The object complexity can be inferred from the fact that 18 parameters were used to create it.

6a. Fourier transform frame.
6b. Zero the whole transform except for side lobe indentified in step 5c.
6c. Inverse Fourier transform.
7. Average amplitudes with former frames.
8. Multiply complex frame by its two rotated images (at 120° and 240°) for phase closure.
9. Average closure quantities with former frames.

Note that small errors in the location of the side lobe (corresponding to the interferogram main frequency) are not significant for the purpose of phase closure. They do become important when large, since the nulling of neighbouring points (step 6b) might affect real image points (inside the object support).

For each equilateral triangle we end up with a closure quantity $A_k = a_k \exp i\psi_k$, where k is the frame index. To improve the signal-to-noise ratio we have to average these quantities over many frames. Common sense and experience tell us that the worst way to average the phases is directly, $\psi = \langle\psi_k\rangle$, because of the 2π ambiguities involved. We can average the phasors, $\psi = \arg\{\langle\exp i\psi_k\rangle\}$, but here we add them all up equally, including the ones with the smaller amplitudes (and hence larger errors). Thus an effective way would be to include the amplitudes: $\psi = \arg\{\langle A_k\rangle\} = \arg\{\langle a_k \exp i\psi_k\rangle\}$. This has been shown to be the best combination theoretically [Wuan and Duffett-Smith 1988].

Figures 6.5 – 6.9 show the degradation of the resulting amplitudes and closure phases as a function of object complexity and light level. It is encouraging to see that the closure phases of the involved, eighth magnitude object, are already recognisable after 256 frames (2.56 seconds of observation). In the next step we intend to plug these values in a radio-astronomical image-processing package, such as AIPS, in order to see the level of reconstruction possible. It seems,

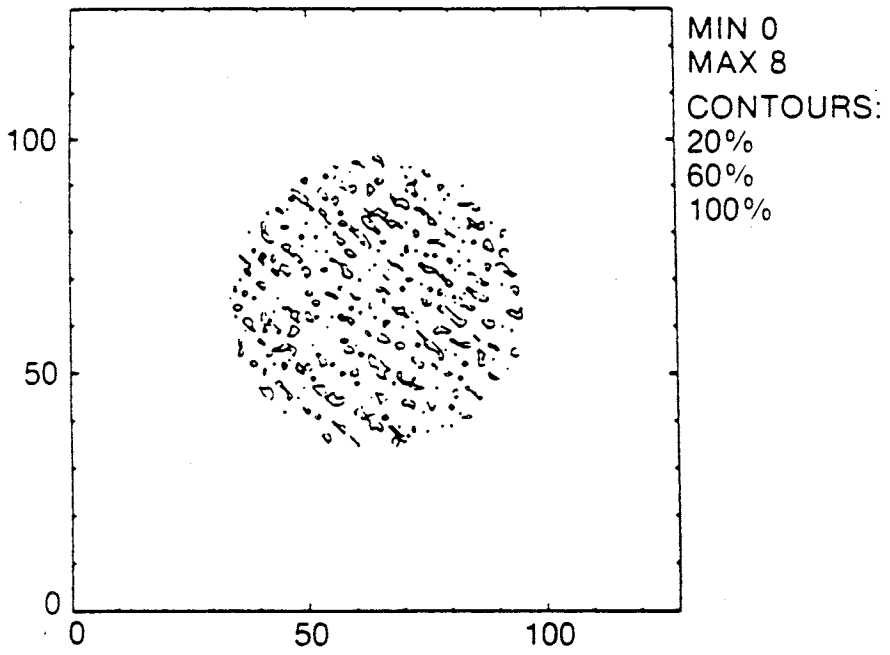

Figure 6.5. A simulated interferogram created by an 8^m point source.

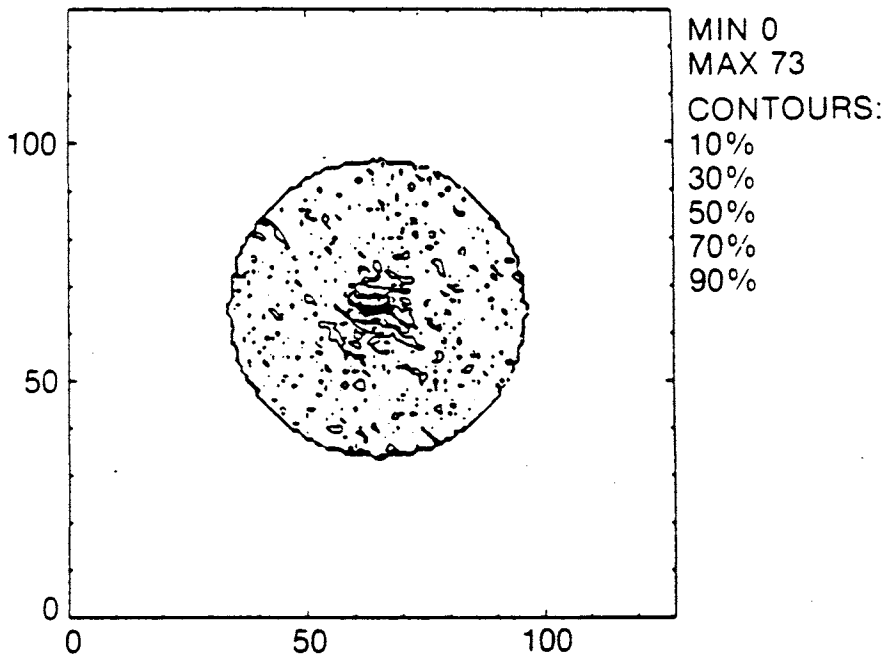

Figure 6.6. A simulated interferogram created by the 4^m extended object.

however, that these packages might not perform as well as a specifically written program which takes into account the unique characteristics of this instrument, such as continuity in the UV plane.

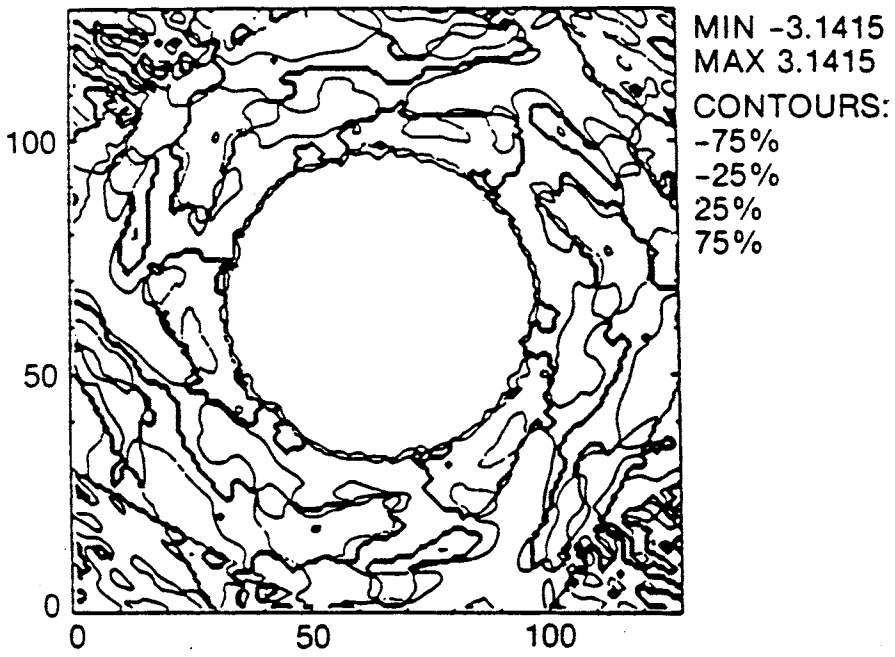

Figure 6.7. Closure phases obtained by averaging 256 frames of an 8^m point source (as in Figure 6.5).

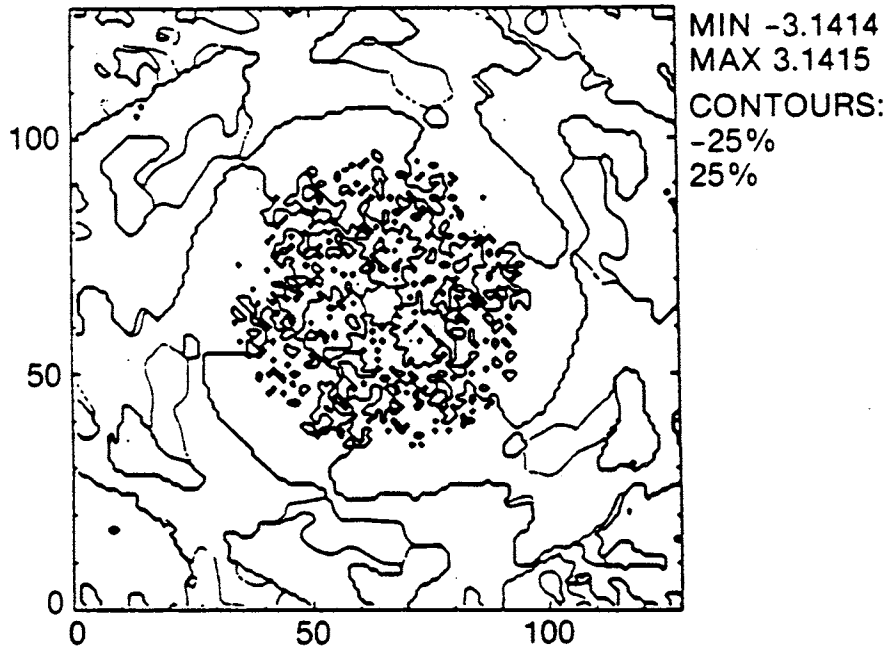

Figure 6.8. Closure phases from 256 frames of the 8^m extended object (40 times fainter than Figure 6.6). Phase noise is high where related amplitudes are less that 5%. Compare with Figure 6.9.

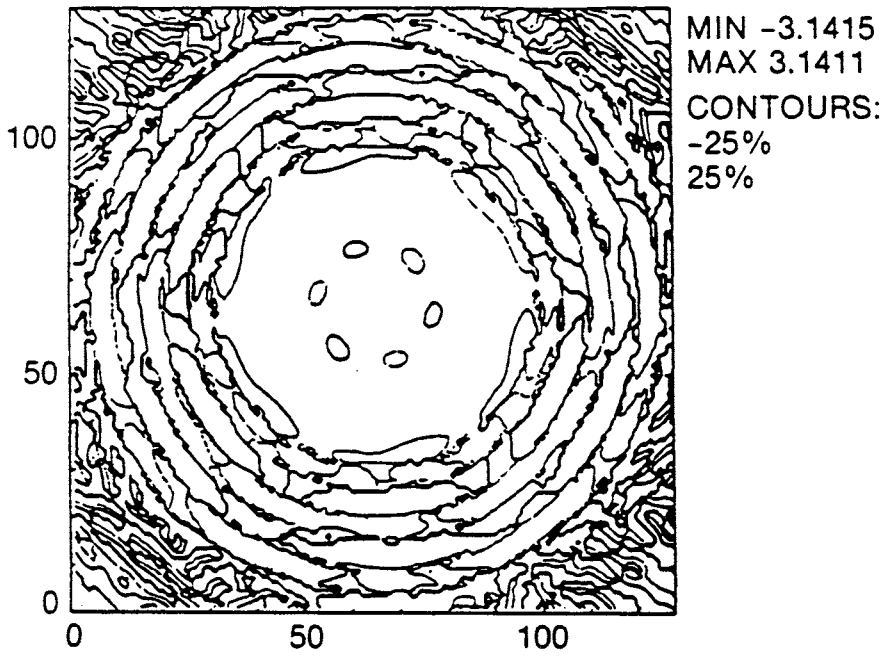

Figure 6.9. Closure phases on the noiseless, turbulence free extended object. All phases inside the telscope are within $[-\pi, \pi]$. Ignore digitisation noise outside telescope.

7. CONCLUSIONS

In this report we tried to show some of the work done on the white light Fourier transform system and its applications. We were able to provide full transforms for complex objects, calculate and prove the signal-to-noise characteristics of the system, discover another use for it, namely phase closure in astronomical imaging, and start some work on using this interferometer as a building block and a part of a full correlator. We feel very strongly that this effort should be further pursued. The most significant points that now need more work are:

1. Building a correlator utilizing a second interferometer for inverse transforms, with the following specific problems to solve:
   a. Efficient coupling of the two parts of the system by optical or electro-optical means.
   b. Application of correlation filters in the Fourier plane.
   c. Miniaturization of the interferometer-chromatic corrector unit.
2. Laboratory and field experiments for phase-closure imaging applications.
3. Development of image reconstruction and signal processing techniques by means of this system (moment calculations, matched filtering).

We believe that the system will find many future applications in white light or narrow band image processing.

8. APPENDIX A: Optical Design Prescription for the White light Rotational Shear Interferometer Brassboard.

Table 8.1 gives the optical prescription for the layout of the white light compensated rotational shear interferometer laboratory set-up shown in Figure 3.1. Column 1 gives the element number, column 2 gives the radius of curvature of the front and the back surface of the element, column 3 gives the thickness of the element, the front and back aperture diameter are given in the fourth column and the fifth column gives the name of the medium or the type of optical glass. All of the glasses were manufactured by Schott. To obtain the necessary "apochromatic" correction four kinds of glasses were used: SF1, BK7, SF8 and LAK31.

The aperture stop of the optical system is located within the rotational shear interferometer. The prisms are given as element number 5 and are Schott BK7 glass modeled here as thick plane parallel plates.

Table 8.2 shows the output sheet from the CODE V optical system ray trace tabular results.

Copies of the drawings used for optical shop specification for the component manufacture are shown in Figure 8.1

Note that the chromatic corrector optical element system designed for this task must be used with the rotational shear interferometer system shown here. The amount of lateral chromatic aberration required to achromatize the fringes depends on the specific layout of the interferometer and power elements.

Figure 8.1. Optical shop specification for the color corrector component manufacture (over).

NOTES :

1. ELEMENT E7 PER DRAWING
   ELEMENT E8 PER DRAWING
   ELEMENT E9 PER DRAWING
2. CEMENT PER MIL-A-3920 USING
3. CENTER WITHIN ARC MINUTES
4. MAX FINISHED DIAMETER SHALL
   NOT EXCEED INCHES.
5. BLACKEN EDGES PER
6. REFERENCE DATA FOR ASS'Y AT NM:
   EFL
   BFL
   FFL

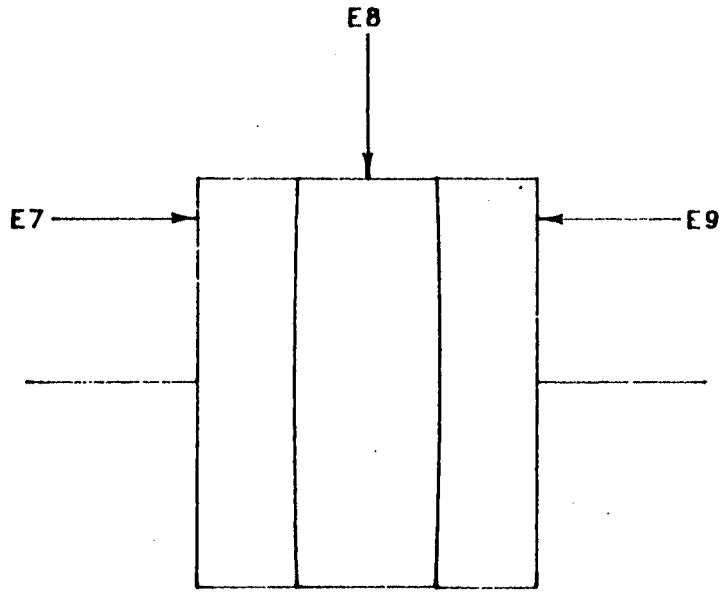

POPI OPTICAL SYSTEM	DR		
	CHK		
	APPD		
ELEMENTS 7 THROUGH 9	SCALE 2.86:1	REL BY	REL DATE

NOTES :

1. ELEMENT E10 PER DRAWING
   ELEMENT E11 PER DRAWING
   ELEMENT E12 PER DRAWING
2. CEMENT PER MIL-A-3920 USING
3. CENTER WITHIN ARC MINUTES
4. MAX FINISHED DIAMETER SHALL NOT EXCEED INCHES.
5. BLACKEN EDGES PER
6. REFERENCE DATA FOR ASS'Y AT NM:
   EFL
   BFL
   FFL

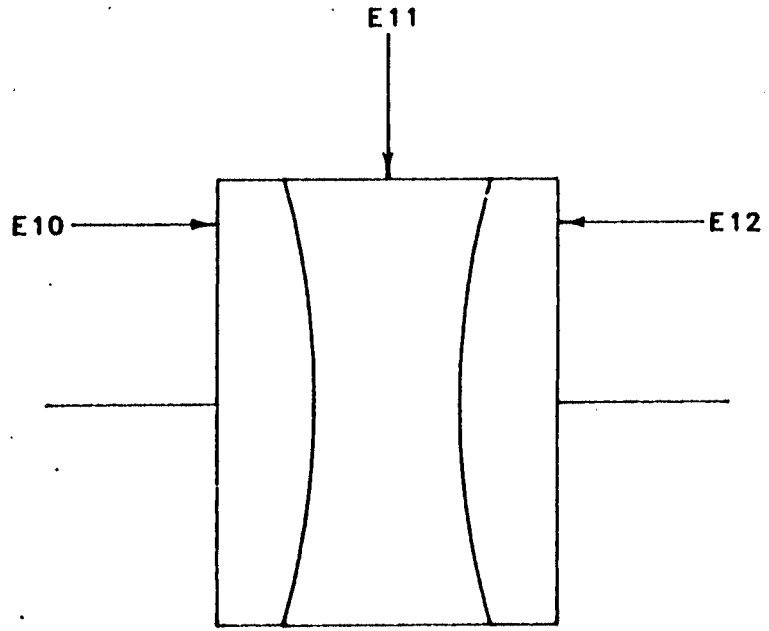

POPI OPTICAL SYSTEM	DR		
	CHK		
	APPD		
	SCALE 2.86:1	REL BY	REL DATE
ELEMENTS 10 THROUGH 12			

NOTES :

1. ELEMENT E13 PER DRAWING
   ELEMENT E14 PER DRAWING
   ELEMENT E15 PER DRAWING
2. CEMENT PER MIL-A-3920 USING
3. CENTER WITHIN ARC MINUTES
4. MAX FINISHED DIAMETER SHALL
   NOT EXCEED INCHES.
5. BLACKEN EDGES PER
6. REFERENCE DATA FOR ASS'Y AT NM:
   EFL
   BFL
   FFL

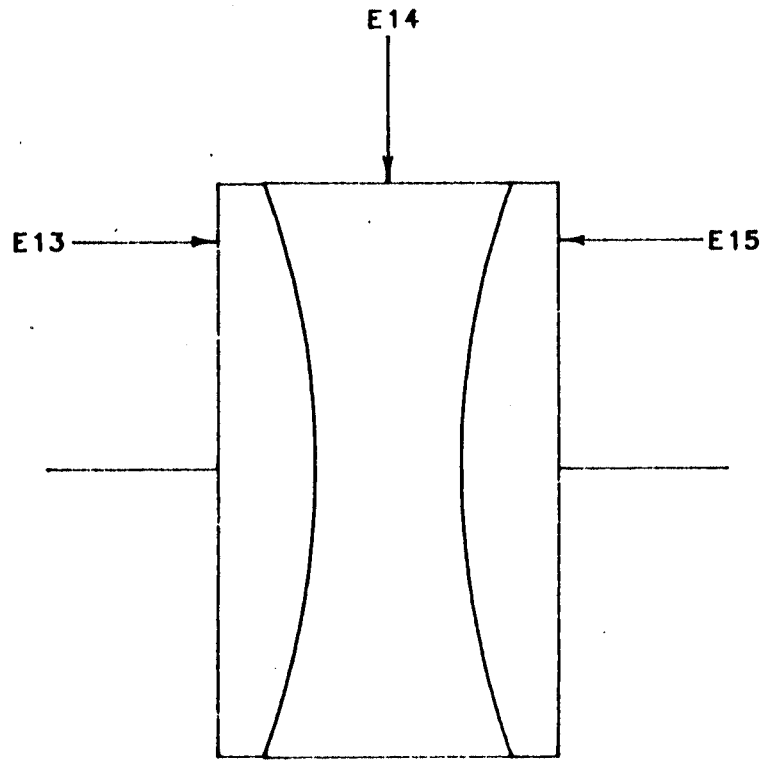

DR	
CHK	
APPD	
SCALE 2.86:1	REL BY / REL DATE

POPI OPTICAL SYSTEM

ELEMENTS 13 THROUGH 15

NOTES :

1. ELEMENT E16 PER DRAWING
   ELEMENT E17 PER DRAWING
   ELEMENT E18 PER DRAWING
2. CEMENT PER MIL-A-3920 USING
3. CENTER WITHIN ARC MINUTES
4. MAX FINISHED DIAMETER SHALL NOT EXCEED INCHES.
5. BLACKEN EDGES PER
6. REFERENCE DATA FOR ASS'Y AT NM:
   EFL
   BFL
   FFL

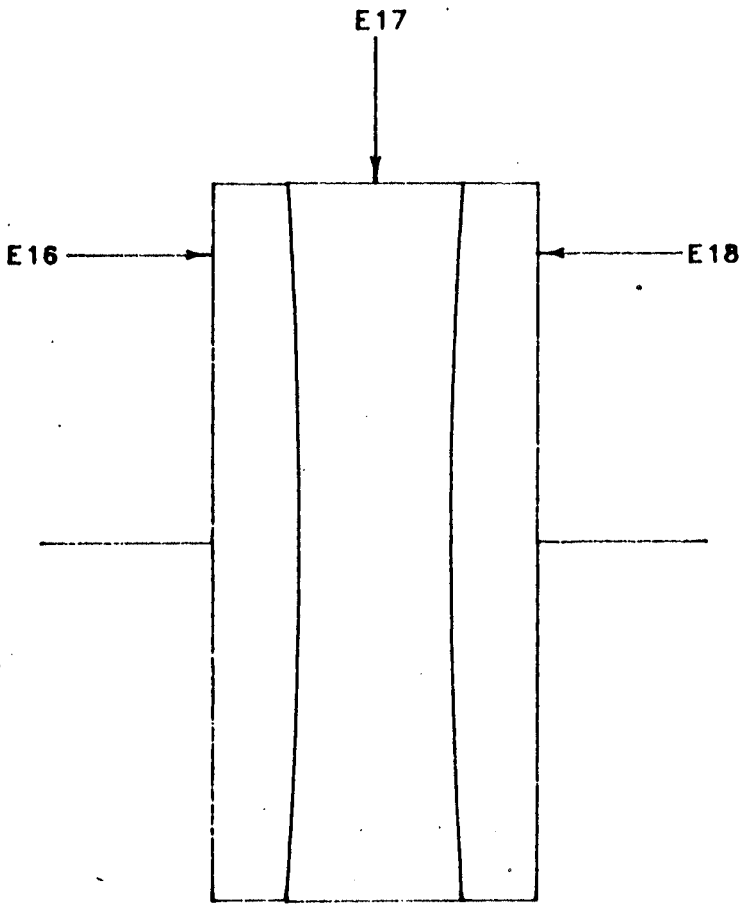

	DR		
	CHK		
	APPD		
POPI OPTICAL SYSTEM	SCALE 2.54:1	REL BY	REL DATE
ELEMENTS 16 THROUGH 18			

Table 8.1. Optical prescription for the layout of the rotational shear interferometer.

POPI OPTICAL PRESCRIPTION

ELEMENT NUMBER	RADIUS OF CURVATURE FRONT	BACK	THICKNESS	APERTURE DIAMETER FRONT	BACK	GLASS
OBJECT	INFINITY		2.0047			AIR
				0.2994		
			4.4673			AIR
1	40.8203 CX	5.1263 CC	0.2500	0.8035	0.8173	SF1 Schott
2	5.1263 CX	-4.7296 CX	0.3000	0.8173	0.8383	BK7 Schott
			0.1137			AIR
3	40.2667 CX	3.5557 CC	0.2500	0.8423	0.8456	BK7 Schott
			0.1137			AIR
4	3.7097 CX	-11.1356 CX	0.2500	0.8621	0.8652	BK7 Schott
			5.3809			AIR
5	INFINITY	INFINITY	2.2000	0.7628	0.7353	BK7 Schott
			APERTURE STOP	0.7353		
	INFINITY	INFINITY	2.2000	0.7353	0.7316	BK7 Schott
			1.5000			AIR
6	INFINITY	12.1109 CC	0.2000	0.7529	0.7546	LAK31 Schott
7	12.1109 CX	-12.1109 CX	0.3000	0.7546	0.7572	SF8 Schott
8	-12.1109 CC	INFINITY	0.2000	0.7572	0.7591	LAK31 Schott
			4.7341			AIR
9	INFINITY	-1.6743 CX	0.2000	0.8334	0.8347	LAK31 Schott
10	-1.6743 CC	1.6743 CC	0.3000	0.8347	0.8371	SF8 Schott
11	1.6743 CX	INFINITY	0.2000	0.8371	0.8374	LAK31 Schott
			7.8083			AIR
12	INFINITY	-1.6743 CX	0.2000	1.0791	1.0800	SF8 Schott
13	-1.6743 CC	1.6743 CC	0.3000	1.0800	1.0840	LAK31 Schott
14	1.6743 CX	INFINITY	0.2000	1.0840	1.0849	SF8 Schott
			32.3440			AIR
15	INFINITY	-12.1109 CX	0.2000	1.5411	1.5426	SF8 Schott
16	-12.1109 CC	12.1109 CC	0.3500	1.5426	1.5459	LAK31 Schott
17	12.1109 CX	INFINITY	0.2000	1.5459	1.5474	SF8 Schott
			2.0000			AIR
				1.5756		
			10.0000			
18	5.2588 CX	10.3787 CC	0.3100	1.7353	1.6998	SF1 Schott
			0.6021			AIR
19	-8.2332 CC	-15.0059 CX	0.3100	1.6442	1.6518	SF1 Schott
			28.1428			AIR
IMAGE	INFINITY			0.6113		

Table 8.2. Output sheet from the CODE V optical system ray trace tabular results.

10-NOV-87
POPI OPTICAL SYSTEM

ELEMENT NUMBER	RADIUS OF CURVATURE FRONT	BACK	THICKNESS	APERTURE DIAMETER FRONT	BACK	GLASS
OBJECT	INF		2.0047*1			AIR
				0.2994		
			4.4673*2			
1	40.8203 CX	5.1263 CC	0.2500	0.8035	0.8173	SF1 Schott
2	5.1263 CX	-4.7296 CX	0.3000	0.8173	0.8383	BK7 Schott
			0.1137			
3	40.2667 CX	3.5557 CC	0.2500	0.8423	0.8456	BK7 Schott
			0.1137			
4	3.7097 CX	-11.1356 CX	0.2500	0.8621	0.8652	BK7 Schott
			5.3809			
5	INF	INF	2.2000	0.7628	0.7353	BK7 Schott
			APERTURE STOP	0.7353		
	INF	INF	2.2000	0.7353	0.7316	BK7 Schott
			1.5000			
6	INF	12.1109 CC	0.2000	0.7529	0.7546	LAK31 Schott
7	12.1109 CX	-12.1109 CX	0.3000	0.7546	0.7572	SF8 Schott
8	-12.1109 CC	INF	0.2000	0.7572	0.7591	LAK31 Schott
			4.7341			
9	INF	-1.6743 CX	0.2000	0.8334	0.8347	LAK31 Schott
10	-1.6743 CC	1.6743 CC	0.3000	0.8347	0.8371	SF8 Schott
11	1.6743 CX	INF	0.2000	0.8371	0.8374	LAK31 Schott
			17.8083			
12	INF	-1.6743 CX	0.2000	1.0791	1.0800	SF8 Schott
13	-1.6743 CC	1.6743 CC	0.3000	1.0800	1.0840	LAK31 Schott
14	1.6743 CX	INF	0.2000	1.0840	1.0849	SF8 Schott
			32.3440			
15	INF	-12.1109 CX	0.2000	1.5411	1.5426	SF8 Schott
16	-12.1109 CC	12.1109 CC	0.3500	1.5426	1.5459	LAK31 Schott
17	12.1109 CX	INF	0.2000	1.5459	1.5474	SF8 Schott
			2.0000			
				1.5756		
			10.0000			
18	5.2588 CX	10.3787 CC	0.3100	1.7353	1.6998	SF1 Schott
			0.6021			
19	-8.2332 CC	-15.0059 CX	0.3100	1.6442	1.6518	SF1 Schott
	IMAGE DISTANCE =		28.1428*3			
IMAGE	INF			0.6113		

NOTES - Positive radius indicates the center of curvature is to the right
Negative radius indicates the center of curvature is to the left
- Dimensions are given in inches

- Thickness is axial distance to next surface

- Image diameter shown above is a paraxial value, it is not a ray traced value

- Other glass suppliers can be used if their materials are functionally equivalent to the extent needed by the design; contact the designer for approval of substitutions.

REFERENCE WAVELENGTH = 480.0 NM

SPECTRAL REGION = 480.0 - 700.0 NM

* ZOOM PARAMETERS		POS. 1	POS. 2	POS. 3	POS. 4	POS. 5	POS. 6	POS. 7
*1	=	2.0047	2.0047	2.0047	47.6254	47.6254	2.0047	2.0047
*2	=	4.4673	4.4673	4.4673	6.8466	6.8466	4.4673	4.4673
*3	=	28.1428	30.2122	30.2122	41.2248	42.9094	29.6614	30.2982

		POS. 1	POS. 2	POS. 3	POS. 4	POS. 5	POS. 6	POS. 7
INFINITE CONJUGATES								
EFL	=	-5.3027	-5.6946	-5.9820	-5.3027	-5.9820	-5.5104	-5.8509
BFL	=	50.4334	59.6797	65.0976	50.4334	65.0976	55.7217	62.7199
FFL	=	-3.2626	-3.1037	-3.0323	-0.8833	-0.6531	-3.1670	-3.0610
F/NO	=	-0.0585	-0.0482	-0.0529	-53.5300	-60.3870	-0.0503	-0.0495
AT USED CONJUGATES								
REDUCTION	=	4.2156	5.1817	5.8212	-0.1134	-0.1274	4.7410	5.5390
FINITE F/NO	=	42.3935	52.1093	58.5397	-54.5416	-61.2266	47.6772	55.7019
OBJECT DIST	=	2.0047	2.0047	2.0047	47.6254	47.6254	2.0047	2.0047
TOTAL TRACK	=	118.1316	120.2011	120.2011	179.2136	180.8983	119.6502	120.2870
IMAGE DIST	=	28.1428	30.2122	30.2122	41.2248	42.9094	29.6614	30.2982
OAL	=	87.9841	87.9841	87.9841	90.3634	90.3634	87.9841	87.9841
PARAXIAL								
IMAGE HT	=	0.2108	0.2591	0.2911	0.2723	0.3056	0.2371	0.2770
IMAGE DIST	=	28.0792	30.1716	30.2753	51.0350	65.8595	29.5966	30.3118
SEMI-FIELD								
ANGLE	=	0.0031	0.0024	0.0025	2.8849	2.8849	0.0026	0.0024
ENTR PUPIL								
DIAMETER	=	90.6048	118.1310	113.1567	0.0991	0.0991	109.6140	118.1951
DISTANCE	=	908.0193	1184.4889	1134.5269	0.0000	0.0000	1098.9451	1185.1326
EXIT PUPIL								
DIAMETER	=	0.5272	0.5665	0.5950	0.5947	0.9074	0.5481	0.5820
DISTANCE	=	50.4026	59.6524	65.0662	18.5996	10.3020	55.6941	62.6911
APER STOP								
DIAMETER	=	0.7102	0.7101	0.7109	0.0991	0.0991	0.7099	0.7105

NOTES - FFL is measured from the first surface
- BFL is measured from the last surface

CODE V>

9. APPENDIX B: Optical Processing Computational Throughput.

The potential computational throughput of a system using parallel optical processing by interferometry is calculated and compared to other methods such as digital and analog image converter methods.

Figure 9.1 shows a schematic diagram of our optical processing system. Plane 2 indicates the entrance pupil of a fore-optic system that relays an image from object space (plane 1) onto a field stop located at the image plane 3. A collimator at plane 4 relays the pupil at plane 2 into an optical interferometer that performs a two-dimensional white light spatial frequency Fourier transform which is displayed at plane 5. The lens at plane 6 relays the output of the interferometer at plane 5 onto the complex (amplitude and phase) filter mask at plane 7. The system forms an image of the processed two-dimensional information at plane 3 as modified by the filter at plane 7 for readout by a two-dimensional array detector system. Here appears the cross-correlation between the scene and the spectrum of the a priori information at the filter.

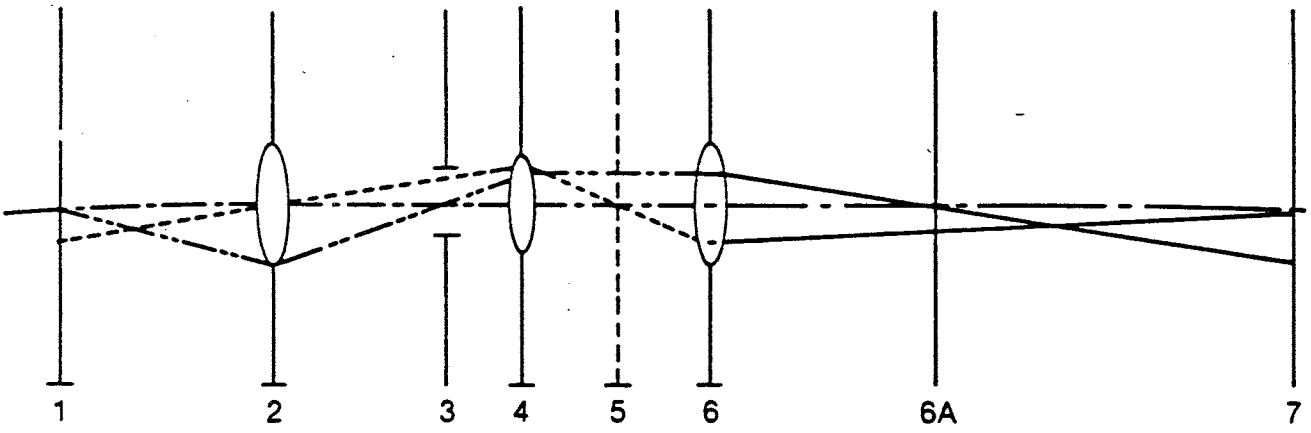

Figure 9.1. Schematic diagram of a white light optical processing system.

Processing

The processing capacity of the optical system between planes 4 and 6 in Figure 9.1 is now calculated. Assume the diffraction limit of the optical system is such that the linear dimension across the zeros of the Airy diffraction pattern is denoted by l, and assume that the field stop at plane 3 in Figure 9.1 has diameter D_3. The number of Airy patterns, A_n, across the portion of

the image plane admitted by the field stop is then

$$A_n = \left(\frac{D_3}{l}\right)^2 \tag{9.1}$$

The Fourier transform operation is performed by the device at plane 5 as a consequence of white light image formation, or the white light interference phenomenon. The Fourier transform of the two-dimensional irradiance distribution across plane 3 is performed in the length of time light takes to travel from plane 3 to plane 7 in Figure 9.1. For a physical distance, L, in meters within the optical system, this time, t, is given by

$$t = m(\frac{L}{3}) \times 10^{-8}\text{seconds} \tag{9.2}$$

To quantify the amount of data, Q, at the image plane 3, we need to assume that each of N independent samples across the image is represented by a quantum of bits, b. The amount of data, Q, at plane 3 is then,

$$Q = Nb \tag{9.3}$$

and the data throughput, T, of the system expressed as data rate (bits per unit time) or band-width is

$$T = Q/t \tag{9.4}$$

A realistic value for T, the throughput, is now computed.

The linear dimension across the Airy diffraction pattern, l, at the image plane 3 is

$$l = 2.441\frac{f_2}{D_2} \tag{9.5}$$

where f_2 is the focal length of the lens at plane 2 in Figure 9.1 whose diameter is D_2. For the system in Figure 9.1 we assume that the lens at plane 4 is large enough to transmit all the rays, with no spatial frequency vignetting onto plane 5.

To identify samples at the image plane 3 that are independent and not correlated at, say, the 1% level, we assume the spacing of the samples, d, must be approximately, $d = 4l$, where l is defined in equation 9.5.

The number, N, of independent samples across the image plane number 3 in Figure 9.1 is then,

$$N = \left(\frac{D_2 D_3}{10\lambda f_2}\right)^2 \tag{9.6}$$

If we assume the quantum number of bits – that is, the number of binary levels used to represent intensity levels within an independent spatial sample at the image plane – to be 10, then, from equation 9.3

$$Q = 10 \times \left(\frac{D_2 D_3}{10\lambda f_2}\right)^2 \tag{9.7}$$

The throughput, T, in units of bits per second is obtained by placing equations 9.7 and 9.2 into equation 9.4, to give,

$$T = \frac{3 \times 10^7}{L}\left(\frac{D_2 D_3}{\lambda f_2}\right)^2 \tag{9.8}$$

where the variables are in units of meters.

If we assume that the entrance aperture diameter of the optical system, D_2, is 0.1 m, that the diameter at the field stop, D_3, is 0.1 m, that the focal length, f_2, is 1.0 m, that the length of the entire optical system, L, is 3.0 m, and that the wave-length, λ, is 500 nm, then the processing throughput of the system, T, is found to be

$$T = 4 \times 10^{15} \text{bits per second}$$

or 4 peta (peta $= 10^{15}$) bits per second.

This data processing rate represents an approximate upper bound theoretical limit for real-time parallel optical processing by interferometry. This rate is several orders of magnitude above current predictions for the more classical digital architectures. If this capacity is realizable in a system, a new dimension in information processing is opened up. The throughput in equation 9.8 is per unit of the broad band wave-length interval of the "white light" signal. Wave-length multiplexing may be possible to increase the system information throughput beyond that given above by up to a factor of 100.

10. APPENDIX C: CCD Camera Details.

Details given by Photometrics Ltd., 2010 N. Forbes Blvd, Suite 103, Tucson, Arizona 85745.

GENERAL DESCRIPTION

The Photometrics, Ltd. Model 81S-A CCD Camera System consists of a Model 80-A Camera Controller, a Model CH81-A Camera Head, a Model 810 Cooler Power Unit and associated interconnecting cables. The Model 80-A Controller has connectors on the rear panel which allow on-line camera control from a user processor and provides digital intensity and X, Y pixel position data. Also, three analog outputs are provided which may be used to drive an XYZ CRT monitor.

The RCA SID53612X0 CCD is divided into two sections; a 320x256 element image array and a 320x256 element storage array. Both arrays may function as imagers in a 320x512 element mode. Figure I-1 illustrates the device architecture. The Model 80-A Controller provides the options of transferring the image array to the storage array, reading out the storage array while the image array is integrating and reading the image and storage arrays as a single field; the latter option being the most commonly used. A set of parameters (ΔX, ΔY) may be passed to the camera so that only a subarray, called a field, on the CCD is read out which may be any size rectangle up to the size of the entire array, i. e. 320x512 elements.

Also, the origin or location of the field may be specified by the two parameters ($X\phi$, $Y\phi$). The CCD is unique in that during the readout, charge from adjacent rows may be combined in the horizontal storage register as vertical shifting proceeds. As charge is shifted out of the horizontal register, individual pixels may be combined so that the final charge packet which is read out is the combined charge from several pixels in a rectangle called a superpixel. The result of combining pixels (binning) is that the output signal will have an increased level since it has the contribution of several pixels while system noise remains constant.

Figure I-1 illustrates how a 100x200 field located at origin X=110, Y-156, binned into a 1x1 pixel would look as seen on the CCD. Other binning formats may be used, for example, 2x4 pixels. Resolution is reduced, however, since each superpixel consists of 8 individual pixels. There is a limit to how many pixels may be binned, since the horizontal register will saturate at some point, and the output diffusion where individual pixels are combined will also saturate. The number of pixels which may be binned depends upon the total integrated charge within the superpixel, which, in turn, is scene-related. Care must be taken to see that saturation does not occur when operating in a binning mode.

The low speed analog processor card located in the Camera Head uses a correlated double sample integration to remove KTC offset caused by the CCD reset switch. The integrator gain may be set by the user so that in binning applications, a low gain will allow full dynamic range to be realized. For non-binned readout, a higher gain is required since each pixel output will contain only a single equivalent unit of charge.

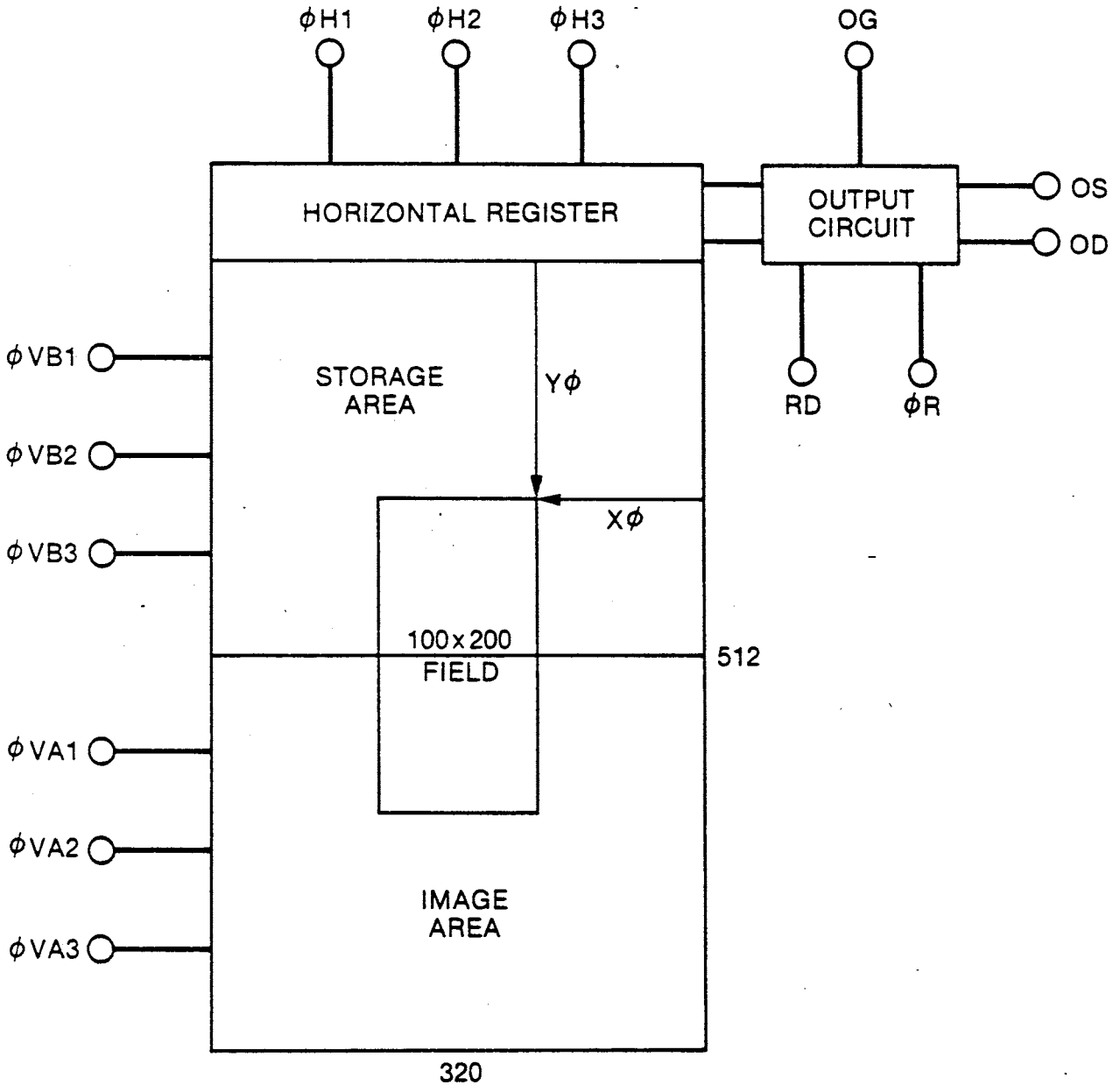
φH1
φH2
φH3
OG
HORIZONTAL REGISTER
OUTPUT CIRCUIT
OS
OD
φVB1
φVB2
φVB3
STORAGE AREA
Yφ
RD
φR
Xφ
100x200 FIELD
512
φVA1
φVA2
φVA3
IMAGE AREA
320

The high speed analog processor (optional) allows readout rates to 5 μseconds/pixel, but is not programmable in gain. A two-pole lowpass filter is used instead of the integrator and the correlated double sample is made on the filtered signal.

The Model CH81-A Camera Head contains a vacuum chamber with a 3-stage thermoelectric cooler. The CCD is mounted to the cooler and the preamplifier electronics are located in the vacuum chamber. A 26-pin hermetic connector is used to interface the vacuum chamber electronics with the electronics which reside in a 5-card cage. A small fan provides cooling for the electronics and the hot side of the thermoelectric cooler.

A lens and shutter assembly are provided for typical shuttered mode operation, however, these may be removed for direct image plane work or other special applications.

MODEL 80-A UNIVERSAL CAMERA CONTROLLER SPECIFICATIONS

DIGITAL INTERFACE

All digital outputs are buffered TTL Active Low Sense. All inputs are TTL, pulled up with 1K resistors to +5 volts.

INPUTS

$\overline{\text{CONTROL}}$-12 lines. 8 bits of parameter input and 4 bits of command.

$\overline{\text{STROBE}}$-Strobes the command and specified parameters, if any, into the Model 80-A Controller. All 12 inputs must be stable when $\overline{\text{STROBE}}$ is asserted with a minimum width of 1 μsec.

OUTPUTS

$\overline{\text{RDY}}$-Low when Camera Controller is ready for a new command. Goes high when $\overline{\text{STROBE}}$ is asserted and remains high until Controller is ready again for new input.

$\overline{\text{TIP}}$-Low when Camera Controller is busy executing a task.

$\overline{\text{DATA}}$-Up to 15 data lines, depending on specific Camera Head used. It represents the intensity of the pixel specified by X and Y addresses and is output in straight binary code.

$\overline{\text{DVD}}$-Low Data Valid pulse 330 ns. wide, may be used to strobe Z axis digital data into a register.

$\overline{\text{ADDRESS}}$-X and Y address of pixel being read out. Up to 10 bits in each axis depending on array type.

$\overline{\text{AVD}}$-Low address valid pulse 330 ns. wide, may be used to strobe X and Y digital addresses into a register.

ANALOG INTERFACE

All analog outputs appear on isolated ground BNC connectors with an impedance of 1K. X and Y analog outputs are voltages reflecting the position of the pixel being read out and are 5 mv. per pixel address. Z axis analog output is reconstructed from digital data to produce voltage proportional to intensity with a range of Ø to 2.5 volts. The analog outputs are intended to drive an XYZ monitor such as a Tektronix, Model 604A. This is especially useful for setup and focusing the camera.

GENERAL SPECIFICATIONS

POWER - 105-125 Volts, 50-440 Hz. AC. 90 watts.

MECHANICAL - Standard 19-inch (43.3 cm.) wide rack-mountable; 5¼ inch high (13.3 cm.) x 18-inch (45.7 cm.) enclosure.

WEIGHT - 20 lbs.; 9.1 kgs.

VIII. Hardware:

The DIPS 184 consists of a Photometrics digital electronic camera and a computer. The camera and controller are described in other documentation. This manual describes the computer system and the software which supports user interaction with the camera.

The computer system is based upon Multibus™ architecture and consists of a single board computer, ram memory board(s), a scan converter image display, a DMA camera controller interface, a Winchester disk, a floppy disk and an optional 1/4" cartridge tape unit or a 9-track tape unit for removable archive storage. A graphics terminal is supported by the system but is not essential. The peripheral hardware supported is:

a) the Multibus™ memory,
b) a 1/4" cartridge tape (optional),
c) a 65 megabyte disk,
d) a scan converter,
e) the ccd camera system,
f) a graphics terminal (optional),
g) a 9-track tape (optional),
h) a floppy disk drive (8" or 5 1/4").

A. The Computer:

The computer is supplied by the Heurikon Corp. of Madison Wisconsin. The basic system consists of a single board processor in a six or 14 slot rack-mounted enclosure. The single board computer contains four serial ports, the Winchester and floppy disk controllers and 1-Mbyte of RAM memory. This RAM memory is termed "on-board" as opposed to other memory on the Multibus™. A portable 6-slot version of the computer system is available

that utilizes a 5 1/4" floppy disk drive.

B. The Winchester Disk:

The 5 1/4" form factor Winchester disk has 65 Mbytes of un-formatted capacity. A 140 Mbyte unit is optionally available. Additional disk units of the same capacity can be added to the system in an expansion chassis.

C. The Floppy Disk:

The eight-inch floppy is a standard 48 tpi, double sided double density unit having capacity for 1.3 Mbytes. The 5 1/4" unit is a 96 tpi quad density unit that holds 0.75 Mbytes.

D. Memory:

The program employs Multibus™ RAM for image buffers. The camera performs DMA transfer directly from the digitizer into the Multibus™ memory starting at a program-supplied address and continuing until the specified count of pixels has been transferred. The program requires sufficient RAM to hold one full-size image. To utilize the interactive image processing activities, RAM sufficient to hold three images is required. RAM boards are available in 1, 2 or 4 Mbyte sizes. Clearly the number of images that can be accommodated at one time is dependent upon their sizes as well as the RAM memory available. RAM memory on the Multibus can be configured by the user. RAM to be used by the UNIX OS is specified by setting the RAM module hardware address registers to fill the memory space extending from the end of on-board RAM to the 2-Mbyte OS upper limit. RAM to be used

exclusively by external programs such as the CCD program is obtained by setting the address offsets to be equal to or greater than 2 Mbytes. The UNIX OS is restricted to only using available RAM below the 2 Mbyte boundary. RAM boards can be used which span the 2 Mbyte boundary if desired. Adding UNIX RAM allows larger concurrent user programs. It is even possible to allow two versions of the ccd program to run concurrently by creating two different executable binary images with different Multibus RAM image buffer pointers. The memory is byte addressed. Image array elements are 2-byte quantities.

E. Image Display:

The image display is a two-plane scan converter having an image plane that is 640 x 480 pixels x 8-bits and a graphics overlay plane that is 640 x 480 pixels x 1-bit. The image display has no input or output windowing. The program is able to directly load the unit from RAM so reasonably rapid updating is possible. In addition, the program provides a small-area special windowing function (sw) for rapid user interaction. The graphics overlay is rendered at 2x the beam intensity of the full scale image plane. The two signals are merged in the RS170 video output. It is necessary to adjust the display monitor brightness and contrast so that graphics do not "bloom".

F. The DMA Controller Interface:

This Multibus™ board contains the registers required to perform DMA transmission of data from the camera into the

Multibus™ RAM. It is also capable of transmitting commands to the camera controller in a manner which allows duplication of command sequences that are available at the front of the stand alone camera controller chassis. The camera controller must be "on-line" for the computer to communicate with it. The computer is able to interrogate the on-line, the ready and the "TIP" signals and properly synchronize command and data transfer sequences.

G. The 1/4" Archive Tape:

The 1/4" tape is a special device that uses pre-formatted cartridges. The device looks like a disk in that it is random access with the ability to write over sector-sized segments anywhere on the tape.

The tape unit employs special cartridges that have pre-recorded format and should never be "bulk" erased as the format will be lost. The 1/4" cartridge tape comes in two lengths but the program only deals with the 600' cartridges which contain 65536 1024-byte blocks.

The cartridge locks into the drive after it is loaded. It can be disengaged by the user command unload. The tape cartridge should be removed from the drive when it is powered down. The tape drive emits a very striking "buzz" when the cartridge is released. When this sound occurs, a cartridge can be removed if one was in the drive. This release occurs at power up and when the user unload command is executed. The tape scans its entire length

upon first loading, an activity that calibrates the position of the tape but which also takes about three minutes to complete for a 600' cartridge.

H. The Camera Controller:

The Photometrics Camera controller employs a microprocessor which accepts commands and their (occasionally optional) data qualifiers. The definition of the hardware camera commands is contained in the Photometrics Camera hardware manual. The camera controller is connected to the DMA controller interface through a programmed I/O hardware driver. The program provides a command for controlling the camera: camcmd, (camcmd <com> <data>), which allows the user to command all of the camera functions from the computer. It also provides several program sequences (such as obs and dark) that allow the specification of the camera readout parameters, the camera exposure conditions and, for timing sequences which are outside the 12.567-second range of the hardware shutter, exposure timing.

For timing exposures, the computer uses the system clock which has a resolution of one second. The camera controller contains a clock which has a resolution of 50 milliseconds. The controller and the computer cannot perform identical timing operations in the short-duration area. The higher resolution of the controller is utilized for timing obs exposure activities that are ten seconds or shorter. Since there is no hardware capability to sequence a dark exposure, the computer times darks

using the system clock.

In the Photometrics Camera System hardware documentation, an image is described in a X x Y format where X is the number pixels in an image row. An image is read from the camera one row at a time so the most rapidly varying subscript is the element within the row. In the Photometrics DIPS 184 Software system, the term column is used to describe a reference in the X direction, row is used for the Y direction.

IX. Program Description

The Photometrics ccd program controls all of the hardware in the DIPS 184 system including the ccd camera and the computer. It is operated by running a program, called ccd, that provides user control of the camera and computer hardware and the data that is obtained with it.

The program is coded in the "C" programming language and is designed to run under a UNIX operating system. It can be run single user or while running UNIX as a multi-user system. Since there is only one image display and camera, and since the ccd program utilizes a large memory extent, a multi-user environment can only support other terminals which are executing programs that do not require large memory extents. The primary virtue of running multi-user is that the updating of the disk image of the master file system block (sync) occurs regularly without user intervention. This is an important virtue in the event of a system crash.

A. Utilization of Resources.

Unix uses approximately 250 Kbytes of on-board memory, the program uses in excess of 200 Kbytes of on-board memory when it is running. The auxiliary Multibus™ RAM extent is utilized as a ccd program resource (it is physically withheld from the operating system and mapped into user space) to hold images. This RAM extent is referred to as the "image cache."

The system is supplied with a 65 Mbyte (unformatted capacity) Winchester disk. In a UNIX system which has been stripped of the directory called dict and its file of words, the games directory and the man directory, there is user disk space sufficient to hold about 90 320x512-pixel "images." The program utilizes the disk within the UNIX file system so each image is a file.

Any of the standard operating system file manipulations can be addressed to image files. In particular, saving and restoring of images can be exercised using the tar or dd facilities as described in the UNIX manual.

It should be noted that the organization of bytes in a 68000 computer is such that data which is read from a magnetic tape written on any non-DEC equipment will have bytes swapped for 16-bit binary images. The user can invoke a tape device (see the Heurikon UXIX Users Manual for byte swapping tape devices) which swaps bytes automatically. This has some problems since character information does not want to be swapped, only data.

11. APPENDIX D: REFERENCES

J D Armitage and A W Lohmann [1965]: "Character recognition by incoherent spatial filtering," Applied Optics 4, 461-467.

R H T Bates and M J McDonnel [1986]: *Image restoration and reconstruction,* Clarendon Press, Oxford.

T E Bell [1986]: "Optical computing: a field in flux," IEEE Spectrum **23**, 34-57.

D J Bone, H-A Bachor and R J Sanderman [1986]: "Fringe-pattern analysis using 2-D Fourier transform," Applied Optics **25**, 1653-1660.

J B Breckinridge [1972]: "Coherence Interferometer and Astronomical Applications," Applied Optics **11**, 2996.

J B Breckinridge [1974]: "Two-dimensional white light coherence interferometer," Applied Optics **13**, 2760-2762.

J B Breckinridge [1976]: *The spatial structure analyser and its astronomical applications,* Ph.D. Thesis, University of Arizona.

J B Breckinridge [1978]: "A white light amplitude interferometer with 180-degrees shear," Optical Engineering **17**, 156.

J M Burch [1953]: "Scatter fringes of equal thickness," Nature **171**, 889-890.

W T Cathey [1974]: *Optical information processing and holography,* Wiley, New York.

G Cochran [1966]: "New method of making Fresnel transforms," Journal of the Optical Society of America **56**, 1513.

P Connes [1970]: "Astronomical Fourier Spectroscopy," *Annual Review of Astronomy and Astrophysics* **8**, 209.

D Courjon and J Bulabois [1979]: "Real time holographic microscopy using a peculiar holographic illuminating system and a rotary shearing interferometer," Journal of Optics (Paris) **10**, 125-128.

D L Fried [1977]: "Least-square fitting a wave-front distorsion estimate to an array of phase-difference measurements," Journal of the Optical Society of America **67**, 370-375.

N George, S Wang [1984]: "Cosinusoidal transforms in white light," Applied Optics **23**, 787-797.

R W Gershberg [1974]: "Super-resolution through error energy reduction," Optica Acta **21**, 709-720.

D C Ghiglia, G A Mastin and L A Romero [1986]: "A cellular automata method for phase unwrapping," OSA Topical Meeting on *Signal Recovery and Synthesis II*, held in Honolulu, Technical Digest FC2.

I Glaser [1987]: "Information processing with spatially incoherent light," *Progress in Optics* XXIV, 390-509, editor E Wolf, North-Holland.

J W Goodman [1968]: "Introduction to Fourier optics," McGraw-Hill, New York.

K-H Hofmann and G Weigelt [1986]: "High angular resolution shearing spectroscopy and triple shearing interferometry" Applied Optics **25**, 4280-4287.

K-H Hofmann and G Weigelt [1987]: "Triple shearing interferometry and shearing spectroscopy," in the Proceedings of the ESO/NOAO Workshop, 83-84, *High angular resolution imaging from the ground using interferometric techniques*, editor J Goad (Oracle, Arizona, 1987).

J Högbom [1974]: "Aperture synthesis with a non-regular distribution of interferometer baselines," Astrophysical Journal Supplement **15**, 417.

R H Hudgin [1977]: "Wave-front reconstruction for compensated imaging," Journal of the Optical Society of America **67**, 375-378.

B R Hunt [1979]: "Matrix formulation of the reconstruction of phase values from phase differences," Journal of the Optical Society of America **69**, 393-399.

K Itoh [1982]: "Analysis of the phase unwrapping algorithm," Applied Optics **21**, 2470.

K Itoh and Y Ohtsuka [1983]: "Phase estimation based on the maximum likelihood criterion," Applied Optics **22**, 3054-3057.

K Itoh and Y Ohtsuka [1983]: "Interferometric imaging of a thermally luminous two dimensional object," Optics Communications **48**, 75-79.

K T Knox and B J Thompson [1974]: "Recovery of images from atmospherically degraded short exposure photographs," Astrophysical Journal letters **193**, L45.

K V Konjaev [1967]: "Interfereence method of two-dimensional Fourier transform with spatially incoherent illumination," Physics Letters **24A**, 490-491.

A Kozma and N Massey [1969]: "Bias level reduction of incoherent holograms," Applied Optics **8**, 393.

E N Leith and D K Angell [1985]: "Generalization of some incoherent spatial filtering

techniques," Applied Optics **25**, 499.

A Lohmann [1965]: "Wave-front reconstruction for incoherent objects," Journal of the Optical Society of America **55**, 1556.

S Lowenthal, J Serres, and H Arsenault [1970]: "Resolution and film-grain noise in Fourier Transform Holograms Recorded with Coherent or Spatially Incoherent Light," Optics Communications **1**, 438.

W W Macy [1983]: "Two-dimensional fringe-pattern analysis," Applied Optics **22**, 3898-3901.

A Marathay [1987]: "Non-coherent-object hologram: its reconstruction and optical processing," Journal of the Optical Society of America **A 4**, 1861-1868

B L McGlamery [1971]: "Image Restoration Techniques Applied to Astronomical Photography," NASA Technical Report SP-256.

L N Mertz [1965]: *Transformations in optics,* Wiley, New York.

L N Mertz [1984]: "Phase estimation with few photons," Applied Optics **23**, 1638-1641.

L N Mertz [1985]: "Multichannel seeing compensation via software," Applied Optics **24**, 2898-2902.

M V R K Murty and E C Hagerott [1966]: "Rotational-Shearing Interferometry," Applied Optics **5**, 615-619.

K A Nugent [1985]: "Interferogram analysis using an accurate fully automatic algorithm," Applied Optics **24**, 3101-3105.

A Papoulis [1965]: *Probability, Random Variables and Stochastic Processes,* (McGraw-Hill).

W T Rhodes and A A Sawchuk [1981]: "Incoherent image processing," in *Optical information processing,* editor S H Lee, Springer-Verlag, Berlin.

E Ribak and E Leibowitz [1985]: "Shearing Stellar Interferometer: 1. Digital data analysis scheme," Applied Optics **24**, 3088.

E Ribak, E Leibowitz, and E K Hege [1985]: "Shearing Stellar Interferometer: 2. Optoelectronic phase locked system," Applied Optics **24**, 3094.

Ribak, E [1987a]: "Phase relations in a rotational shear interferogram," in the Proceedings of the ESO/NOAO Workshop, 215-218, *High angular resolution imaging from the ground using interferometric techniques*, editor J Goad (Oracle, Arizona, 1987).

E Ribak [1987b]: "Phase closure with a rotational shear interferometer," Applied Optics **26**, 197-199.

E Ribak, C Roddier, F Roddier, and J B Breckinridge [1987]: "Signal to noise ratio in white light holography," Applied Optics **27**, 1183-1186.

Ribak, E [1988]: "Phase relations and imaging in pupil plane interferometry," in the Proceedings of the NOAO/ESO conference *High resolution imaging by interferometry* (Garching bei Munchen, 15-18 March 1988)

C Roddier [1976]: "Measurements of the atmospheric attenuation of the spectral components of astronomical images," Journal of the Optical Society of America **66**, 478-482.

C Roddier and J Vernin [1977]: "Relative contribution of upper and lower atmosphere to integrated refractive-index profiles," Applied Optics **16**, 2252-2256.

C Roddier, [1979]: "Enregistrement holographiques d'images astronomiques degradees par la turbulence atmospherique," ATP Traitement des Images du CNRS, Contrat no. 3109, final report.

C Roddier and F Roddier [1979]: "Imaging with a coherence interferometer in optical astronomy" in the Proceedings of IAU colloquium number 49 on *Formation of images from spatial coherence functions in astronomy*, held in Groningen (1978), editor C van Schooneveld, Reidel.

C Roddier, F Roddier, F Martin, A Baranne, and R Brun [1980]: "Twin-image holography with spectrally broad light," Journal of Optics (Paris) **11**, 149.

C Roddier and F Roddier [1983]: "High angular resolution observations of Alpha Orionis with a rotation shearing interferometer," Astrophysical Journal **270**, L23-L26.

C Roddier and F Roddier [1987a]: "Processing of interferograms," in the Proceedings of the ESO/NOAO Workshop, 25-28, *High angular resolution imaging from the ground using interferometric techniques*, editor J Goad (Oracle, Arizona, 1987).

C Roddier and F Roddier [1987b]: "Interferogram analysis using Fourier transform techniques," Applied Optics **26**, 1668-1673.

F Roddier [1979]: "Rotation shearing interferometry" in the Proceedings of IAU colloquium number 50 on *High angular resolution stellar interferometry*, held at the University of Maryland (1978), editors J Davis and W J Tango, Chatterton Astronomy Department, University of Sydney.

F Roddier [1981]: "The effects of atmospheric turbulence in optical astronomy," *Progress in Optics* XIX, 281-376, editor E Wolf, North-Holland.

F Roddier and C Roddier [1977]: "Imaging with a multi-mirror telescope" in the Proceedings of ESO conference on *Optical Telescopes of the Future*, held in Geneva (1977), editors F Pacini,

W Richter, and R N Wilson, Geneva 23: ESO c/o CERN.

F Roddier, C Roddier, J Demarcq [1978]: "A rotation shearing interferometer with phase-compensated roof prisms," Journal of Optics (Paris) **9**, 145.

F Roddier and C Roddier [1985]: "An image reconstruction of Alpha Orionis," Astrophysical Journal **295**, L21-L23.

F Roddier and C Roddier [1986]: "Phase closure with rotational shear interferometers," Optics Communications **60**, 350-352.

F Roddier and C Roddier [1987]: "Phase closure with rotational shear interferometers," in the Proceedings of the ESO/NOAO Workshop, 79-82, *High angular resolution imaging from the ground using interferometric techniques*, editor J Goad (Oracle, Arizona, 1987).

R M Scott [1969]: "Scatter Plate Interferometry," Applied Optics **8**, 531-537.

G W Stroke and R C Restrick [1965]: "Holography with spatially incoherent light," Applied Physics Letters **7**, 229.

G W Stroke [1969]: *An introduction to coherent optics and holography,* 2nd Edition, Academic Press.

M Takeda, I Hideki and S Kobayashi [1982]: "Fourier-transform method of fringe-pattern analysis for computer-based topography and interferometry," Journal of the Optical Society of America **72**, 156-160.

J M Tribolet [1979]: "A new phase unwrapping algorithm," IEEE Transactions on Acoustics, Speech, and Signal Processing **ASSP-25**, 170-177.

S Wang and N George [1985]: "Fresnel zone transforms in spatially incoherent illumination," Applied Optics **24**, 842-850.

G Wuan and P J Duffett-Smith (1988): "Determination of closure phase in noisy conditions," submitted to Astronomy and Astrophysics.

12. APPENDIX E: REPORTS

The following peer-reviewed papers are attached:

E Ribak, C Roddier, F Roddier, and J B Breckinridge [1987]: "Signal to noise ratio in white light holography." Applied Optics **27**, 1183-1186.

C Roddier and F Roddier [1987]: "Interferogram analysis using Fourier transform techniques", Applied Optics **26**, 1668-1673.

E Ribak [1987]: "Phase closure with a rotational shear interferometer." Applied Optics **26**, 197-199.

Signal-to-noise limitations in white light holography

Erez Ribak, Claude Roddier, Francois Roddier,
and James B. Breckinridge

a reprint from Applied Optics
volume 27 number 5, March 15, 1988

Signal-to-noise limitations in white light holography

Erez Ribak, Claude Roddier, Francois Roddier, and James B. Breckinridge

A simple derivation is given for the signal-to-noise ratio (SNR) in images reconstructed from incoherent holograms. Dependence is shown to be on the hologram SNR, object complexity, and the number of pixels in the detector. Reconstruction of involved objects becomes possible with high dynamic range detectors such as charge-coupled devices. We have produced such white light holograms by means of a rotational shear interferometer combined with a chromatic corrector. A digital inverse transform recreated the object.

I. Introduction

Incoherent optical Fourier transforms have an advantage over coherent transforms in that they can be performed on natural white-light scenes as well as on simple input devices [cathode ray tubes (CRTs), image intensifiers]. They are also less sensitive to coherent noise and to system vibrations. In this paper we investigate the noise characteristics of such transforms.

An incoherent optical Fourier transform is obtained when each point of an incoherent object produces a distinct sinusoidal fringe pattern. The incoherent addition of all the fringe patterns produces the object Fourier transform. This is the case when an interferometer gives two images of an incoherent object, one being rotated with respect to the other.[1-14] Let $o(\mathbf{x})$ be the irradiance distribution in the incoherent object. Without loss of generality we shall assume that the object is at infinity so that $\mathbf{x}$ is a pair of angular coordinates expressed in radians. The irradiance distribution $I(\mathbf{u})$ in the hologram can be written in a general way:

$$I(\mathbf{u}) = O(0) + \mathrm{Re}O(kR\mathbf{u}/\lambda), \tag{1}$$

where $O(\cdot)$ is the Fourier transform of $o(\cdot)$, k is a magnification factor, R is a rotation operator, and λ is the wavelength. The Fourier transform $i(\cdot)$ of the irradiance distribution in the hologram gives

$$(k/\lambda)^2 i(kR^{-1}\mathbf{x}/\lambda) = O(0)\delta(\mathbf{x}) + \tfrac{1}{2}[o(\mathbf{x}) + 0(-\mathbf{x})], \tag{2}$$

where R^{-1} is the inverse rotation and $\delta(\mathbf{x})$ is a Dirac distribution. Equation (2) shows that the object can be recovered from the hologram as long as it does not overlap with its mirror image with respect to the interferometer axis. Another limitation is that the transform has to be either narrowband or chromatically corrected to utilize the polychromatic nature of real-life objects [and increase the signal-to-noise ratio (SNR) of the transform]. Many efforts have been conducted[15-18] toward a solution to this limitation. For involved objects, the dc component (which may also include scattered light) creates a demand for a high dynamic range detector.

Incoherent holography might be called as well Fourier transform imaging, since it is formally similar to Fourier transform spectroscopy,[19] time being here replaced with a 2-D space variable. Theoretical analyses of Fourier transform spectroscopy directly apply to Fourier transform imaging.

II. Signal-to-Noise Ratio in the Reconstructed Image

The SNR for the reconstructed image has been discussed by Lowenthal *et al.*[20] Here we adapt a derivation due to Mertz[1] for the SNR in Fourier transform spectroscopy. The noise n_O in the reconstructed image is a scaled version of the Fourier transform of the noise N_I in the hologram. According to Eq. (2), the Parseval theorem gives

$$\int |N_I(\mathbf{u})|^2 d\mathbf{u} = (\lambda/k)^2 \int |n_O(\mathbf{x})|^2 d\mathbf{x}, \tag{3}$$

which can be written

$$\overline{N_I^2} A = (\lambda/k)^2 \overline{n_O^2} a', \tag{4}$$

where A is the hologram area and a' is the mean area over which noise extends in the plane of the reconstructed image. $\overline{N_I}$ and $\overline{n_O}$ are the average rms noises in the hologram and the reconstructed image, respectively. We assume here that the reconstructed image is obtained from Eq. (2), although taking the real part of it would reduce the noise by a factor of $\sqrt{2}$.

Let a be the area over which the reconstructed image extends. The average signal in the image is

$$\bar{o} = \frac{1}{a}\int o(\mathbf{x})d\mathbf{x} = \frac{O(0)}{a} = \frac{\bar{I}}{a}, \tag{5}$$

where $\bar{I}$ is the average illumination in the hologram [Eq. (1)]. We estimate the SNR for the reconstructed image as

Erez Ribak and J. B. Breckinridge are with California Institute of Technology, Jet Propulsion Laboratory, Pasadena, California 91109; the other authors are with National Optical Astronomy Observatories, ADP Division, P.O. Box 26732, Tucson, Arizona 85726.

Received 4 July 1987.
0003-6935/88/061183-04$02.00/0.

$$\mathrm{SNR}_{\mathrm{rec}} = \frac{\bar{o}}{n_O}. \tag{6}$$

Putting Eqs. (4) and (5) into Eq. (6) yields

$$\mathrm{SNR}_{\mathrm{rec}} = \frac{\sqrt{a'}}{a\sqrt{A}} \frac{\lambda}{k} \frac{\bar{I}}{\bar{N}_I}. \tag{7}$$

Since the smallest resolved area in the image plane is $(\lambda/k)^2 A^{-1}$, one can introduce in Eq. (7) the number $M = (k/\lambda)^2 aA$ of resolved pixels in the image yielding

$$\mathrm{SNR}_{\mathrm{r}} = \frac{\sqrt{a'}}{\sqrt{A}} \frac{1}{\sqrt{M}} \frac{\bar{I}}{\bar{N}_I} = \frac{\sqrt{a'}}{\sqrt{a}} \frac{1}{\sqrt{M}} \mathrm{SNR}_{\mathrm{hol}}, \tag{8}$$

where $\mathrm{SNR}_{\mathrm{hol}}$ is the SNR for the hologram. Equation (8) is formally equivalent to that derived by Lowenthal *et al.*[20] Assuming detector pixels with statistically independent noise, the noise to image area ratio a'/a in the reconstruction is also the ratio of the number P of independent pixels in the detector to the number of independent samples in the hologram. To reduce the noise, we wish the noise area a' to be as large as possible [Eq. (4)] compared with the image area. The factor $\sqrt{a'/a}$ shows that the SNR in the reconstructed image can be improved at will by averaging each sample of the hologram over a larger number of detector pixels. Equation (8) now gives

$$\mathrm{SNR}_{\mathrm{rec}} = \frac{\sqrt{P/M}}{\sqrt{M}} \mathrm{SNR}_{\mathrm{hol}} = \frac{\sqrt{P}}{M} \mathrm{SNR}_{\mathrm{hol}} \tag{9}$$

III. Discussion

Equation (9) holds for any kind of noise (as long as different pixels have statistically independent noise). It shows that the SNR in the reconstructed image decreases when the image complexity increases.[21] For a given detector (given P) and a given object total flux (given $\mathrm{SNR}_{\mathrm{hol}}$), it is proportional to the inverse of the number M of bright pixels resolved in the object, defined as [Eq. (5)]

$$M = aA = \frac{A}{\bar{o}} \int o(\mathbf{x}) d\mathbf{x}. \tag{10}$$

If the object total flux increases as M, keeping constant the object brightness, one can match the detector size to the object size ($P \propto M$), keeping constant $\mathrm{SNR}_{\mathrm{hol}}$. In this case the SNR decreases with image complexity M only as $1/\sqrt{M}$.

When photon noise is the main source of noise, one has

$$\mathrm{SNR}_{\mathrm{hol}} = \sqrt{N/P}, \tag{11}$$

where N is the total number of photons detected. Putting Eq. (11) into Eq. (9) gives

$$\mathrm{SNR}_{\mathrm{rec}} = \frac{\sqrt{N}}{M}, \tag{12}$$

which is independent of the number of pixels in the detector.

In all cases, the maximum achievable SNR in the reconstructed image depends on the number of detector pixels P and the maximum achievable SNR in the detector, which is determined by its saturation level:

$$(\mathrm{SNR}_{\mathrm{rec}})_{\max} = \frac{\sqrt{P}}{M} (\mathrm{SNR}_{\mathrm{hol}})_{\max} \tag{13}$$

Current charge-coupled device (CCD) chips can store up to 160,000 photoelectrons before saturating, which gives $(\mathrm{SNR}_{\mathrm{hol}})_{\max} = 400$. Hence a commercially available 2048- × 2048-pixel CCD can holographically record a 100 × 100-pixel image with a SNR:

$$\mathrm{SNR}_{\mathrm{rec}} = \frac{2048 \times 400}{10{,}000} = 82. \tag{14}$$

IV. Experimental Setup

To verify the dependence of the SNR on image complexity, measured by the parameter M, we employed a phase-compensated rotational-shear interferometer as described by Roddier *et al.*[23] Incoherent holograms were recorded with a CCD camera[24] using a RCA 512- × 320-pixel detector. However, only 250 × 256 pixels were used for the image reconstruction. The holograms were recorded with broadband white light by means of a chromatic corrector as described in Ref. 15.

In our experiment the color correction is achieved by a system of four afocal triplet lenses, combined with a relay lens, all placed after the interferometer. The relay lens reimages the twin images chromatically dispersed, and the beams expand freely to interfere on the detector. The chromatic dispersion is such that the angular distance between the twin images, as viewed from the detector, is proportional to the wavelength. Since fringe spacing is proportional to both the wavelength and the inverse of this angular distance, it becomes wavelength independent. Indeed by putting in Eq. (1) a magnification factor $k = m\lambda$ proportional to the wavelength λ we have a wavelength-independent illumination:

$$I(\mathbf{u}) = O(0) + \mathrm{Re}O(mR\mathbf{u}). \tag{15}$$

After the chromatic corrector every image point is smeared into a spectrum expanding radially from the optical axis. When interfering on the detector the two beams produced by twin points combine to create white-light fringes. We have counted a few hundred such fringes with the CCD detector. A test using system illumination at a series of discrete wavelengths between 500 and 700 nm showed < 4% error for the desired equally spaced fringes.

An important drawback of incoherent holography is the dc bias produced by the term $O(0)$ in Eq. (15). Another bias term composed of light scattered in the system and dark current of the CCD should be added to this term. To remove these bias terms two holograms were taken per image with the fringe phase flipped 180° between them,[21,25–27] thus flipping the sign of the last term in Eq. (15). Taking the difference between the two (digitized) holograms gives

$$D(\mathbf{u}) = \mathrm{Re}O(mR\mathbf{u}), \tag{16}$$

i.e., a hologram with the bias terms removed. Figure 1 shows an example of hologram obtained with this procedure. It has three advantages:

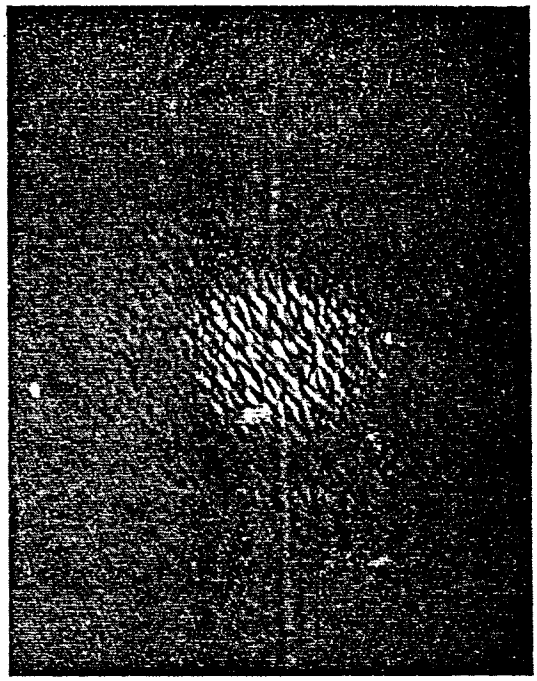

Fig. 1. Incoherent hologram recorded with broadband white light. The dc bias has been removed (background grey level is zero, dark is negative, bright is positive). The object consisted of 40 bright dots.

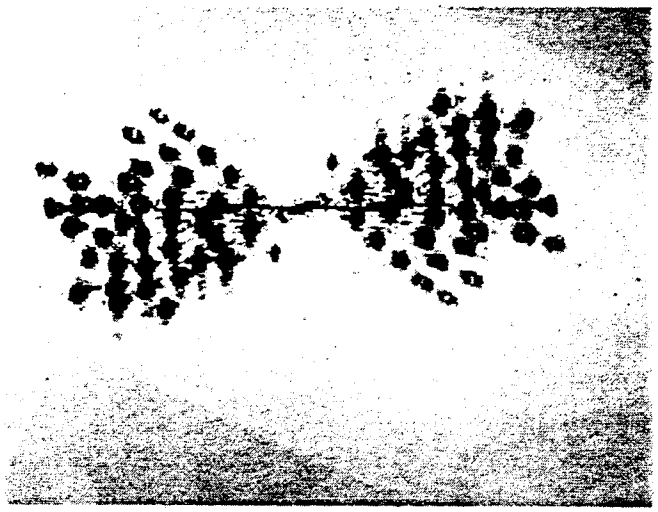

Fig. 2. Reconstructed image obtained by computing the 2-D Fourier transform of the hologram displayed in Fig. 1. The picture is a negative with a reduced dynamic range to better show the noise distribution.

(1) It removes all the bias components including their irrelevant spatial structure.

(2) The noise (contributed mainly by fluctuations in the bias terms) is multiplied by $\sqrt{2}$. But, since the signal is doubled, the SNR increases by a factor of $\sqrt{2}$.

(3) It improves the dynamic range. Although for the CCD readout we still use the same dynamic range, the digital Fourier transform that follows gains from the more limited range of input levels.

We needed an object with a varying and definable degree of complexity. For this purpose, we drilled a large number of round identical holes in a metal plate at random locations. We masked them all with black tape and then unmasked a growing number of holes from the center outward for each hologram. Since the fully exposed mask was very large, the illumination of the holes was slightly different between the center and outer side. The object had, therefore, more than the initially expected two levels of illumination. We estimate the number a'/a of detector pixels per independent area in the hologram to be ~10 for the maximum number of holes (sixty).

V. Experimental Results

The holograms were digitized with a dynamic range of up to 4000 levels. The gain was approximately forty photons per level. The readout noise was low (up to 0.025 of the full range) and, therefore, negligible compared with photon noise. To utilize the full dynamic range, different exposure times were used for different number of holes. The hologram difference shown in Fig. 1 was obtained with forty holes. Hologram differences were Fourier transformed digitally to reconstruct the original object and its twin image. Figure 2 shows the image reconstructed from the hologram of Fig. 1. The noise level in the reconstructed image was measured outside the object extent and found to be uniform all over the reconstruction area as expected.

Since the object had more than two levels of illumination, we defined the object area as the area over which, in each reconstructed point, the signal was above some fraction of its maximum value. The results below were found widely independent of the fraction chosen. This area expressed in number of pixels was taken as our measure of the object complexity M. The SNR in the reconstructed image was obtained by taking the ratio of the signal averaged over the above defined area to the rms noise measured outside the reconstructed object as indicated by Eq. (5).

Assuming pure shot noise, the noise in the hologram was taken as the square root of the average illumination expressed in detected photons per pixels, and the signal was taken as the maximum amplitude of the fringes also expressed in photon units. The SNR in the reconstructed image was then divided by the SNR in the hologram and plotted as a function of M in a log–log scale as shown on Fig. 3. It is clear that for a large object complexity the $1/M$ dependence predicted by Eq. (9) is well observed. However, the factor of proportionality is found to be ~40, well below the factor $\sqrt{P} = 256$ predicted by Eq. (9); i.e., the SNR in the reconstructed image is ~6.4 times lower than the expected value assuming photon noise as the only source of noise in the hologram. The discrepancy is even larger when the image complexity is small.

We believe that these discrepancies can be explained by the imperfections of the optics, such as aberrations, dust, and misalignment of the chromatic corrector. Such errors are highly correlated over different detector pixels and are not included in our modelization. We indeed observed that the point-spread function of the full system is a sharp spike flanked by low-lying

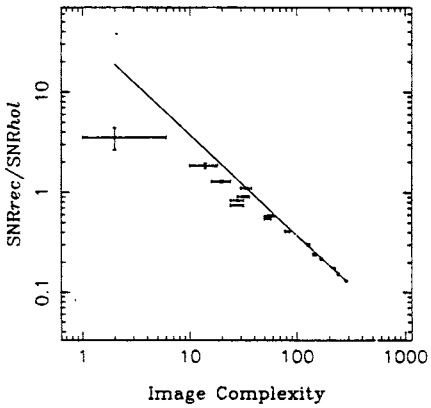

Fig. 3. Ratio of the SNR in the reconstructed image to the SNR in the hologram as a function of the number of bright pixels in the image taken as a measure of its complexity. A minus one slope is shown for comparison with theory.

wide sidelobes. These sidelobes divert power from what we have considered as the reconstructed image (central peaks) and, therefore, produce a lower SNR. When the object consists of closely packed dots the loss of signal power is less severe as observed. The situation is a close analog to that of image reconstruction in radio astronomy where the point spread function is called the dirty beam. Deconvolution techniques such as CLEAN[28] can be used to produce images with an improved SNR.

VI. Summary

We have recorded with a CCD camera holograms obtained with incoherent white-light sources. The SNR in the object reconstruction was compared to theoretical predictions. For complex objects the decrease of the SNR as the inverse of the number of resolved object pixels is well observed. Discrepancies are explained by imperfections in the optics.

References

1. L. Mertz, *Transformations in Optics* (Wiley, New York, 1965).
2. A. Lohmann, "Wavefront Reconstruction for Incoherent Objects," J. Opt. Soc. Am. **55**, 1556 (1965).
3. G. W. Stroke and R. C. Restrick, "Holography with Spatially Incoherent Light," Appl. Phys. Lett. **7**, 229 (1965).
4. G. Cochran, "New Method of Making Fresnel Transforms," J. Opt. Soc. Am. **56**, 1513 (1966).
5. M. V. R. K. Murty and E. C. Hagerott, "Rotational-Shearing Interferometry," Appl. Opt. **5**, 615 (1966).
6. J. B. Breckinridge, "Coherence Interferometer and Astronomical Applications," Appl. Opt. **11**, 2996 (1972).
7. J. B. Breckinridge, "Two-Dimensional White Light Coherence Interferometer," Appl. Opt. **13**, 2760 (1974).
8. J. B. Breckinridge, "A White-Light Amplitude Interferometer with 180-degrees Shear," Opt. Eng. **17**, 156 (1978).
9. F. Roddier and C. Roddier, "Imaging with a Multi-Mirror Telescope," in *Optical Telescopes of the Future, Geneva 1977*, F. Pacini, W. Richter, and R. N. Wilson, Eds. (ESO-CERN, Location, 1978).
10. C. Roddier and F. Roddier, "Imaging with a Coherence Interferometer in Optical Astronomy," in *Formation of Images from Spatial Coherence Functions in Astronomy*, IAU Coll. 49, Van Schooneveld, Ed. (Reidel, Norwell, MA, 1979).
11. F. Roddier, "Rot tion-Shearing Interferometry," in *High Angular Resolution Stellar Interferometry*, IAU Coll. 50, J. Davis and W. J. Tango, Eds. (U. Sydney, 1978).
12. K. Itoh and Y. Ohtsuka, "Interferometric Imaging of a Thermally Luminous Two-Dimensional Object," Opt. Commun. **48**, 75 (1983).
13. N. George and S. Wang, "Cosinusoidal Transforms in White Light," Appl Opt. **23**, 787 (1984).
14. S. Wang and N. George, "Fresnel Zone Transforms in Spatially Incoherent Illumination," Appl. Opt. **24**, 842 (1985).
15. C. Roddier, F. Roddier, F. Martin, A. Baranne, and R. Brun, "Twin-Image Holography with Spectrally Broad Light," J. Opt. **11**, 49 (1980).
16. N. George and S. Wang, "Cosinusoidal Transforms in White Light," Appl. Opt. **23**, 787 (1984).
17. S. Wang and N. George, "Fresnel Zone Transform in Spatially Incoherent White Light," Appl. Opt. **24**, 842 (1985).
18. E. N. Leith and D. K. Angell, "Generalization of Some Incoherent Spatial Filtering Techniques," Appl. Opt. **25**, 499 (1985).
19. P. Connes, "Astronomical Fourier Spectroscopy," Ann. Rev. Astron. Astrophys. **8**, 209 (1970).
20. S. Lowenthal, J. Serres, and H. Arsenault, "Resolution and Film-Grain Noise in Fourier Transform Holograms Recorded with Coherent or Spatially Incoherent Light," Opt. Commun. **1**, 438 (1970).
21. A. Kozma and N. Massey, "Bias Level Reduction of Incoherent Holograms," Appl. Opt. **8**, 393 (1969).
22. A. Papoulis, *Probability, Random Variables and Stochastic Processes* (McGraw-Hill, New York, 1965).
23. F. Roddier, C. Roddier, and J. Demarcq, "A Rotation Shearing Interferometer with Phase-Compensated Roof Prisms," J. Opt. Paris **9**, 145 (1978).
24. Photometrics, Ltd., 2010 N. Forbes Blvd., Suite 103, Tucson, AZ 85745.
25. E. Ribak and E. Leibowitz, "Shearing Stellar Interferometer: 1. Digital Data Analysis Scheme," Appl. Opt. **24**, 3088 (1985).
26. E. Ribak and E. Leibowitz, "Shearing Stellar Interferometer: 2. Optoelectronic Phase Locked System," Appl. Opt. **24**, 3094 (1985).
27. W. T. Rhodes and A. A. Sawchuk, "Incoherent Image Processing," in *Optical Information Processing*, S. H. Lee, Ed. (Springer-Verlag, Berlin, 1981).
28. J. Hogbom, "Aperture Synthesis with a Non-regular Distribution of Interferometer Baselines," Astrophys. J. Suppl. **15**, 417 (1974).

Part of this work was carried out by the Jet Propulsion Laboratory, California Institute of Technology, under contract with the U.S. Army Missile Command at Redstone Arsenal, through the National Aeronautics and Space Administration. Another part was done at NOAO and sponsored by the Strategic Defense Initiative Organization, Office of Innovative Science and Technology, managed by Harry Diamond Laboratories. Erez Ribak is on leave from the Optical Sciences Center, University of Arizona. The National Optical Astronomy Observatories are operated by the Association of Universities for Research in Astronomy, Inc., under contract with the National Science Foundation.

Reprinted from Applied Optics, Vol. 26, Page 1668, May 1, 1987

Interferogram analysis using Fourier transform techniques

Claude Roddier and François Roddier

Fourier transform techniques have been used to map the complex fringe visibility in several types of interferogram. A Gerchberg-type iterative technique is used to eliminate edge effects. Results are presented for two specific cases: seeing measurements and interferometric tests.

I. Introduction

Mapping the amplitude and/or phase of fringes displayed on an interferogram is an important problem in many areas of optics. Figure 1 shows three examples of interferograms we have analyzed. Their use and the way they were obtained are discussed below. Interferogram (c) requires mapping of the fringe phase, interferogram (b) requires mapping of the fringe amplitude, and interferogram (a) requires both.

We have worked mainly on interferograms of type (a) which are clearly the most challenging. The interferogram in Fig. 1(a) was recorded in 1980, in a plane conjugate to the entrance pupil of the 3.6-m CFH telescope in Hawaii, using a rotation-shearing interferometer. The telescope was illuminated with light from the star α Ori (Betelgeuse). The distortion of the fringes due to atmospheric turbulence was frozen in a $\frac{1}{60}$th of a second exposure through a four-stage image intensifier. Photon shot noise is the main source of noise apart from atmospheric perturbations. Mapping the amplitude and the phase of the fringes on the interferogram and averaging the result over many such interferograms, yields an estimate of the complex coherence function of the unperturbed wavefront, the Fourier transform of which gives a reconstructed image of the star.

In 1976, we started using Fourier transform techniques to reduce such interferograms also called incoherent holograms. The 2-D algorithms we used are described in Ref. 1 and the results on the first laboratory tests are presented in Refs. 1–4. Astronomical results are presented in Refs. 5 and 6. In 1982, Takeda *et al.*[7] suggested applying a similar method for the reduction of interferometric tests but using only 1-D Fourier transforms. Macy[8] made tests showing the accuracy of the method. Nugent[9] discussed the effect of sampling and detector nonlinearities. Recently Bone *et al.*[10] developed a 2-D algorithm similar to the one we have used since 1976 and suggested a technique for reducing phase errors produced by the boundaries.

We present here our latest approach to the problem. Our algorithms were developed to estimate both the amplitude and the phase of the fringes (yielding the modulus and the phase of the holographically recorded object Fourier transform). We have recently applied our algorithms to simpler cases, namely, the reduction of interferometric seeing measurements, i.e., the estimation of the fringe amplitude only from interferograms such as that displayed in Fig. 1(b) and the reduction of interferometric tests, i.e., estimation of the fringe phase only from interferograms such as that displayed in Fig. 1(c). We present here results obtained for these last two applications only.

II. Statement of the Problem

The irradiance distribution in a general interferogram can be described as

$$I(\mathbf{r}) = D(\mathbf{r})A(\mathbf{r})\{1 + V(\mathbf{r})\cos[2\pi\mathbf{f}_0 \cdot \mathbf{r} - \phi(\mathbf{r})]\}; \quad (1)$$

$D(\mathbf{r})$ describes the domain D over which the interferogram extends:

$$D(\mathbf{r}) = \begin{cases} 1 & \text{inside the interferogram,} \\ 0 & \text{outside the interferogram.} \end{cases} \quad (2)$$

$A(\mathbf{r})$ will be referred to as the continuum. We assume that it can be determined independently inside domain D. Methods to determine the continuum will be discussed in Sec. II. $\mathbf{f}_0$ is a reference spatial frequency usually taken as the average or undisturbed fringe frequency. $V(\mathbf{r})$ and $\phi(\mathbf{r})$ are to be determined from the interferogram. $V(\mathbf{r})$ is the local fringe visibility and $\phi(\mathbf{r})$ is the local fringe phase with respect to the reference frequency $\mathbf{f}_0$. Equation (1) can be written

The authors are with National Optical Astronomy Observatories, Advanced Development Program, P.O. Box 26732, Tucson, Arizona 85726.

Received 14 October 1986.
0003-6935/87/091668-06$02.00/0.

(a)

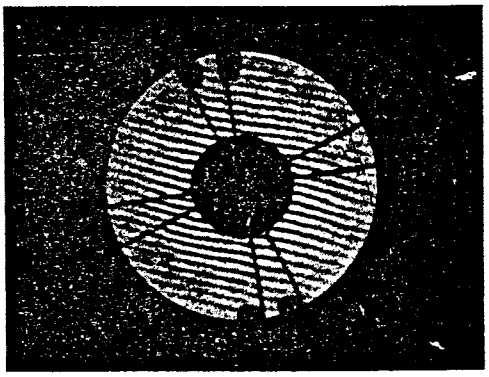

(b)

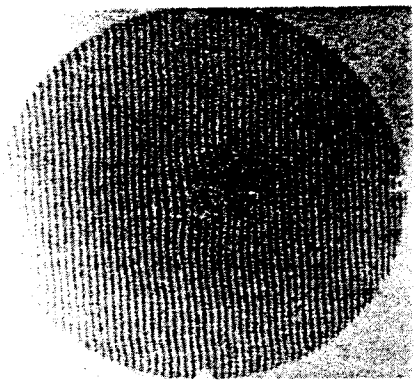

(c)

Fig. 1. Examples of interferograms: (a) stellar interferogram, (b) interferometric seeing measurement, (c) interferometric test.

$$I(\mathbf{r}) = D(\mathbf{r})A(\mathbf{r})[1 + \mathrm{Re}C(\mathbf{r}) \exp(2i\pi\mathbf{f}_0 \cdot \mathbf{r})]$$
$$= D(\mathbf{r})A(\mathbf{r})[1 + \tfrac{1}{2}C(\mathbf{r}) \exp(2i\pi\mathbf{f}_0 \cdot \mathbf{r}) + \tfrac{1}{2}C(\mathbf{r}) \exp(-2i\pi\mathbf{f}_0 \cdot \mathbf{r})], \quad (3)$$

where $C(\mathbf{r})$, often called the complex fringe visibility, is defined as

$$C(\mathbf{r}) = V(\mathbf{r}) \exp[-i\phi(\mathbf{r})]. \quad (4)$$

The problem is to determine $C(\mathbf{r})$ from $I(\mathbf{r})$. The Fourier transform of $I(\mathbf{r})$ is

$$\hat{I}(\mathbf{f}) = \hat{D}(\mathbf{f}) * \hat{A}(\mathbf{f}) * [\delta(\mathbf{f}) + \tfrac{1}{2}\hat{C}(\mathbf{f} - \mathbf{f}_0) + \tfrac{1}{2}\hat{C}^*(-\mathbf{f} - \mathbf{f}_0)], \quad (5)$$

where the asterisk ($*$) denotes a convolution product, the asterisk superscript (*) denotes a complex conjugate, and $\delta(\mathbf{f})$ represents a Dirac impulse distribution.

Let us consider first the ideal case of an infinite interferogram with a uniform continuum [$A(\mathbf{r}) = D(\mathbf{r}) = 1$ for all $\mathbf{r}$]. In this case the Fourier transform of the interferogram reduces to the last convolution factor in Eq. (5), i.e., to the three following terms: a Dirac impulse $\delta(\mathbf{f})$ at the origin and two terms shifted from the origin and centered at frequency $+\mathbf{f}_0$ and $-\mathbf{f}_0$, the Fourier transform of the complex fringe visibility and its transposed complex conjugate. This clearly shows that the complex fringe visibility can be unambiguously determined only as long as $C(\mathbf{r})$ is a bandlimited function, with a frequency cutoff f_c, and $|\mathbf{f}_0|$ is taken larger than f_c. This condition holds whatever the method used to determine the fringe amplitude and/or phase. Here we assume that it is satisfied in all that follows.

The complex fringe visibility can be obtained by setting to zero all the points in the closed half-part of the frequency plane opposite $\mathbf{f}_0$, shifting the result by an amount $-\mathbf{f}_0$ back to the origin, and taking an inverse Fourier transform. This is nothing more than a generalization in two dimensions of a standard technique in wave processing. The interferogram can be considered as an amplitude and/or phase modulated 2-D sinusoid. The process of recovering the fringe amplitude and/or phase is a demodulation process. Setting to zero half of the frequency plane yields the Fourier transform of the associated analytic signal and shifting the result by an amount $-\mathbf{f}_0$ eliminates the carrier frequency.

Difficulties arise from the fact that any interferogram has a finite extent and, generally, the continuum is not uniform. Since $D(\mathbf{r})$ has a bounded support, its Fourier transform $\hat{D}(\mathbf{f})$ is analytic and therefore extends to infinity. After convolution with $\hat{D}(\mathbf{f})$ and $\hat{A}(\mathbf{f})$ in Eq. (5), the three terms described above now overlap producing errors in the determination of the complex fringe visibility. The extended wings may also produce significant aliasing errors associated with the use of discrete Fourier transforms. In Sec. III we discuss how to correct for continuum nonuniformities, and in Sec. IV we propose new ways to deal with the finite extent of the interferogram.

III. Estimation of the Continuum

We found that fluctuations of the continuum $A(\mathbf{r})$ due to imperfections in the optics often seriously affect the data. An independent measure of the continuum is therefore necessary if one seeks an accurate estimate of the fringe visibility. Some interferometric systems provide two outputs with fringes in opposite phase, in which case the continuum is easily obtained by simple addition of the two output frames. Dividing $I(\mathbf{r})$ by $A(\mathbf{r})$ eliminates the effect of the continuum nonuniformities and considerably improves the final result. Unfortunately in all the cases we have studied, only one output was available. We have devised and implemented three different techniques to estimate the continuum.

A. Use of a Frame Without Fringes

For our seeing measurements, fringes were obtained with broadband light. In this case, it is easy to introduce an optical path difference in the two arms of the interferometer to make fringes disappear. The resulting illumination may slightly differ from that of the continuum in the interferogram. We found that the best results were obtained by taking the Fourier transform of the interferogram, removing from it two spectral windows centered at frequencies $+\mathbf{f}_0$ and $-\mathbf{f}_0$ where most of the fringe signal is located, and replacing them with the corresponding values obtained from the Fourier transform of the frame without fringes (appropriately weighted). Our estimate of the continuum is obtained by taking the inverse Fourier transform of the result. Figure 2 shows an example of such a correction. Figure 2(a) shows a scan across one line of the raw data (interferogram). Figure 2(b) shows the fluctuations of the continuum estimated as described above. Figure 2(c) shows the result of the division $I(\mathbf{r})/A(\mathbf{r})$. The improvement is clearly apparent.

B. Use of a Frame with Different Fringe Orientation

With narrowband laser light, the above procedure is not applicable. However, another frame can be taken with fringes oriented at 90° from the previous one. In this case, we take the Fourier transform of the first interferogram, remove as above two windows centered at frequencies $+\mathbf{f}_0$ and $-\mathbf{f}_0$, and replace them with the corresponding values obtained from the Fourier transform of the second interferogram which are essentially free from fringe signal. Figure 1(c) shows an interferogram of a 1.8-m telescope mirror under test at NOAO. The interferogram was taken with a scatter plate interferometer[11,12] The fringe amplitude is clearly nonuniform. A second interferogram (not shown) was taken with fringes oriented at 90°. The continuum was estimated as described above. Figure 3(a) shows the result of the division $I(\mathbf{r})/A(\mathbf{r})$.

C. Use of Symmetries

When no other frame is available, one can still make use of the symmetry properties of the interferogram. If the shape of the interferogram is invariant under a 90° rotation, one can still remove, as described above, two spectral windows where the fringe signal is concentrated, and replace them by the corresponding values taken on the same Fourier transform after a 90° rotation. We applied this technique in some cases to incoherent holograms.

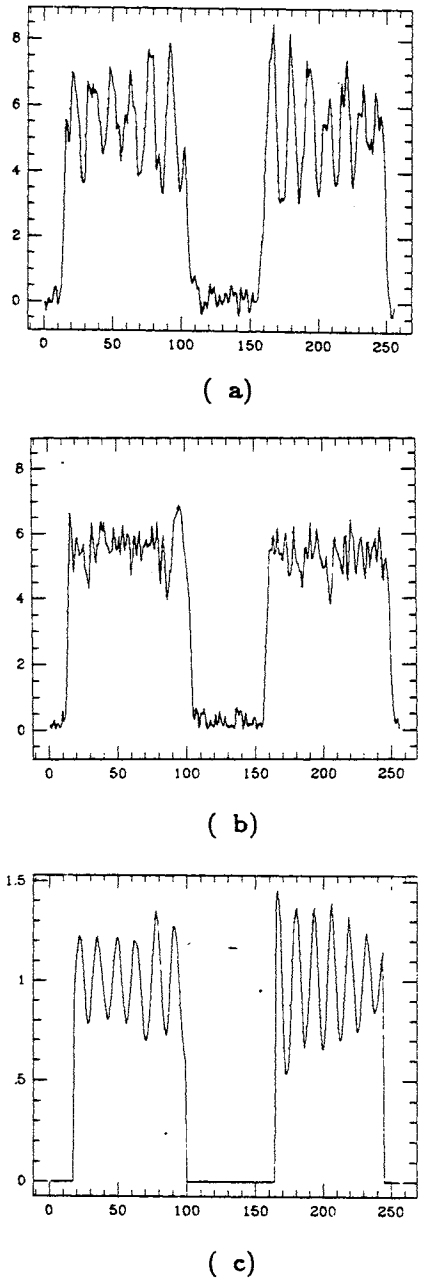

Fig. 2. Seeing measurements; correction for the fluctuations of the continuum: (a) raw data, (b) estimated continuum, (c) corrected data.

IV. Boundary Problem

As sown in Sec. 1, the boundaries of the interferogram are an important source of error if they are not properly taken into account; this was also noted by Bone *et al.*[10] The discontinuities of $D(\mathbf{r})$ at the edge of the interferogram produce large ripples in $\hat{D}(\mathbf{f})$ which dominate the Fourier transform of the interferogram. A way to deal with this problem is to extrapolate the interferogram beyond its limits. Indeed, if the Fourier transform $\hat{C}(\mathbf{f})$ of the complex fringe visibility $C(\mathbf{r})$ has a bounded support as assumed in Sec. I, $C(\mathbf{r})$ is analytic and can therefore be uniquely extrapolated beyond the interferogram limits by analytic continuation. In 1974, Gerchberg[13] proposed a simple iterative algorithm for analytic continuation. We have used Gerchberg's method to extrapolate the interferograms.

The algorithm works as schematically described in Fig. 4. After division by the continuum, we first subtract unity inside the interferogram. According to Eq. (1), we get

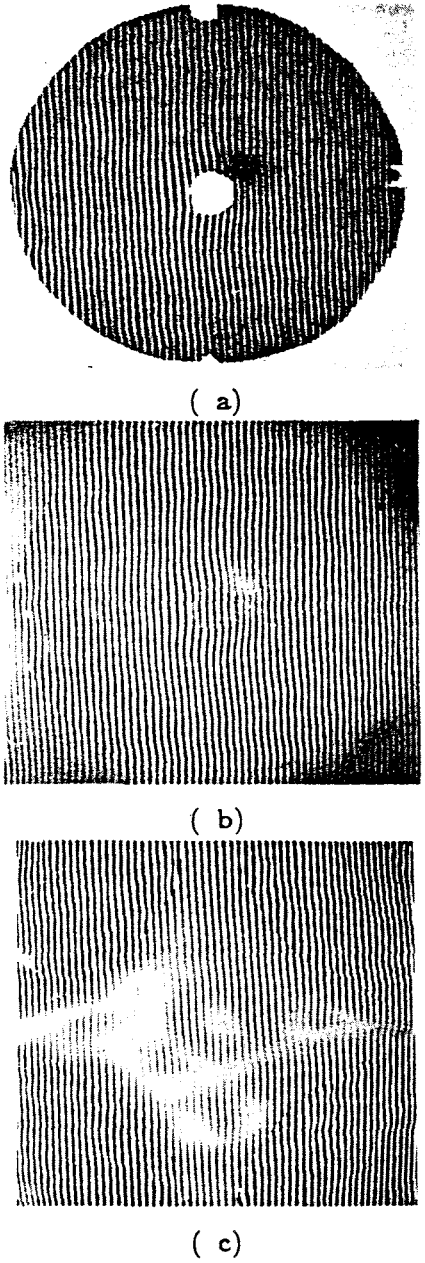

Fig. 3. Processing of the interferometric test: (a) after sampling and correction for the continuum, (b) after extrapolation of the fringes, (c) same as (b) but shifted by half a period.

$$J(\mathbf{r}) = \frac{I(\mathbf{r})}{A(\mathbf{r})} - D(\mathbf{r})$$

$$= D(\mathbf{r})V(\mathbf{r})\cos[2\pi\mathbf{f}_0\cdot\mathbf{r} - \phi(\mathbf{r})], \quad (6)$$

the Fourier transform of which is

$$\mathcal{J}(\mathbf{f}) = \hat{D}(\mathbf{f}) * [\tfrac{1}{2}\hat{C}(\mathbf{f}-\mathbf{f}_0) + \tfrac{1}{2}\hat{C}^*(-\mathbf{f}-\mathbf{f}_0)]. \quad (7)$$

If the interferogram was infinite, $\mathcal{J}(\mathbf{f})$ would be entirely concentrated inside two circles at $+\mathbf{f}_0$ and $-\mathbf{f}_0$ and with radius f_c [the frequency cutoff of $\hat{C}(\mathbf{f})$]. The algorithm consists of setting to zero all the values outside these two circles. The inverse Fourier transform of the result produces an interferogram with extrapolated fringes. The values inside the interferogram are replaced by the original values. The extrapolated values are kept as they are. The new interferogram is Fourier transformed and the procedures is repeated until most of the energy becomes concentrated inside the two circles. This usually takes only a few iterations. The fringe pattern inside the interferogram remains unchanged. It is only extrapolated outside the interferogram limits. This prevents the two terms in the Fourier transform from overlapping. Figure 3(b) shows an extrapolation of the fringes displayed in Fig. 3(a). The two fringe patterns are identical inside the interferogram boundaries.

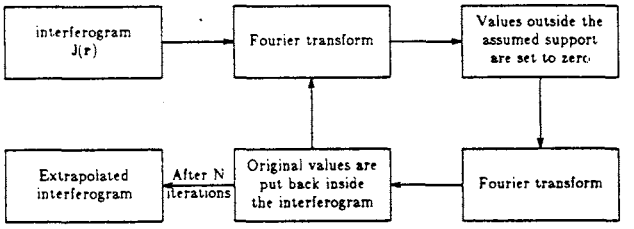

Fig. 4. Gerchberg's extrapolation algorithm.

A discrete Fourier transform must be thought of as the Fourier transform of a periodic function, i.e., in two dimensions, of a plane tiled with interferograms all adjacent and identical. The algorithm described above not only extrapolates the fringes but also nicely interpolates them from one period to another thus avoiding any discontinuity in the periodic tiling. Figure 3(c) is identical to Fig. 3(b) but for a shift of one-half period in both directions; it clearly demonstrates the continuity of the interpolation. Methods previously proposed to extrapolate the fringes do not have this property.[10] Because the periodic tiling is continuous, the energy is highly localized in the Fourier transform plane and aliasing errors due to finite sampling are avoided.

V. Phase Unwrapping

The phase of the complex fringe visibility, also called the wrapped phase, is defined on a circle, modulo 2π. For some uses, such as image reconstruction through turbulence[1–4,14–19] or wavefront reconstruction,[7,8,20–22] it is necessary to compute an unwraped phase, defined on the real axis. Mathematically, the unwrapped phase is defined as the integral of the derivative of the wrapped phase. In practice, due to finite sampling, an unwrapped phase is obtained by summing the phase differences. As discussed by Itoh,[15] in one dimension this is possible only if the true phase jumps are smaller than π, i.e., if the true phase differences range between $-\pi$ and $+\pi$.

Takeda *et al.*[7] and Macy[8] compute phase differences from the phase of the complex fringe visibility. It is equivalent but more elegant to compute the sine and the cosine of the phase differences from the real and imaginary parts of the complex visibility yielding automatically phase differences ranging between $-\pi$ and $+\pi$, which can be directly summed without bothering about phase jumps. As shown by Itoh and Ohtsuka,[16]

turbulence effects are best removed by averaging sine and cosine of the phase differences computed as above.

Unfortunately, when the fringe contrast is low or the interferogram is noisy, as in the example of Fig. 1(a), phase jumps larger than π often occur and none of the methods described above works. Tribolet[23] proposed to unwrap the phase with an adaptive sampling interval. In two dimensions one may use many different integration paths and use the constraint that each path should yield the same result. Least-squares algorithms have been proposed to integrate 2-D wavefront slopes.[20–22] Unfortunately they do not take properly into account the statistics of the errors on phase differences, namely, the fact that a small error on the complex fringe visibility may produce nearly a 2π error on the phase difference producing dislocations in the reconstructed wavefront surface. We have written a 2-D phase unwrapping algorithm that seeks to find and correct these dislocations.[1] Recently Ghiglia *et al.*[24] proposed a 2-D phase unwrapping algorithm based on cellular automata that may also isolate dislocations.

VI. Results on Seeing Measurements

Figure 1(b) shows an example of seeing measurements made with a rotational-shear interferometer. The interferometer and this use are described in Refs. 25 and 26. Fringes are photographically recorded in a plane conjugate to the entrance pupil of a 50-cm astronomical telescope illuminated with a bright star. The film is photometrically calibrated. The interferometer produces two images of the telescope pupil rotationally sheared about their center. Clearly, the fringe visibility decreases as the base line for interference increases from the center to the edge, showing the loss of coherence produced by atmospheric turbulence on exposures of the order of a few tens of seconds. The shear angle can be adjusted to match the coherence length with the interferogram size. The optical bandwidth was limited by an interference filter to ~100 Å.

The algorithms described above were used to map the fringe visibility on such interferograms. Theory predicts that the fringe visibility should decrease with the base line r as[27]

$$V(r) = \exp[-3.44(r/r_0)^{5/3}], \tag{8}$$

where r_0 is a parameter called Fried's parameter which is a measure of the seeing quality of the atmosphere. Figure 5 is a plot of the observed log of the log visibility as a function of the log base line together with a 5/3 slope best fit showing how well the 5/3 law in Eq. 8 is verified. We estimate that the method yields a determination of r_0 with a few percent accuracy.

VI. Results of Interferometer Tests

The same methods were applied to scatter plate interferograms used to control the figuring of large mirrors under test at NOAO. Fig. 1(c) shows such an interferogram obtained on a 1.8-m mirror with a honeycomb structure. The reference wave was highly tilted to enable us to recover small details on the wavefront surface. Figures 3(a)–(c) show intermediate steps of the process as described above. Because fringes have a large amplitude at the edge of the interferogram, the use of Gerchberg's extrapolation was found to be especially important.

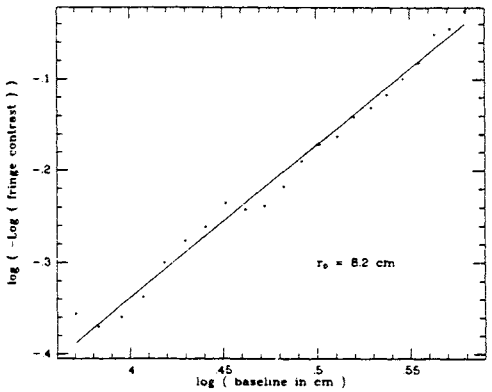

Fig. 5. Seeing measurements: plot of the log–log visibility vs log base line (dots) and 5/3 slope best fit (full line).

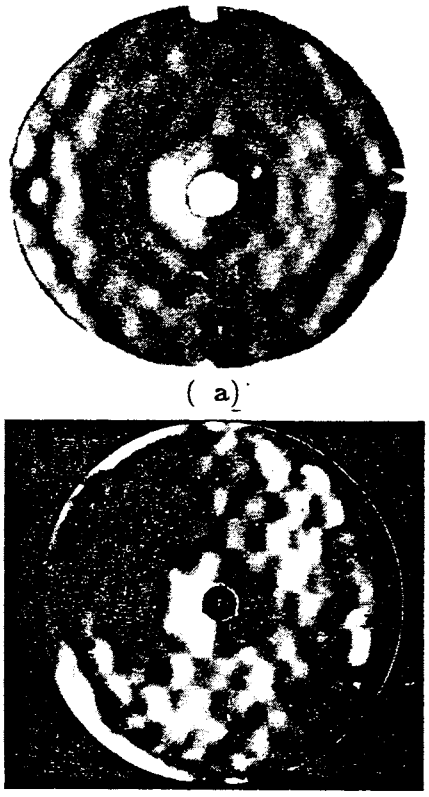

Fig. 6. (a) Wavefront slopes derived from the interferogram of Fig. 1(c) and (b) knife-edge test on the same mirror.

Figure 6(a) shows a map of the wavefront slope along the horizontal direction reconstructed from the interferogram in Fig. 1(c). Such a display simulates the result of a knife-edge test. For comparison, Fig. 6(b) shows the result of a real knife-edge test made on the same mirror a few months before. Clearly the two results are in excellent agreement. Small differences can be attributed to the effect of atmospheric turbu-

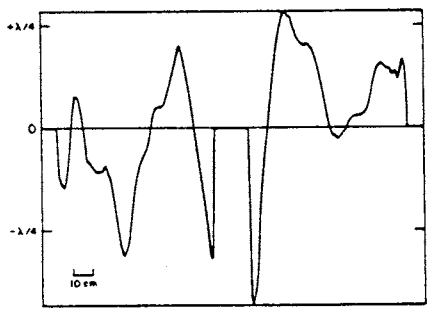

Fig. 7. Profile of the reconstructed wavefront displayed in Fig. 6(a). Horizontal cut near the center.

lence in the laboratory, which does not average out in a single short-exposure interferogram. These effects can be removed by averaging the results of several interferograms.

Figure 7 shows a plot of one line of the reconstructed wavefront taken near the center of the 256 computed lines. The phase was unwrapped without difficulty using the simple 1-D algorithm described in Sec. IV. Because of the high amplitude of the fringes and the high signal-to-noise ratio of the data, it was not necessary to use more robust 2-D algorithms. However, it is worth mentioning that, when the same data were processed without Gerchberg's extrapolation, the simple 1-D algorithm did not work, showing evidence for phase errors. The peak-to-valley amplitude displayed in Fig. 7 is of the order of half a wave. The small ripples related to the honeycomb structure have an amplitude of typically one-tenth of a wave, corresponding to 0.03-μm bumps on the mirror surface. The horizontal resolution on the mirror is 3 cm. We have therefore been able to reconstruct the wavefront with interferometric accuracy while achieving a spatial resolution comparable to that of a knife-edge test.

The interferogram displayed in Fig. 1(c) and the knife-edge test presented in Fig. 6(b) were provided by J. Richardson at NOAO. The authors also wish to thank Janine Connes (CNRS, France) for stimulating discussions. This work was supported partly under contract from the Jet Propulsion Laboratory of the California Institute of Technology to the Optical Sciences Center, University of Arizona, and partly under contract from the Rome Air Development Center.

The National Optical Astronomy Observatories are operated by the Association of Universities for Research in Astronomy, Inc., under contract with the National Science Foundation.

References

1. C. Roddier, "Enregistrement holographique d'images astronomiques degradées par la turbulence atmosphérique," ATP traitement des images du CNRS, contract 3109, final report (1979).
2. F. Roddier and C. Roddier, "Imaging with a Multi-Mirror Telescope," in *Proceedings, ESO Conference on Optical Telescopes of the Future*, Geneva (1977), F. Pacini, W. Richter, and R. N. Wilson, Eds., Geneva 23: ESO c/o CERN (1978).
3. C. Roddier and F. Roddier, "Imaging with a Coherence Interferometer in Optical Astronomy" in *Proceedings, IAU Colloquium 49 on Formation of images from spatial coherence functions in astronomy*, Groningen, 1978, C. van Schooneveld, Ed. (Reidel, Norwell, MA, 1979).
4. F. Roddier, "Rotation Shearing Interferometry," in *Proceedings, IAU Colloquium 50 on High Angular Resolution Stellar Interferometry*, U. Maryland, 1978, J. Davis and W. J. Tango, Ed. (Chatterton Astronomy Dept., U. Sydney, 1979).
5. C. Roddier and F. Roddier, "High Angular Resolution Observations of Alpha Orionis with a Rotation Shearing Interferometer," Astrophys. J. **270**, L23 (1983).
6. F. Roddier and C. Roddier, "An Image Reconstruction of Alpha Orionis," Astrophys. J. **295**, L21 (1985).
7. M. Takeda, I. Hideki, and S. Kobayashi. "Fourier-Transform Method of Fringe-Pattern Analysis for Computer-Based Topography and Interferometry," J. Opt. Soc. Am. **72**, 156 (1982).
8. W. W. Macy, "Two-Dimensional Fringe-Pattern Analysis," Appl. Opt. **22**, 3898 (1983).
9. K. A. Nugent, "Interferogram Analysis Using an Accurate Fully Automatic Algorithm," Appl. Opt. **24**, 3103 (1985).
10. D. J. Bone, H.-A. Bachor, and R. J. Sandeman, "Fringe-Pattern Analysis Using a 2-D Fourier Transform," Appl. Opt. **25**, 1653 (1986).
11. J. M. Burch, "Scatter Fringes of Equal Thickness," Nature London **171**, 889 (1953).
12. R. M. Scott, "Scatter Plate Interferometry," Appl. Opt. **8**, 531 (1969).
13. R. W. Gerchberg, "Super-Resolution Through Error Energy Reduction," Opt. Acta **21**, 709 (1974).
14. B. L. McGlamery, "Image Restoration Techniques Applied to Astronomical Photography," NASA Tech. Rep. SP-256 (1971).
15. K. Itoh, "Analysis of the Phase Unwrapping Algorithm," Appl. Opt. **21**, 2470 (1982).
16. K. Itoh and Y. Ohtsuka, "Phase Estimation Based on the Maximum Likelihood Criterion," Appl. Opt. **22**, 3054 (1983).
17. K. Itoh and Y. Ohtsuka, "Interferometric Imaging of a Thermally Luminous Two-Dimensional Object," Opt. Commun. **48**, 75 (1983).
18. L. N. Mertz, "Phase Estimation with Few Photons," Appl. Opt. 23, 1638 (1984).
19. L. N. Mertz, "Multichannel Seeing Compensation via Software," Appl. Opt. **24**, 2898 (1985).
20. D. L. Fried, "Least-Squares Fitting a Wave-Front Distortion Estimate to an Array of Phase-Difference Measurements," J. Opt. Soc. Am. **67**, 370 (1977).
21. R. H. Hudgin, "Wave-Front Reconstruction for Compensated Imaging," J. Opt. Soc. Am. **67**, 375 (1977).
22. B. R. Hunt, "Matrix Formulation of the Reconstruction of Phase Values from Phase differences," J. Opt. Soc. Am. **69**, 393 (1979).
23. J. M. Tribolet, "A New Phase Unwrapping Algorithm," IEEE Trans. Acoust. Speech Signal Process. **ASSP-25**, 170 (1977).
24. D. C. Ghiglia, G. A. Mastin, and L. A. Romero, "Cellular Automata Method for Phase Unwrapping," J. Opt. Soc. Am. A **4**, 267 (1987).
25. C. Roddier, "Measurements of the Atmospheric Attenuation of the Spectral Components of Astronomical Images," J. Opt. Soc. Am. **66**, 478 (1976).
26. C. Roddier and J. Vernin, "Relative contribution of upper and lower atmosphere to integrated refractive-index profiles," Appl. Opt. **16**, 2252 (1977).
27. F. Roddier, "The Effects of Atmospheric Turbulence in Optical Astronomy," Prog. Opt. **19**, 281 (1981).

Reprinted from Applied Optics, Vol. 26, Page 197, January 15, 1987

Phase closure with a rotational shear interferometer

Erez Ribak

Jet Propulsion Laboratory, 4800 Oak Grove Drive, Pasadena, California 91109.
Received 13 September 1986.
0003-6935/87/020197-03$02.00/0.

Phase closure is a radio astronomical technique that enables recovering Fourier transform phases that would otherwise be corrupted by atmospheric and instrumental errors.[1] It has been suggested in the past that radio methods, such as aperture synthesis and phase closure, are applicable to the visible region too.[2,3] Recently direct phase closure was demonstrated on an optical telescope,[4] and it was shown[5] that the method of triple correlation[6] is a generalization of phase closure. Proposed here is a simple and efficient way of achieving phase closure by means of rotational shear interferometery.

In a rotational shear interferometer one images the telescope aperture onto the interferometer, then interferes the aperture with itself in a rotated orientation. If we observe an object $o(\mathbf{x})$ whose Fourier transform is $O(\mathbf{u})$, it can be shown[7] that the intensity of the interference pattern behaves like

$$I(\mathbf{u}) = O(0) + \mathrm{Re}[O(2\mathbf{u}|\sin\theta/2|/\lambda)]\,, \qquad (1)$$

where θ is the rotation angle and λ is the wavelength. It is obvious that to achieve the maximum frequency content permitted by the telescope the shear has to be 180°, but better dynamic range and SNR are possible for lower frequencies. This zoom effect is achieved by turning to smaller rotation angles. The second term on the right can also be written as

$$\mathrm{Re}[O(2\mathbf{u}|\sin\theta/2|/\lambda)] = |\tilde{G}(\mathbf{r})|\cos[\psi(\mathbf{r}) + \phi(\mathbf{r})]\,, \qquad (2)$$

where $\mathbf{r} = 2\mathbf{u}|\sin\theta/2|/\lambda$, $G(\mathbf{r})$ is the mutual coherence function, and $\psi(\mathbf{r}) = \arg[G(\mathbf{r})]$. $\phi(\mathbf{r})$ is the combination of all other phase fluctuations not associated with the mutual coherence function, mainly atmospheric but also those due to telescope imperfections etc. (No absorption in the atmosphere is assumed.) In phase closure one chooses three vectors $\mathbf{r}_1,\mathbf{r}_2,\mathbf{r}_3$ so that $\mathbf{r}_1 + \mathbf{r}_2 + \mathbf{r}_3 = 0$. In this case the atmospheric and instrumental phases must obey $\phi(\mathbf{r}_1) + \phi(\mathbf{r}_2) + \phi(\mathbf{r}_3) = 0$. When adding the total phases for the three vectors, the atmospheric and telescope-induced phases cancel out, and we remain with the sum of the phases of the coherence function $\psi(\mathbf{r}_1) + \psi(\mathbf{r}_2) + \psi(\mathbf{r}_3)$. The same theory applies also to any closed loop of vectors, not just three.

If we choose a rotation angle $\theta = 120°$, we automatically create an infinite number of closure loops. Every equilateral triangle whose center coincides with the center of rotation will constitute such a set of vectors. At each vertex of such a triangle, we have an interference of two out of three possible points 120° apart on the telescope aperture [Fig. 1(a)]. The same applies for a rotation angle of 72° where we now have phase closure in all possible centered pentagons [Fig. 1(b)] etc. As remarked above, we do lose in terms of spatial frequency as we rotate at smaller angles. On the other hand, we could rotate by 144° and measure along the five-pointed star that is created as we connect all vectors 144° apart [Fig. 1(c)]. In general, for n vertices (or apertures, as referred to in radio astronomy) we have

$$n\theta = 2\pi m, \qquad m = 1,2,3,\ldots. \qquad (3)$$

Since the rotation angle θ is always less than π, we get $n > 2$ m

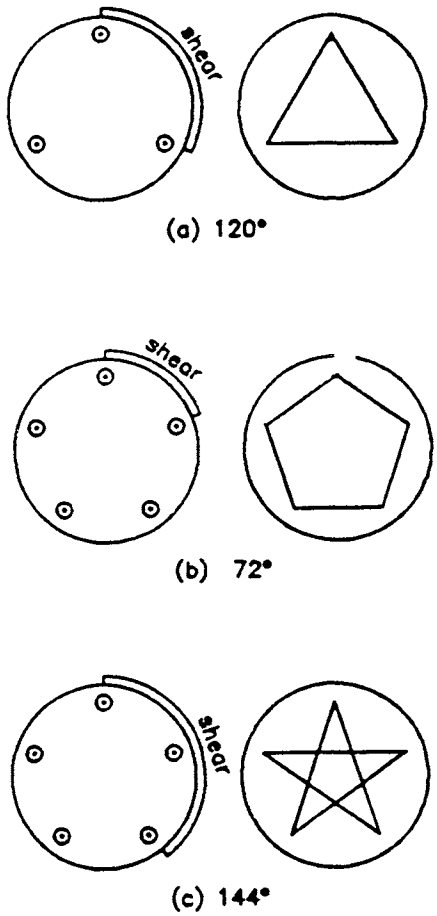

Fig. 1. (a) Two interfering apertures at 120° shear and one set of base lines in the telescope aperture that constitutes a closure loop. (All centered equilateral triangles are such loops.) (b) As in (a) with 72° rotation and pentagon. (c) As in (a) with 144° rotation and five-pointed star.

Table I. Possible Shear Angles and Associated Maximum Frequency (in Terms of the Telescope Cutoff Frequency f_c)

n (vertices)		3	4	5	6	7
m 1	θ	120°	90°	72°	60°	52°
	f_{max}/f_c	0.87	0.77	0.58	0.50	0.44
$m = 2$	θ			144°	120°	103°
	f_{max}/f_c			0.95	0.87	0.78
$m = 3$	θ					154°
	f_{max}/f_c					0.97

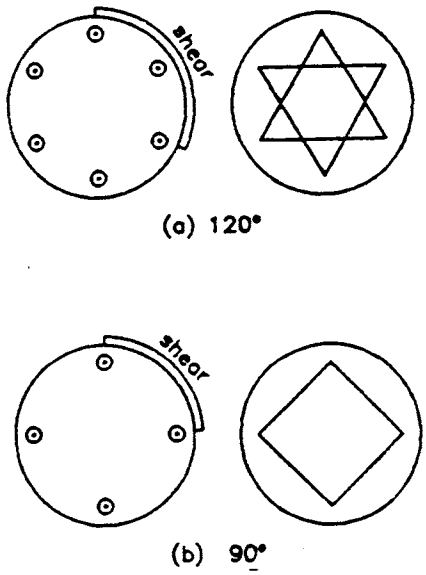

Fig. 2. As in Fig. 1(a) showing two redundant triangles with the same phase closure value. (b) As in Fig. 1(a) with 90° rotation. The sum of phases around the square (or any even-sided regular polygon) should always be zero.

(Table I). The loss of phase information at high frequencies, as inferred from this table, is not so severe. (Amplitudes can still be measured at 180° or up to the highest frequency.) This is because many methods have been developed to estimate the missing phases even from data that hold no phase information at all (Fienup, Knox-Thompson, speckle imaging, self-calibration, and many others[1,8–12]). These methods have shown their ability both in the visible and radio regimes.

A shortcoming of the proposed method is that for filled apertures, such as used in astronomy in the optical region, the number of closure loops is not sufficient to determine uniquely all the Fourier plane phases. In radio astronomy, where the apertures are few and (sometimes) far apart, the number of relations (aperture pairs) outnumbers the number of variables (coherence phases and amplitudes). Since the problem is overdetermined, methods like self-calibration, also known as hybrid mapping, are being used. In the interferogram of the two mutually rotated apertures, every base line (and thus every closure loop) exists twice [Fig. 2(a)]. This is due to the fact that the object $o(\mathbf{x})$ is real, and its Fourier transform $O(\mathbf{u})$ must be Hermitian. If the interferogram emcompasses N pixels on the (2-D) detector, we will have N/n phase closure relations, out of which one-half is equal (up to the noise) and opposite in sign to the other half. Thus there is not enough redundancy to solve for all the needed phase relations. This is the case for odd values of n, whereas for even values of n each closed loop has equal and opposite sides, and the coherence function phases are equal and opposite in sign [Fig. 2(b)]. Included in this category is the $n = 2$ case (180° rotation) not mentioned in the table. Since the closure phase is trivially zero in even regular polygons, they can only be used to enhance the signal-to-noise of the amplitude measurements.

A drawback of the scheme compared to radio astronomy is that all the base lines have to be of the same length, as set by the shear vector $\mathbf{r}$. Every point in the interferogram is involved in only one phase closure loop. This base line limitation also rules out amplitude closure, which is another tool in radio astronomical interferometry.[1] Amplitude closure cannot be applied directly, since it demands that measurements be taken simultaneously over base lines of different lengths. One should also keep in mind that the quantity measured is the local intensity, and the phase value related to this intensity has still to be extricated.[3] This is especially difficult under low light level conditions or near zeroes of the mutual coherence function. On the other hand, once we have phase closure values for one interferogram, we can average over many interferograms to improve the SNR.

There are different approaches as to how to collect and use the phase closure data. One way is to take measurements at

lower shear angles and try to build a partial phase and amplitude map consistent with these data and other physical demands, such as source positivity and limited size. The shear value is raised, as is the frequency content of the data, and a map utilizing the former map and the new data is constructed. The process is repeated until the highest frequency possible is attained. The other way round is also possible: start at a high frequency, high rotation angle, then interpolate between points by going to a simple fraction of the first angle, etc. Again, we demand that in every step we have consistency with object positivity and limited support. A third way is to build the phase map from one shear value by demanding that the phases are continuous as one proceeds from one polygon to the adjacent one (both in the radial and tangential directions). This approach is equivalent to the maximum-entropy demand of smoothness, this time in Fourier space. Notice also that if one employs maximum entropy methods, phase closure values from interferograms of different shear can be combined as constraints. The increase in number of phase relations improves the quality of the solution. Of course, there is always the approach of radio astronomy, where a model is iteratively improved on under the closure constraints.[1] A combination of different methods is also possible.

To summarize: phase closure can be realized on existing telescopes and existing interferometers without special modifications. Although not all base lines are possible, the extra constraints provided by the closure phases reduce very much the ambiguity now existing in phaseless image reconstruction.

The work described in this paper was carried out by the Jet Propulsion Laboratory, California Institute of Technology, under contract with the National Aeronautics and Space Administration. The author is on leave from the Optical Sciences Center of the University of Arizona.

References

1. T. J. Pearson and A. C. S. Readhead, "Image Formation by Self-calibration in Radio Astronomy," Ann. Rev. Astron. Astrophys. **22,** 97 (1984).
2. W. T. Rhodes and J. W. Goodman, "Interferometric Technique for Recording and Restoring Images Degraded by Unknown Aberrations," J. Opt. Soc. Am **63,** 647 (1973).
3. D. H. Rogstad, "A Technique for Measuring Visibility Phase with an Optical Interferometer in the Presence of Atmospheric Seeing," Appl. Opt. **7,** 585 (1968).
4. J. E. Baldwin, C. A. Haniff, C. D. Mackay, and P. J. Warner, "Closure Phase in High-Resolution Optical Imaging," Nature London **320,** 595 (1985).
5. F. Roddier, "Triple Correlation as a Phase Closure Technique," Opt. Commun. **60,** 145 (1986).
6. A. W. Lohmann, G. P. Weigelt, and B. Wirnitzer, "Speckle Masking in Astronomy: Triple Correlation Theory and Applications," Appl. Opt. **22,** 4028 (1983).
7. F. Roddier, "Rotation Shearing Interferometry," in *High Angular Resolution Stellar Interferometry* (IAU Colloquium 50) J. Davis and W. J. Tango, Eds. (Astronomy Department, School of Physics, U. Sydney, 1979).
8. R. H. T. Bates, "Astronomical Speckle Imaging," Phys. Rep. **90,** 203 (1982).
9. F. R. Fienup, "Reconstruction of an Object from the Modulus of its Fourier Transform," Opt. Lett. **3,** 27 (1978).
10. K. T. Knox and B. J. Thompson, "Recovery of Images from Atmospherically Degraded Short Exposure Photographs," Astrophys. J. Lett. **193,** L45 (1974).
11. A. Chelli and J. M. Mariotti, "Visibility and Phase Analysis for Image and Pupil Plane Interferometry at Optical Wavelengths," Aston. Astrophys. **157,** 372 (1986).
12. E. Ribak "Astronomical Imaging by Filtered, Weighted Shift-and-Add," J. Opt. Soc. Am. A **3,** 2069 (1986).